

Silica Microspheres Functionalized with Self-assembled Nanomaterials

Ishac Lamei Nagiub Kandas

**Dissertation submitted to the Faculty of the
Virginia Polytechnic Institute and State University
in partial fulfillment of the requirements for the degree of**

Doctor of Philosophy

in

Electrical Engineering

Yong Xu, Chair

James R. Heflin

Ali Mohamed Okaz

Gary R. Pickrell

Sedki Mohamed Riad

Anbo Wang

December 6, 2012

Blacksburg, Virginia

Keywords: Optical resonator, Microsphere, Fiber taper, Quality factor, Polymer, Nanoparticles, Quantum dots, Nonlinearity.

Silica Microspheres Functionalized with Self-assembled Nanomaterials

Ishac Lamei Nagiub Kandas

(Abstract)

A major limitation of silica-based high-Q microcavities is the lack of functionalities such as gain, plasmonic resonance, and second-order nonlinearity. Silica possesses third order nonlinearity but cannot produce second order nonlinearity, plasmonic resonances, or fluorescence emission. The key to overcome this deficiency is to develop versatile methods that can functionalize the surface of a silica microsphere with appropriate nanomaterials. The goal of this thesis is to present and characterize an electrostatic self-assembly based approach that can incorporate a large number of functional materials onto the surface of a silica resonator with nanoscale control. We consider several types of functional materials: polar ionic self-assembled multilayer (ISAM) films that possess second order nonlinearities, Au nanoparticles (NPs) that support plasmonic resonances, and fluorescent materials such as CdSe/ZnS core/shell QDs.

A major part of this thesis is to investigate the relationship between cavity Q factors and the amount of nanomaterials deposited onto the silica microspheres. In particular, we fabricate multiple functional microspheres with different ISAM film thickness and Au NPs density. We find that the Q factors of these microspheres are mainly limited by optical absorption in the case of the ISAM film, and a combination of optical absorption and scattering in the case of the Au NPs. By controlling the number of polymer layers or

the NPs density, we can adjust the Q factors of these functional microspheres in the range of 10^6 to 10^7 . An agreement between theoretical prediction and experimental data was obtained. The results may also be generalized to other functional materials including macromolecules, dyes, and non-spherical plasmonic NPs.

We also study the adsorption of Au NPs onto spherical silica surface from quiescent particle suspensions. The surfaces consist of microspheres fabricated from optical fibers and were coated with a polycation, enabling irreversible nanosphere adsorption. Our results fit well with theory, which predicts that particle adsorption rates depend strongly on surface geometry. This is particularly important for plasmonic sensors and other devices fabricated by depositing NPs from suspensions onto surfaces with non-trivial geometries.

We use two additional examples to illustrate the potential applications of this approach. First, we explored the possibility of achieving quasi-phase-matching (QPM) in a silica fiber taper coated with nonlinear polymers. Next, we carry out a preliminary investigation of lasing in a silica fiber coated with CdSe/ZnS core/shell quantum dots (QDs).

To my family,

My thesis is lovingly dedicated to my dearest brother, Rizk Kandas.

Acknowledgements

I owe a debt of gratitude to my advisor, **Dr. Yong Xu** for giving me the opportunity to work with him. I would like to thank him for his excellent guidance, caring, patience and encouragement all the time.

I wish to express my thanks to **Prof. Dr. Sedki Riad** for his kindness, most valuable and helpful advices and detailed constructive opinions.

I want to express my great appreciation to **Dr. James R. Heflin and Dr. Hans Robinson** for their constructive discussion and suggestions that helped me a lot.

I would also like to thank the members of my committee for their input: **Prof. Dr. Ali M. Okaz , Dr. Anbo Wang,** and **Dr. Gary Pickrell.**

I owe a debt of gratitude to **Dr. Safwat Mitry , Salwa Mitry,** and their family for supporting me all the time and considering me one of their sons. They were my family in USA.

Finally, I would like to express my thanks to my colleagues: Dr. Chalongrat Daengngam, Dr. Baigang Zhang, Islam Ashry, Dorothy Wang, Aram Lee, Peng Lu, Jeong-Ah Lee for their help on the laboratory work.

Contents

1. Introduction	1
1.1 Motivation.....	1
1.2 Research Objectives.....	4
1.3 Thesis Organization.....	5
References	6
2. Background	8
2.1 WGMs in Spherical Resonator.....	9
2.2 WGMs in Cylindrical Resonator.....	10
2.3 Tapered Optical Fibers (TOFs).....	12
2.4 Self-Assembly.....	14
2.4.1 Introduction	14
2.4.2 Nonlinear Organic Nanomaterial	15
2.4.2.1 Poled (Guest/Host) Polymer Films.....	16
2.4.2.2 Ionic Self-Assembled Multilayer (ISAM) Films.....	16
2.4.2.3 Hybrid Covalent/Ionic Self-Assembled Multilayer Films.....	19
References	21
3. Theoretical Development	27
3.1 Equations of WGMs in Spherical Resonators.....	27
3.1.1 Electromagnetic Fields in Spherical Coordinates System.....	27
3.1.1.1 Radial Dependence of Fields.....	28
3.1.1.2 Polar Dependence of Fields.....	30
3.1.1.3 Azimuthal Dependence of Fields.....	31

3.1.2	Characteristic Equation.....	33
3.2	Q Factor.....	39
3.2.1	Q Factor of Coated Microsphere with Film of Nanomaterial.....	39
3.2.1.1	Wavelength Relative Shift.....	42
3.2.1.2	Q Factor of added Film.....	47
3.2.2	Q Factor of Coated Microsphere with Au NPs.....	49
	References	53
4.	Functionalization and Characterization of Silica Microspheres	55
4.1	Microsphere Fabrication and Experimental Setup.....	55
4.2	Experimental Characterization and Analysis.....	62
	References	74
5.	Irreversible Adsorption of Au NPs on Flat surfaces and Microspheres	76
5.1	Adsorption of NPs.....	76
5.2	Diffusion Model of Irreversible Adsorption of Au NPs on Microspheres.....	77
5.3	Experimental Verification and Analysis.....	80
	References	87
6.	Functionalization of Silica-based Microstructures	90
6.1	Nonlinear Fiber Tapers.....	90
6.1.1	Theory for QPM in a Nonlinear Fiber Taper.....	92
6.1.2	Fabrication and Experimental Setup for QPM Measurement.....	95
6.1.3	SHS in a Periodically Patterned Fiber Taper.....	97
6.2	Quantum Dots (QDs).....	101

6.2.1	Introduction.....	101
6.2.2	CdSe/ZnS core/shell QDs based laser.....	102
	References	106
7.	Conclusion and Future Work	109
7.1	Conclusion.....	109
7.1.1	Functionalization of microsphere surface.....	109
7.1.2	Irreversible Adsorption of Au NPs on Microspheres.....	110
7.1.3	Nonlinear Fiber Tapers.....	110
7.1.4	CdSe/ZnS QDs Based Laser.....	111
7.2	Future Work.....	111

List of Figures

Fig. 1.1 Schemes of light coupling to a microsphere: (a) Tapered optical fiber, (b) integrated waveguide, (c) angle polished fiber, and (d) prism.....	2
Fig. 2.1 Schematic of light coupling from a fiber taper to a cylindrical resonator.....	11
Fig. 2.2 Schematic of fiber taper.....	13
Fig. 2.3 Schematic diagram of multilayer buildup process.....	17
Fig. 2.4 Schematic of ISAM film process. One bilayer process is illustrated and many layers can be formed in the same manner.....	17
Fig. 2.5 Polar orientation of chromophore at the layer surface.....	18
Fig. 2.6 Molecular structure of (a) PB, (b) PCBS, and (c) PAH.....	19
Fig. 3.1 Spherical Bessel function with small indices.....	29
Fig. 3.2 Spherical Bessel function with large indices.....	29
Fig. 3.3 Squared Legendre polynomial representing the angular structure of the modes. The three examples have $l = 50$ and: (a) $m = 50$, (b) $m = 49$, and (c) $m = 48$	32
Fig. 3.4 Coated silica microsphere with film surrounded by air.....	34
Fig. 3.5 Possible solutions for TM modes.....	41
Fig. 3.6 Possible solutions for TE modes.....	41
Fig. 3.7 The radial field distribution: (a) first three modes of TM modes, (b) fundamental modes of TM and TE modes.....	43
Fig. 3.8 TM-to-TE ratio plotted as a function of refractive index of added film.....	48
Fig. 3.9 Percentage of power in the added film for the fundamental modes of TM and TE modes.....	49
Fig. 3.10 Q factor due the absorption on the added film.....	50

Fig. 4.1 Setup for microsphere fabrication.....	56
Fig. 4.2 Microsphere fabrication: (a) melting the fiber by CO ₂ laser beam and stretching it, (b) cutting the fiber with very high power, and (c) forming the microsphere.....	57
Fig. 4.3 SEM images for different number of bilayers of PAH/PCBS: (a) 1Bilayer, (b) 10 Bilayers, (c) 15 Bilayers, and (d) 20 Bilayers.....	59
Fig. 4.4 SEM images for different deposition times of Au NPs on a microsphere: (a) 0.5 min in 10% diluted solution, (b) 20 min. in 10% diluted solution.....	60
Fig. 4.5 Heating the fiber to make a fiber taper.....	60
Fig. 4.6 Software to control the motion stages showing the diameter of taper.....	61
Fig. 4.7 SEM of fiber taper.....	61
Fig. 4.8 Coupling system between the microsphere and fiber taper.....	62
Fig. 4.9 Transmission spectrum of microsphere coated with: (a) 1Bilayer of PAH/PCBS, (B) 5 Bilayers, and (c) 20 Bilayers.....	64
Fig. 4.10 Surface data obtained by AFM on a 500-nm square grid of 768×768 points: (a) 1 Bilayer, (b) 5 Bilayers, and (c) 20 Bilayers.....	65
Fig. 4.11 Theoretical and experimental correlation function: (a) 1 Bilayer, (b) 5 Bilayer, and (c) 20Bilayer of PAH/PCBS.....	67
Fig. 4.12 Surface profile of film after ablation for: (a) 50PAH/PB, and (b) 50PAH/PCBS.....	69
Fig. (4.13): (a) Q factors as a function of film thickness (t) for microsphere coated with PAH/PB and PAH/PCBS, (b) theoretical and experimental result for quality factor due to added film as a function of film thickness (t) for microsphere coated with PAH/PB and PAH/PCBS. The green and black lines are the fitting curves for PAH/PB and	

PAH/PCBS, respectively.....	71
Fig. 4.14 TE-to-TM Q factor ratio plotted as a function of refractive index of surrounding medium.....	72
Fig. 4.15 Theoretical and experimental results for Q factor as a function of Au NPs density on the surface of silica microsphere.....	73
Fig. 5.1 SEM images for different deposition times of Au NPs on a microsphere: (a) 0.5 min in 10% diluted solution, (b) 20 min. in 10% diluted solution, (c) 6 hour in 3% diluted solution, and (d) 12 hours in 3 % diluted solution.....	83
Fig. 5.2 SEM images for different deposition times of Au NPs on flat surface using 30% diluted solution: (a) 5 min. , (b) 20 min., (c)80 min. , and (d) 120 min.....	84
Fig. 5.3 Normalized density of Au NPs for microsphere surface and flat surface.....	86
Fig. 6.1 (a) periodic structure of $\chi^{(2)}$, and (b) corresponding power of SHS.....	94
Fig. 6.2 Theoretical calculation for QPM SHS in fiber taper [21]. Used with permission of Chalongrat Daengngam, 2013.....	95
Fig. 6.3 Schematic of SHG measuring system.....	96
Fig. 6.4 Confocal fluorescence microscope images of a periodic pattern of 20-bilayer PAH/PSS-Dye film coated on a fiber taper: (a) near side and (b) far side.....	98
Fig. 6.5 (a) SHS measured for 10PAH/PB with phase-mismatching (blue line) and with QPM (red line), and (b) measured fiber taper diameter using optical microscope.....	99
Fig. 6.6 (a) removing the coating and maintaining a length about 1 mm at the center, and (b) SHS measured for 10PAH/PB after removing the coating and maintaining a length about 1 mm at the center.....	100

Fig. 6.7 Schematic of coupling system between fiber (microsphere) and fiber taper to study lasing effect.....103

Fig. 6.8 Spectral emissions from cylindrical resonator at different pump power.....104

Fig. 6.9 Comparison between emission of fiber and microsphere coated with 2 bilayers of PAH/(CdSe/ZnS)..... 104

List of Tables

Table 1 rms roughness (nm), correlation length (nm), and quality factor due to surface scattering for different bilayer numbers of PAH/PCBS.....	68
--	----

CHAPTER 1

Introduction

Research on silica-based optical micro-resonators has recently drawn much attention [1]. The majority of such resonators support high-Q whispering gallery modes (WGMs), where optical confinement is provided by total internal reflection at the resonator interface. Due to the exceptionally low material absorption and the extremely smooth surface morphology, the Q factors of the WGMs can often be as high as 10^{10} [1]. Such a high quality factor has led to many interesting applications in areas such as chemical and biological sensing [2], nonlinear optics [3], optomechanics [4], and optofluidics [5]. Despite these advantages, silica-based high Q resonators also face some intrinsic limits. For example, silica possesses neither second order nonlinearity [6] nor plasmonic resonances [7]. Consequently, it is difficult to investigate important processes such as second order parametric oscillation or surface enhanced Raman scattering in such resonators. The key to overcome this deficiency is to develop versatile methods that can functionalize the surface of a silica microsphere with various nanomaterials. In this chapter, we briefly summarize a few key factors of this thesis and outline our motivations and objectives.

1.1 Motivation

Optical resonators have the ability to confine light to a small volume through total internal reflection [8], Bragg reflection (e.g, photonic crystals) [9], and the formation of plasmonic resonances [10]. Most of the silica based resonators rely on total internal reflection to achieve high Q resonances. In this case, light circulates within the resonator

until it returns again in phase to the starting point. Due to the exceptionally smooth silica surface and the extremely low silica absorption, light can be trapped within the resonator for a long time before its energy dissipate from the resonator [11]. The storage capacity of the resonator can be quantified using mode quality factor (Q factor) [12]. Specifically, the Q factor of an optical resonator is proportional to the amount of time light can be trapped within the resonator [12]. To date, silica-based optical resonators tend to exhibit higher Q factors in comparison with other optical micro-cavities [13]. Due to the ease of fabrication, for silica based optical resonators, the most commonly used ones are the silica microspheres and microcylinders, [14]. Light can be coupled to a silica-based microcavity using many methods, such as external couplers made from fiber taper, an integrated waveguide, a prism surface, and angle polished fiber [8, 15]. These methods are depicted in Fig. (1.1) for the case of microsphere. The fiber taper is easy to fabricate and easy to align the coupling. For this reason, we will use the fiber taper method in our work.

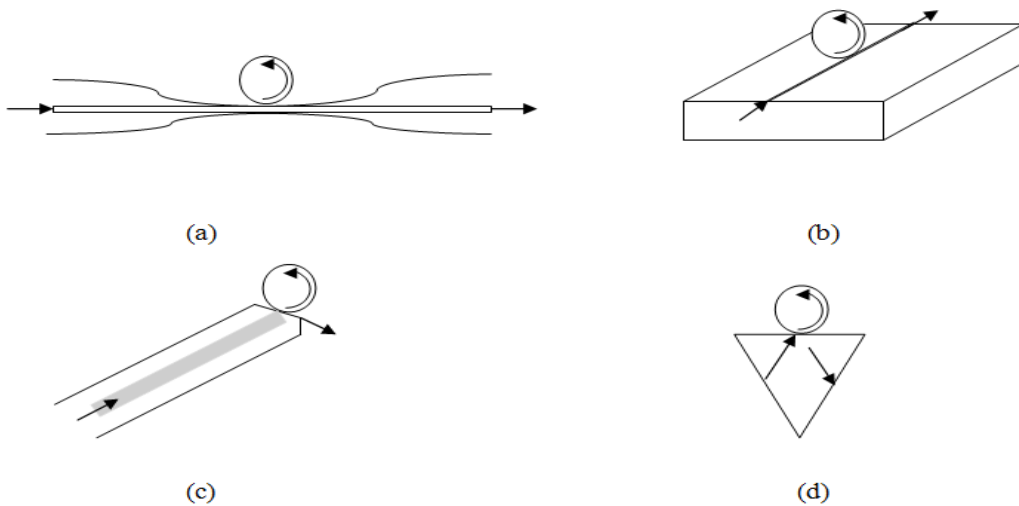


Fig. (1.1) Schemes of light coupling to a microsphere: (a) Tapered optical fiber, (b) integrated waveguide, (c) angle polished fiber, and (d) prism.

As mentioned before, silica material has no second order susceptibility, $\chi^{(2)}$. One of the most common examples of second order nonlinear process is second harmonic generation (SHG). To break the inversion symmetry at the surface of silica microsphere, it can be coated with nonlinear molecules which possess second order nonlinearity. Second order nonlinear optical (NLO) materials are of great importance in current telecommunication networks. Unfortunately, inorganic NLO materials are expensive and difficult to fabricate [16]. So, an alternative approach is organic NLO materials, which is easier to fabrication and can possess comparable second order susceptibility [17, 18]. One such example is ionic self-assembled multilayer (ISAM) films. Compared with other techniques, ISAM method is simple, stable, and inexpensive [17]. ISAM film depends on the alternating adsorption of oppositely charged polymer or dye [17]. Such films can be exceptionally smooth, thermodynamically stable, and possess $\chi^{(2)}$ comparable to that of LiNbO_3 . Furthermore, its absorption coefficient in the standard communication band is relatively small [17]. The method of self-assembly has several important advantages compared with existing methods. First, by depositing one monolayer of nanomaterial at a time, the self-assembly approach can control microsphere functionalization with nanoscale accuracy and maintain exceptional surface smoothness. Secondly, the self-assembly approach relies on electrostatic interaction and is therefore compatible with a wide range of nanomaterials including nonlinear molecules, dyes, quantum dots (QDs), and plasmonic NPs. By selecting appropriate aqueous solutions for self-assembly, we can incorporate a large variety of functional materials (such as polymers and Au NPs) onto the same microsphere, a feature that can be difficult to accomplish using alternative

approaches. Finally, the self-assembly process is simple, straightforward, and can be carried out without using any specialized equipment or clean room.

1.2 Research Objectives

The goal of this thesis is to present and characterize an electrostatic self-assembly-based approach that can incorporate a large number of functional materials onto the surface of silica microsphere and cylindrical resonators with nanoscale control of thickness. The research aims can be summarized as

1. Study the effect of functionalizing the microsphere with thin film of nonlinear material, where we are mainly interested in the relationship between cavity Q factors and the amount of nonlinear materials adsorbed onto the silica surface.
2. Characterize surface smoothness of the nonlinear films to ensure minimal scattering loss. Measuring the thickness of one bilayer and quantify its effect on the absorption loss of the added film.
3. Experimentally verify a diffusion model that can predict the amount of Au NPs assembled over the microsphere surface and the deposition time.
4. Study the relationship between the amount of Au NPs deposited onto the silica microsphere and the cavity Q factors of the functionalized microsphere.
5. Verification of the quasi-phase-matching (QPM) theory applied to fiber taper coated with nonlinear film.
6. Explore potential future applications including quasi-phase-matching (QPM) and lasing.

1.3 Thesis Organization

The structure of the thesis proposal is as follows:

In Chapter 2, we review current research on optical resonators (spherical and cylindrical) and methods of functionalizing the microsphere surface.

The theoretical background on WGMs in spherical resonators is presented in Chapter 3. The Q factor, the characteristic equation, the positions of resonance, and scattering due to surface roughness are discussed. The effect of coating a microsphere with polymeric material or NPs is studied too. Finally, a simple theory for irreversible adsorption of NPs on a surface is presented.

In Chapter 4, we present various experimental procedures including microsphere fabrication, fiber taper fabrication, Q factor measurements, and the self-assembly of polymer, dye, and NPs. Chapter 4 contains also the results of measured Q factor, including the Q factor of a microsphere coated with polymer, dye multilayers, and Au NPs.

In Chapter 5, we present a theoretical model and experimental data on the relationship between the Au NPs density (deposited on a silica microsphere) and the deposition time

In Chapter 6, we present preliminary results on two potential future directions. One deals with QPM using a fiber taper coated with nonlinear films. The other is the possibility of lasing in a silica cylinder coated with 5-nm CdSe/ZnS core/shell QDs.

Finally, the conclusion and future research work for the following period of research are presented in Chapter 7

References

- [1] M. L. Gorodetsky, A. A. Savchenkov, and V. S. Ilchenko, Ultimate Q of optical microsphere resonators, *Opt. Lett.* **21**, 453-455 (1996).
- [2] Hai-Cang Ren, Frank Vollmer, Stephen Arnold and Albert Libchaber, High-Q microsphere biosensor-analysis for adsorption of rodlike bacteria, *Opt. Express.* **15**, 17410-17423 (2007).
- [3] Gregory Kozyreff, Jorge Luis Dominguez-Juarez, and Jordi Martorell, Nonlinear optics in spheres: from second harmonic scattering to quasi-phase matched generation in whispering gallery modes, *Laser Photonics Rev.* **5**, 737-749 (2011).
- [4] T.J. Kippenberg and K.J. Vahala , Cavity Opto-Mechanics, *Opt. Express* **15**, 17172-17205 (2007).
- [5] Jonathan D. Suter, *et al.*, PDMS embedded opto-fluidic microring resonator lasers, *Opt. Express.* **16**, 10248-10253 (2008).
- [6] Yong Xu, Anbo Wang, James R. Heflin, and Zhiwen Liu, Proposal and analysis of a silica fiber with large and thermodynamically stable second order nonlinearity, *Appl. Phys. Lett.* **90**, 211110 (2007).
- [7] S.I Shopova, C.W Blackledge, and A.T Rosenberger, Enhanced evanescent coupling to whispering-galley modes due to gold nanorods grown on the microresonator surface, *Appl. Phys. B* **93**, 183-187(2008).
- [8] Alessandro Chiasera, *et al.*, Spherical whispering-gallery-mode microresonators, *Laser Photon. Rev.* **4**, 457-482 (2010).
- [9] Jacob Scheuer and Amnon Yariv, Optical annular resonators based on radial Bragg and photonic crystal reflectors, *Opt. Express* **11**, 2736-2746 (2003).

- [10] Nicolas Large, *et al.*, Plasmonic properties of gold ring-disk nano-resonators: fine shape details matter, *Opt. Express* **19**, 5587-5595 (2011).
- [11] Ming Cai, *Optical Fiber Taper Coupled Glass Microsphere Resonator*, California Institute of Technology, 2001.
- [12] Juha-Pekka Laine, *Design and Applications of Optical Microsphere Resonators*, Helsinki University of Technology, 2003.
- [13] Andrey B. Matsko and Vladimir S. Ilchenko, Optical Resonators with Whispering-Gallery Modes-Part I: Basics, *IEEE J. Quantum Electron.* **12**, 3-14 (2006).
- [14] George Farca, *Cavity-Enhanced Evanescent-Wave Chemical Sensing Using Microresonators*, Oklahoma State University, 2006.
- [15] A. Mazzei, *et al.*, Optimization of prism coupling to high-Q modes in a microsphere resonator using a near-field probe, *J. Opt. Commun.* **250**, 428-433 (2005).
- [16] Kai Chen, *et al.*, Interface effects in plasmon-enhanced second-harmonic generation from self-assembled multilayer films, *J. Opt. Soc. Am. B* **27**, 92-98(2010).
- [17] Akhilesh Garg, *Organic Self-Assembled Films for Nonlinear Optics: Film Structure, Composition and Kinetic of Film Formation*, Virginia Polytechnic Institute and State University, 2008.
- [18] Chalongrat Daengngam, *Second-Order Nonlinear Optical Responses in Tapered Optical Fibers with Self-Assembled Organic Multilayers*, Virginia Polytechnic Institute and State University, 2012.

CHAPTER 2

Background

Optical resonators have found numerous applications in nonlinear optics, optical signal processing, and sensing [1]. It is of course use two mirrors to form optical resonators [2]. However, it is difficult to use this approach to form high Q resonators with micro- or nano-scale sizes., Among current approaches of fabricating high-Q optical microcavities, a particularly attractive method is silica-based resonators, which often rely on total internal reflection to achieve high Q operation [1]. Extremely high Q factor in a very small volume can be easily achieved which makes the resonator easy to be tuned, stable, and integrated in the optical networks [2]. Many different geometries have been demonstrated in current literature. Among those, the simplest and cheapest ones are: rings, cylinders, and spheres. The modes generated in an optical resonator are called whispering gallery modes (WGMs) [3].

The history of WGMs can be traced to 1912, when Rayleigh considered the sound waves traveling with high efficiency inside the walls of an oval structure. The term “whispering gallery” comes from the ability to hear whispers over a great distance in a domed cathedral [4]. C.V Raman as well made some study on the same cathedral in 1921[5]. Since this time WGMs attracted the scientists’ attention and have been studied at optical, sound, and microwave wavelengths in applications with different geometries such as cylindrical and spherical shapes [1, 6]. In Ref [7], R. D. Richtmyer studied the resonant frequencies and the losses of dielectric resonators of ring and sphere shapes. A. B. Matsko and V. S. Ilchenko demonstrated WGMs in solid state spherical cavity and obtained high Q factors in the range of 10^8 - 10^9 [2]. Laser emission was confirmed using

ethanol droplet containing Rhodamine 6G dye [8]. In Ref [9], Stimulated Raman Scattering (SRS) was studied and was observed for three different materials droplets: H₂O, D₂O, and ethanol. Many studies have been done in WGMs and its applications in measurement of particle size, refractive index, shape, temperature change, pressure change, and absorption of surrounding medium depending on the change of WGMs resonant frequencies [2, 10]. WGM resonators have numerous applications in Ref [1], depending on its geometry and resonant properties [11]. Four major applications of optical resonators were reviewed in Ref [11], which are strong-coupling cavity quantum electrodynamics (QED), enhancement and suppression of spontaneous emission, and dynamic filters in optical communications. Vladimir S. Ilchenko and Andrey B. Matsko discussed the optical and photonic applications of WGMs optical resonators in some details [10]. They presented many applications of WGMs such as optical and photonic signal resonator filters [12], and spectroscopy and analysis of chemical and biological agents [13].

2.1 WGMs in Spherical Resonator

Spherical resonators can support optical modes with complex radial, equatorial, and polar dependence [4]. The existence of WGMs near to the surface makes their Q factor strongly dependent on the surface roughness and interfacial blemishes [14]. All WGMs can be described by three integers (n, m, l) . n ($=1, 2, \dots$) is the radial mode number which represents the number of maxima along the radial direction, while l ($= 0, 1, \dots$) is the polar mode number, and m ($= -l, \dots, 0, \dots, l$) is the azimuthal mode number [15]. Opposite values of m correspond to modes propagating in opposite direction. The modes with $m \approx l$ and $n = 1$ are of particular importance and are called the fundamental WGMs. These modes

have strong confinement, high Q factor, smallest mode volume and, thus, high electric field per photon. Many applications are based on these modes, e.g., low threshold laser, and integrated optical devices. The small mode volume is also essential for cavity QED related applications [14, 16].

The Q factor of any WGM is determined by the loss mechanisms of the resonator. Generally, there are four loss mechanisms: radiative losses, scattering losses due to surface roughness and inhomogeneity, losses caused by surface contaminants and material losses (absorption loss), and coupling losses [17, 18]. The radiative losses are very small when the microsphere diameter is much greater than the resonance wavelength, (e.g., by a factor of 15 or greater) [1]. The contaminants losses are induced during the fabrication process [17]. In the absence of contaminants, the Q factor of a large diameter sphere is limited by the material losses [18]. The latter are associated with absorption and bulk Rayleigh scattering in the material of the resonator. Also, if we add a layer to the surface of the resonator, scattering and absorption loss should be added too. Finally, in the majority of applications, it is necessary to couple input signal into the optical resonator using fibers taper, waveguides, or prisms. In this case, coupling between the high Q resonator and tapers / waveguides / prisms can also incur coupling loss.

2.2 WGMs in Cylindrical Resonator

WGMs can be generated when light is coupled from a fiber taper to a standard cylindrical silica fiber (Fig. (2.1)). In this case, the excitation of WGMs can be inferred from dips in the transmission spectrum of the fiber taper.

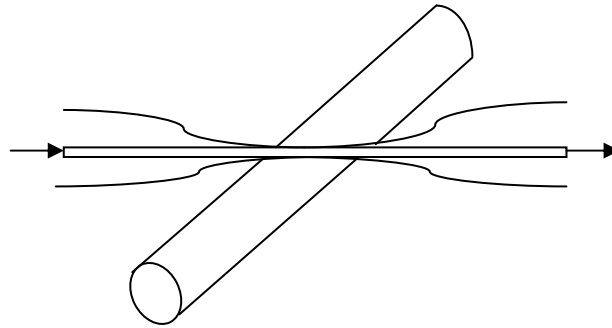


Fig. (2.1) Schematic of light coupling from a fiber taper to a cylindrical resonator.

These dips are symmetric and narrow in the case of microspheres. A cylindrical resonator can cause asymmetric and wide dips in the transmission spectrum [19]. This disadvantage can limit the applications of a cylindrical resonator as a sensor. Biological and chemical sensor applications require narrow linewidth to achieve low detection limits. The other major disadvantage of cylindrical resonators is the lack of light confinement along the longitudinal axis [19]. Although theoretically a Q factor of the order 10^5 can be achieved for standard communication fiber as a resonator, but in practical case 10^3 or 10^4 is maximally obtained [20].

Despite the low sensitivity of cylindrical resonators, the latter have some advantages over microsphere resonators. First, they are made of standard optical fiber of fixed diameter, which provides better repeatability. Second, they are easier to be aligned because we need only the cylindrical resonator to be perpendicular to the fiber taper [21]. Microcapillaries are considered type of cylindrical resonator in which a liquid or gas can flow in a hollow cylindrical. They are particularly useful for label-free biosensing applications [22]. Microcapillaries have some advantages over other resonators such as microsphere and microring resonators [19]. First, they do not need liquid cell containing it. The spatial separation between where the total internal reflection occurs (the outer surface) and where the evanescent wave interacts with fluid (the inner surface) is actually

advantageous. It is also possible to increase the Q factor by increasing the refractive index of the fluid inside the cavity, which makes it a tunable microcavities and highly sensitive refractmeters [19]. It is worthy to notice that, the radius and the wall thickness of the capillary can affect its sensitivity [16]. A sensitivity of 850 nm/RIU was achieved for water solutions [19] using a capillary with wall thickness of 1.64 μm and diameter of 55.6 μm . Much smaller values were reported for microsphere resonators (30 nm/RIU) and microring resonators (140 nm/RIU) using a glucose solution [23].

2.3 Tapered Optical Fibers (TOFs)

TOFs consists of three parts: one is the waist or tapered region, two conical transition regions with gradually increasing diameter, and the third is the untapered region [24, 25] (Fig. (2.2)). A model of the shape of TOFs was presented in Ref [26]. The tapered region can be fabricated to have a diameter of some micrometers or even submicrons. The length of tapered region is generally several millimeters. If the light propagating in the fiber taper remains in a single spatial mode, the taper is called adiabatic [6]. Due to the small diameter of TOF at the center of tapered region, the evanescent field at the surface is much larger than that obtained from normal fibers and light is confined in a very small core [27]. Consequently, it is possible to achieve strong interaction between the guided optical field and the surrounding medium. This feature can be very useful for sensing applications, including label-free detection of biomolecules [25], humidity sensors [28], long period-based grating sensors (LPGs), sensors for temperature and refractive index using Mach-Zehnder interferometer [29].

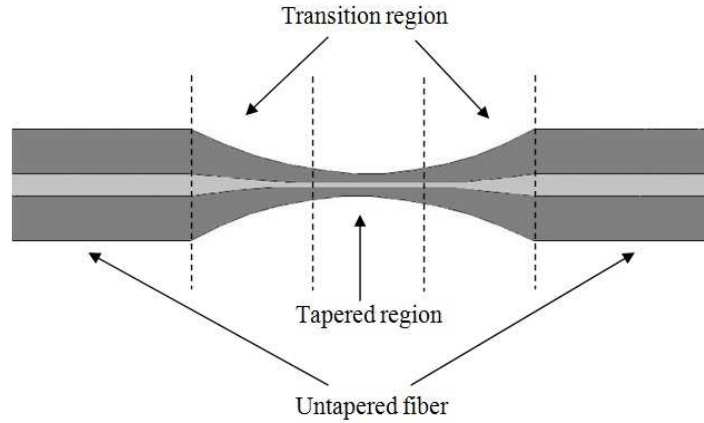


Fig. (2.2). Schematic of fiber taper.

In addition, TOFs can be used in nonlinear applications such as studying the nonlinear transmission of TOF surrounded by rubidium vapor [30], third harmonic generation [31], and enhanced Kerr nonlinearity in AS_2Se_3 chalcogenide TOFs [32].

Strong evanescent field generated in the TOFs allows the light coupling from fiber taper to high Q factor optical resonators of different geometries [11]. It is one of the simplest and most efficient ways to couple light in and out of optical resonators. Coupling light from TOF into high Q factor microsphere was investigated analytically [33]. External coupling Q factor values and intrinsic WGMs loss were derived in numerous formulas.

Some drawbacks of the TOFs should also be mentioned. The diameter of the fiber taper is very small (several micrometers), which makes it mechanically fragile. [33]. Also, when the air-silica boundary is contaminated, taper transmission can be reduced by a significant amount [30].

2.4 Self-Assembly

2.4.1 Introduction

By coating a resonator with appropriate molecules, we can change its surface properties and open the door for numerous sensing applications, especially biosensing applications [34]. However, this functional layer has to be thin and homogeneous in order to keep the Q factor of a WGM at a high value. The Q factor depends on the functional layer and the medium surrounding the resonator [34]. In Ref [35], a layer-by-layer technique (LbL) was used to coat a silica microsphere with emissive thin films of poly (phenylene, ethynylene). The microsphere becomes highly emissive and has fluorescence properties comparable to those of the corresponding polymers in solution and shows enhanced quenching [35]. Also, a major application of microsphere resonators is in cavity QED. If QDs are deposited to the surface of a microsphere, these particles may reduce the Q factor by destroying the smooth surface and can have a weak interaction with the external evanescent field of a WGM. Coating a microsphere with poly (methyl, methacrylate) (PMMA) can preserve the Q factor high value, tune the optical mode in the cavity, and draw the maximal field to the interface where the QDs are located [36]. Coating a microsphere with a conjugated polymer film opens the door for using it in switching applications. A shift of 3.2 GHz in the resonance frequency was achieved when the coated microsphere was pumped by a diode laser at 405 nm with power density of 10^4 mW/cm² due to the coating layer [37].

Noble metal NPs, such as silver or gold, have a unique optical property known as localized surface plasmon resonance (LSPR). This effect is caused by oscillations of metal electrons in resonance with an incident certain frequency [38, 39]. By coating the

microsphere with gold nanorod (NR) particles, Shopova *et al.* enhanced the coupling between the microsphere and fiber taper by factor up to 100 at 830 nm [39]. This coupling enhancement is attributed to the LSPR enhancement of the localized WGM field at the surface. Also, in Ref [40] S. I. Shopova, *et al.*, enhanced the WGMs sensitivity as a biosensor for the detection of individual NPs in an aqueous solution. When dielectric NPs interacted with plasmonic NPs bound to the surface at the equator, they observed a frequency shift that resulted in an enhancement by factor 4.

As silica glass is a centrosymmetric material, it cannot possess any second-order nonlinearity. A silica microsphere coated with nonlinear polymer molecules enhances strong second-order nonlinear responses [41].

2.4.2 Nonlinear Organic Nanomaterial

As mentioned before, for certain applications, organic NLO materials can be more suitable than nonorganic materials. To have strong second order nonlinearity, NLO should have noncentrosymmetric order of the polarizable chromophoric molecules [42] but its fabrications and processing techniques are difficult and expensive [43]. On other hand, temporal and thermally stability can limit the performance of NLO films [42]. Recently, fabrication of stable NLO film with nonlinear property has been studied due to its high nonlinear susceptibility, and low fabrication cost [42-45]. There are many methods that can produce second order nonlinearity in organic films, including Electric field poling, Langmuir-Bodgett (LB), and covalent self assembly. The common drawback between them is the low temporal and mechanical stability [44]. In recent years, Heflin, *et al.*, have developed a layer-by-layer (LbL) technique that can produce second order nonlinearity if the chromophore molecules (dye molecules) can be oriented in a polar

manner [45]. Furthermore, LbL technique can introduce higher thermal and temporal stability than the poled polymers. Alternative adsorption of polycations and polyanions using Lbl fashion has been introduced as simple and powerful way to change the surface properties [46]. Films formed by ionic self-assembled multilayer (ISAM) are also called Polyelectrolyte multilayers [45, 46].

Briefly, different techniques of making organic NLO materials are discussed below:

2.4.2.1 Poled (Guest/Host) Polymer Films

In this technique, we have two polymer complex (Host) and chromophore (Guest). Electric field poling is applied to the host to align the guest. The active chromophore is embedded in a polymer complex and the system heated to a temperature higher than the glass transition temperature. Strong electric field is then applied ($\sim 10^5$ - 10^6 V/m) in order to align the chromophore [43]. K. D. Singer *et al.* observed second harmonic generation in organic polymer glasses poled with electric field [47]. A second harmonic coefficient, d_{33} of $6 \pm 1.3 \times 10^{-9}$ esu at 1580 nm was reported. Thermodynamic model for the poling process and second harmonic coefficient was developed and a good agreement was achieved.

Host/Guest poled polymer method produced NLO with reasonable nonlinearity. However, issues with thermal / temporal stability and poor mechanical stability have limited the practical applications of these materials [42, 43].

2.4.2.2 Ionic Self-Assembled Multilayer (ISAM) Films

Multilayer assembly of polymers was developed two decades ago [48]. This process relies on alternative adsorption of anionic polyelectrolyte and cationic polyelectrolyte on charged solid substrate, which are illustrated in Fig. (2.3) and (2.4). As shown in Fig. 2.4,

the glass slide is normally charged with negative charges. This slide is immersed in an aqueous solution containing a positively charged polyelectrolyte (polycation).

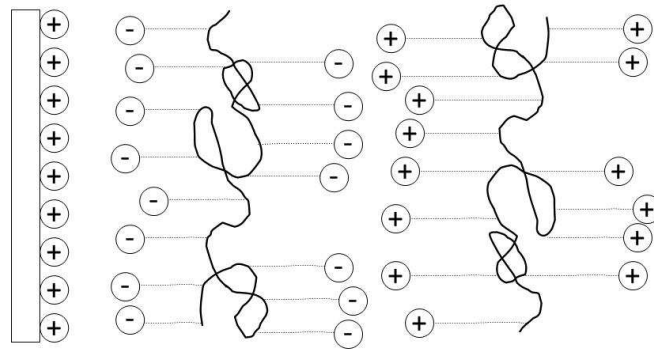


Fig. (2.3) Schematic diagram of multilayer buildup process.

The formation of a monolayer of polycation reverses the surface charge polarity. Then, the substrate is rinsed in DI water to remove the loosely bound excess polymers. Next step is to immerse the substrate in another aqueous solution containing negatively charged polyelectrolyte (polyanion), followed by DI water rinsing. Another monolayer of negatively charged polyelectrolyte is formed, which establishes a single bilayer. Many numbers of bilayers can be obtained as many times as desired by repeating this procedure.

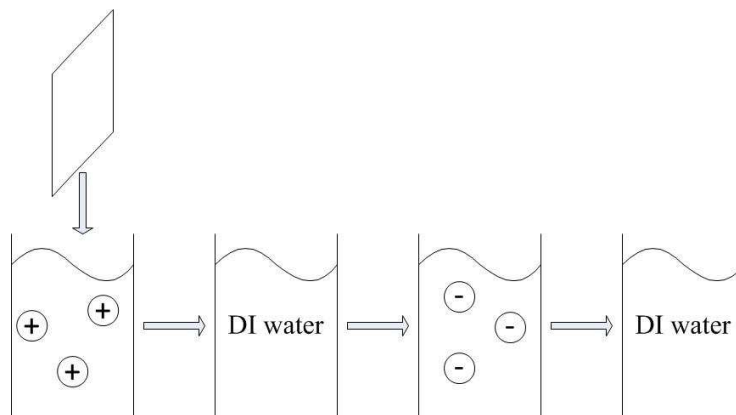


Fig. (2.4) Schematic of ISAM film process. One bilayer process is illustrated and many layers can be formed in the same manner.

There are no restrictions for the size of the glass substrate. Also, many polyelectrolytes can be used in the same to buildup many bilayers as long as the oppositely charged polymers are used sequentially [48]. Polar orientation of NLO chromophore is achieved at the interface of layers whereas random orientation is dominant in the bulk film (Fig. (2.5)).

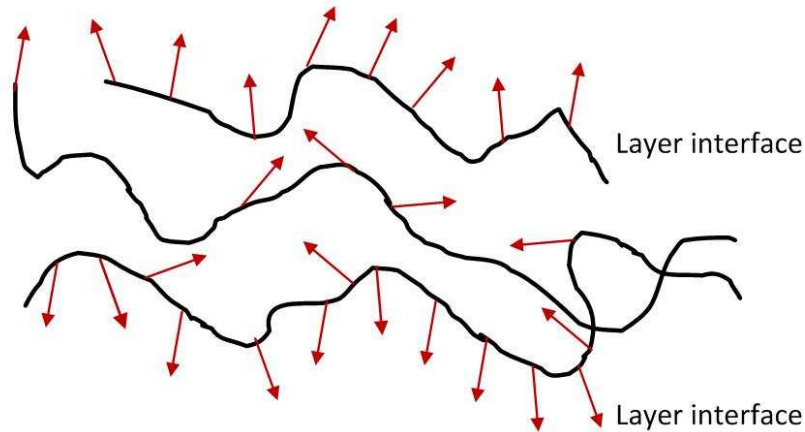


Fig. (2.5) Polar orientation of chromophore at the layer surface.

ISAM films made of nonlinear nonmaterial can exhibit second order nonlinearity. As demonstrated in Ref [42, 45], Reactive dye such as Procion Brown (PB)(Fig. (2.6-a)) and poly {1-[p-(3'-carboxy-4'-hydroxyphenylazo) benzenesulfonamido]-1, 2-ethandiyl} (PCBS) (Fig. (2.6-b)) can be used to form ISAM films with layer of poly (allylamine hydrochloride) (PAH) (Fig. (2.6-c)). More specifically, Heflin, *et al.* demonstrated a fabrication of 600 bilayers of PAH/PCBS on glass substrates using alternating deposition technique [45]. The films have long polar orientation of chromophores and are optically homogenous. It was shown that different deposition parameters such as pH value of PAH and PCBS solutions, solvent quality, and rinsing times affect strongly the optical prosperities of ISAM films. The PAH/PCBS film can exhibit temporal stability with no

decay of $\chi^{(2)}$ for long time (can reach ten years in ambient conditions) [24]. The second harmonic intensity can be an indicator for the polar orientation of chromophores. When the film layer thickness is small (less than 10 μm), the second harmonic intensity is supposed to increase quadratically with the film thickness [43].

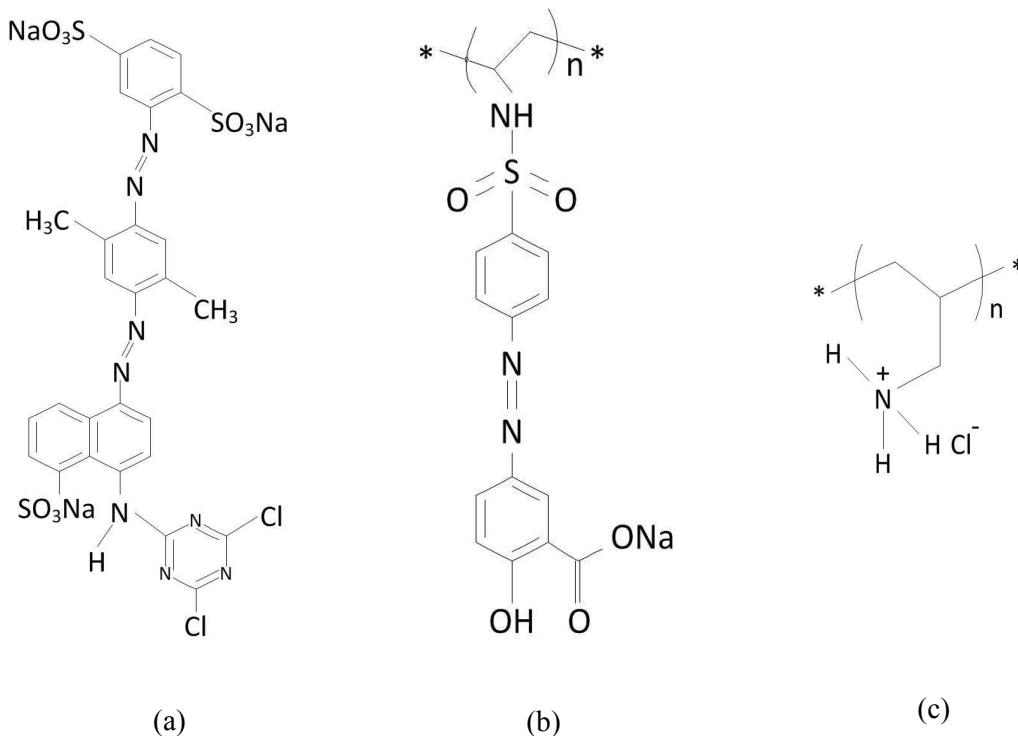


Fig. (2.6) Molecular structure of: (a) PB, (b) PCBS, and (c) PAH.

2.4.2.3 Hybrid Covalent/Ionic Self-Assembled Multilayer Films

For stronger polar orientation of chromophores, water soluble reactive dye (PB MX-GRN) can be used [42, 49]. The hybrid covalent/electrostatic layer-by-layer self assembly was applied to fabricate NLO stable films of PAH and PB. PB contains two different groups as shown in Fig. (2.6-a). One of them is sulfonate, and the other is

dichlorotriazine on each end. The dichlorotriazine group is responsible for the covalent binding with neutral PAH, while the sulfonate group is responsible for the ionic binding with ionized PAH. The control of PAH ionization can be achieved by changing the pH value of the solution. The pH value for PB should be 10.5. At this value, the covalent bonds formation is more efficient. Adding another monolayer of PAH (with pH 7), the sulfonates (negatively charged) form ionic bonds with protonated amine groups of PAH. The second order susceptibility peaked (increased to 250 %) when 0.5 M of NaCl salt is added to the PB solution. This is due to the increased shielding of the PB charges which lead to higher density of chromophore in the film bilayer. The electrooptic coefficient of PAH/PB can reach 14 pm/V which is about the half of the value for lithium niobate. These films also show high temporal stability, and thermal stability upon time. With these interesting features, ISAM films made of PAH/PB are promising for the EO modulator applications.

References

- [1] Alessandro Chiasera, *et al.*, Spherical whispering-gallery-mode microresonators, *Laser Photon. Rev.* **4**, 457-482 (2010).
- [2] Andrey B. Matsko and Vladimir S. Ilchenko, Optical Resonators with Whispering-Gallery Modes-Part I: Basics, *IEEE J. Quantum Electron.* **12**, 3-14 (2006).
- [3] Ming Cai, Optical Fiber Taper Coupled Glass Microsphere Resonator, California Institute of Technology, 2001.
- [4] Juha-Pekka Laine, Design and Applications of Optical Microsphere Resonators, Helsinki University of Technology, 2003.
- [5] C. V. Raman and G. A. Sutherland, On the whispering-gallery phenomenon, *Proc. R. Soc. Lond. A* **100**, 424-428 (1922).
- [6] George Farca, Cavity-Enhanced Evanescent-Wave Chemical Sensing Using Microresonators, Oklahoma State University, 2006.
- [7] R. D. Richtmyer, Dielectric Resonators, *J. Appl. Phys.* **10**, 391-398 (1939).
- [8] H. M. Tzeng, K. F. Wall, M. B. Long, and R. K. Chang, Laser emission from individual droplets at wavelengths corresponding to morphology-dependent resonances, *Opt. Lett.* **9**, 499-501 (1984).
- [9] Judith B. Snow, Shi-Xiong Qian, and Richard K. Chang, Stimulated Raman scattering from individual water and ethanol droplets at morphology-dependent resonances, *Opt. Lett.* **10**, 37-39 (1985).
- [10] Vladimir S. Ilchenko and Andrey B. Matsko, Optical Resonators With Whispering-Gallery Modes—Part II: Applications, *IEEE J. Quantum Electron.* **12**, 15-32 (2006).
- [11] Kerry Vahala, Optical Microcavities, *Nature* **424**, 839-846 (2003).

- [12] P. Rabiei, W. H. Steier, C. Zhang, and L. R. Dalton, Polymer microring filters and modulators, *J. Lightw. Technol.* **20**, no. 11, 1968–1975 (2002).
- [13] F. Vollmer, S. Arnold, D. Braun, I. Teraoka, and A. Libchaber, Multiplexed DNA quantification by spectroscopic shift of two microsphere cavities, *J. Biophys.* **85**, 1974–1979 (2003).
- [14] Kerry Vahala, *Optical Microcavities*, Stallion Press, Singapore, 2004.
- [15] Tobias Jan August Kippenberg, *Nonlinear Optics in Ultra-high-Q Whispering Gallery Optical Microcavities*. California Institute of Technology, 2004.
- [16] A. Mazzei, S. Götzinger, L. de S. Menezes, V. Sandoghdar, and O. Benson, Optimization of prism coupling to high-Q modes in a microsphere resonator using a near-filed probe, *J. Opt. Commun.* **250**, 428-433 (2005).
- [17] Alessandro Chiasera, *et al.*, Spherical whispering-gallery-mode microresonators, *Laser Photon. Rev.* **4**, 457-482 (2010).
- [18] M. L. Gorodetsky, A. A. Savchenkov, and V. S. Ilchenko, Ultimate Q of optical microsphere resonators, *Opt. Lett.* **21**, 453-455 (1996).
- [19] Vanessa Zamora, Antonio Díez, Miguel V. Andrés, and Benito Gimeno, Cylindrical optical microcavities: Basic properties and sensor applications, *Photonics and Nanostructures – Fundamentals and Applications* **9**, 149–158(2011).
- [20] Anna Boleininger, Thomas Lake, Sophia Hami and Claire Vallance, Whispering Gallery Modes in Standard Optical Fibres for FibrProfiling Measurements and Sensing of Unlabelled Chemical Species, *Sensors* **10**, 1765-1781(2010).

- [21] G. Farca, S. I. Shopova, and A. T. Rosenberger, Cavity-enhanced laser absorption spectroscopy using microresonator whispering –gallery modes, *J. Opt. Express* **15**, 17443-17448 (2007).
- [22] Hao Li and Xudong Fan, Characterization of sensing capability of optofluidic ring resonator biosensors, *Appl. Phys Lett.* **97**, 011105:1-3 (2010).
- [23] Vanessa Zamora, Antonio Díez, Miguel V. Andrés and Benito Gimeno, Refractometric sensor based on whisperinggallery Modes of thin capillaries, *Opt. Express* **15**, 12011-12016 (2007).
- [24] Chalongrat Daengngam, Second-Order Nonlinear Optical Responses in Tapered Optical Fibers with Self-Assembled Organic Multilayers, Virginia Polytechnic Institute and State University, 2012.
- [25] Ye Tian, Wenhui Wang, Nan Wu , Xiaotian Zou and Xingwei Wang, Tapered Optical Fiber Sensor for Label-Free Detection of Biomolecules, *Sensors***11**, 3780-3790 (2011).
- [26] Timothy A. Birks and Youwei W. Li, The Shape of Fiber Tapers, *IEEE J. Lightwave Tech.* **10**, 432-438(1992).
- [27] T. A. Birks, W. J. Wadsworth, and P. St. J. Russell, Supercontinuum generation in fiber tapers, *Opt. Lett.* **25**, 1415-1417 (2000).
- [28] Jes´us M. Corres, Francisco J. Arregui, Ignacio R. Mat´ias, Sensitivity optimization of tapered optical fiber humidity sensors by means of tuning the thickness of nanostructured sensitive coatings, *Sensors and Actuators B* **122**, 442–449(2007).

- [29] Ping Lu, Liqiu Men, Kevin Sooley, and Qiying Chen, Tapered fiber Mach–Zehnder interferometer for simultaneous measurement of refractive index and temperature, *Appl. Phys. Lett.* **94**, 131110:1-3 (2009).
- [30] S. M. Hendrickson, T. B. Pittman and J. D. Franson, Nonlinear transmission through a tapered fiber in rubidium vapor, *J. Opt. Soc. Am. B* **26**, 267-271 (2009).
- [31] D.A. Akimov, *et al.*, Generation of a spectrally asymmetric third harmonic with unamplified 30-fs Cr:forsterite laser pulses in a fiber taper, *Appl. Phys. B* **76**, 515-519 (2003).
- [32] E. C. Mägi, L. B. Fu, H. C. Nguyen, M. R. E. Lamont, D. I. Yeom, and B. J. Eggleton, Enhanced Kerr nonlinearity in sub-wavelength diameter As₂Se₃ chalcogenide fiber tapers, *Opt. Express* **15**, 10324-10329 (2007).
- [33] Juha-Pekka Laine, Design and applications of optical microsphere resonators, Helsinki University of Technology, 2003.
- [34] S. Soria, F. Baldini, S. Berneschi, F. Cosi, A. Giannetti, G. Nunzi Conti, S. Pelli, G. C. Righini, and B. Tiribilli, High-Q polymer-coated microspheres for immunosensing applications, *Opt. Express* **17**, 14694-14699 (2009).
- [35] Jordan H. Wosnick, Jessica H. Liao, and Timothy M. Swager, Layer-by-Layer Poly(phenylene ethynylene) Films on Silica Microspheres for Enhanced Sensory Amplification, *Macromolecules* **38**, 9287- 9290 (2005).
- [36] C. H. Dong, F. -W. Sun, C. -L. Zou, X. -F. Ren, G. -C. Guo, and Z. -F. Han, High-Q silica microsphere by poly(methyl methacrylate) coating and modifying, *App. Phys. Lett.* **96**, 061106:1-3(2010).

- [37] H. C. Tapalian, J. -P. Laine, and P. A. Lane, Thermo-optical Switches Using Coated Microsphere Resonators, *IEEE Photon. Technol. Lett.* **14**, 1118-1120 (2002).
- [38] Zhenda Lu, James Goebel, Jianping Ge, and Yadong Yin, Self-assembly and tunable plasmonic property of gold nanoparticles on mercapto-silica microspheres, *J. Mater. Chem.* **19**, 4597-4602 (2009).
- [39] S. I. Shopova, C. W. Blackledge, and A. T. Rosenberger, Enhanced evanescent coupling to whispering-gallery modes due to gold nanorods grown on the microresonator surface, *Appl. Phys. B* **93**, 183-187 (2008).
- [40] S. I. Shopova, R. Rajmangal, S. Holler, and S. Arnold, Plasmonic enhancement of whispering-gallery-mode biosensor for single nanoparticle detection, *Appl. Phys. Lett.* **98**, 243104 :1-3 (2011).
- [41] Yong Xu, *et al.*, Second Order Parametric Process in Nonlinear Silica Microspheres, *Phys. Rev. Lett.* **100**, (2008).
- [42] James R. Hefflin, *et al.*, Efficient, Thermally Stable, Second Order Nonlinear Optical Response in Organic Hybrid Covalent/Ionic Self-Assembled Films, *Langmuir* **22**, 5723-5727 (2006).
- [43] Akhilesh Garg, Organic Self-Assembled Films for Nonlinear Optics: Film Structure, Composition and Kinetic of Film Formation, Virginia Polytechnic Institute and State University, 2008.
- [44] Kevin E. Van Cott, *et al.*, Layer-By-Layer Deposition and Ordering of Low-Molecular-Weight Dye Molecules for Second-Order Nonlinear Optics, *Angew. Chem. Int. Ed.* **41**, 3236 - 3238 (2002).

- [45] Akhilesh Garg, *et al.*, Polar orientation of a pendant anionic chromophore in thick layer-by-layer self-assembled polymeric films, *Appl. Phys.* **104**, 053116:1-8 (2008).
- [46] K. Lowack and C. A. Helm, Molecular Mechanisms Controlling the Self-Assembly Process of Polyelectrolyte Multilayers, *Macromolecules* **31**, 823-833 (1998).
- [47] K. D. Singer, J. E. Sohn, and S. J. Lalama, Second harmonic generation in poled polymer films, *Appl. Phys. Lett.* **49**, 248-250 (1986).
- [48] G. Decher, J. D. Hong and J. Schmitt, Buildup of ultrathin multilayer films by a self-assembly process: III. Consecutively alternating adsorption of anionic and cationic polyelectrolytes on charged surfaces, *Thin Solid Films* **210/211**, 831-835(1992).
- [49] K. Z. Wanga, C. H. Huanga, D. J. Zhoua, G. X. Xua, Y. Xub. Y. Q. Liub, D. B. Zhub, X. S. Zhaoc, and X. M. Xiec, Second-order nonlinear optical property of Langmuir-Blodgett film prepared from A novel ferrocenyl-containing Kanthanide complex, *Solis State Communications* **93**, 189-191 (1995).

CHAPTER 3

Theoretical Development

3.1 Equations of WGMs in Spherical Resonators

3.1.1 Electromagnetic Fields in Spherical Coordinates System

The optical WGMs in a spherical resonator should satisfy the Helmholtz equation [1].

Consider the scalar wave equation

$$\nabla^2 \psi(r, \theta, \varphi, t) - \frac{1}{v^2} \frac{\partial^2 \psi(r, \theta, \varphi, t)}{\partial t^2} = 0, \quad (3.1)$$

where $\psi(r, \theta, \varphi, t)$ can represent the electrical field or magnetic field, and v is the phase velocity in the medium. By assuming harmonic time dependence, it can be written as

$$(\nabla^2 + k^2 n^2) \psi(r, \theta, \varphi) = 0, \quad (3.2)$$

where k is the wavevector in free space, and n is the refractive index of the medium. In spherical coordinates, we can rewrite Eq. (3.2) as

$$\frac{1}{r^2} \frac{\partial^2}{\partial r^2} (r\psi) + \frac{1}{r \sin(\theta)} \frac{\partial}{\partial r} \left(\sin(\theta) \frac{\partial}{\partial \theta} \psi \right) + \frac{1}{r^2 \sin^2(\theta)} \frac{\partial^2}{\partial \varphi^2} \psi + n^2 k^2 \psi = 0. \quad (3.3)$$

From separation of variables, we obtain

$$\psi(r, \theta, \varphi) = \psi_r(r) \psi_\theta(\theta) \psi_\varphi(\varphi), \quad (3.4)$$

where $\psi_r(r)$ is the radial field, $\psi_\theta(\theta)$ represents the polar field, and $\psi_\varphi(\varphi)$ represents the azimuthal component of the field.

3.1.1.1 Radial Dependence of Fields

The radial component satisfies the following equation:

$$\left[\frac{d^2}{dr^2} + \frac{2}{r} \frac{d}{dr} + n^2 k^2 - \frac{l(l+1)}{r^2} \right] \psi_r(r) = 0. \quad (3.5)$$

With the substitution

$$\psi_r(r) = \frac{u_l(r)}{r^{1/2}}, \quad (3.6)$$

Equation (3.5) can be transformed into

$$\left[\frac{d^2}{dr^2} + \frac{1}{r} \frac{d}{dr} + n^2 k^2 - \frac{(l+1/2)^2}{r^2} \right] u_r(r) = 0 \quad (3.7)$$

This equation is the Bessel equation with $\nu = l+1/2$. Finally, the solution for $\psi_r(r)$ is given by

$$\begin{cases} \psi_r(r) = A j_l(nkr) & r < a, \\ \psi_r(r) = B h_l^{(2)}(kr) & r > a, \end{cases} \quad (3.8)$$

where j_l is the spherical Bessel function, $h_l^{(2)}$ is the Hankel function of second order, and a is the radius of the microsphere. A , B are constants to be determined from the boundary conditions.

The spherical Bessel functions determine the radial dependence of the optical field. A plot of $j_l(x)$ for small indices is shown in Fig. (3.1) .

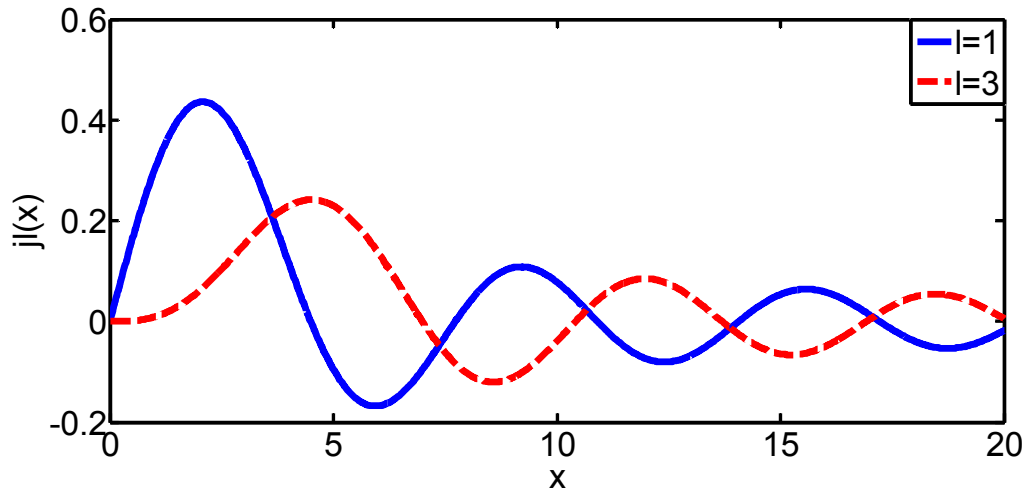


Fig. (3.1) Spherical Bessel function with small indices.

As shown in the figure, the oscillating field of lower order Bessel functions fills almost the entire volume of the sphere. This should not be the case because WGMs are confined close to the surface. Figure (3.2) shows spherical Bessel functions with large l number. As one can see, the Bessel function for large l has a maximum amplitude at approximately $x \approx l$. i.e , $x = nka$.

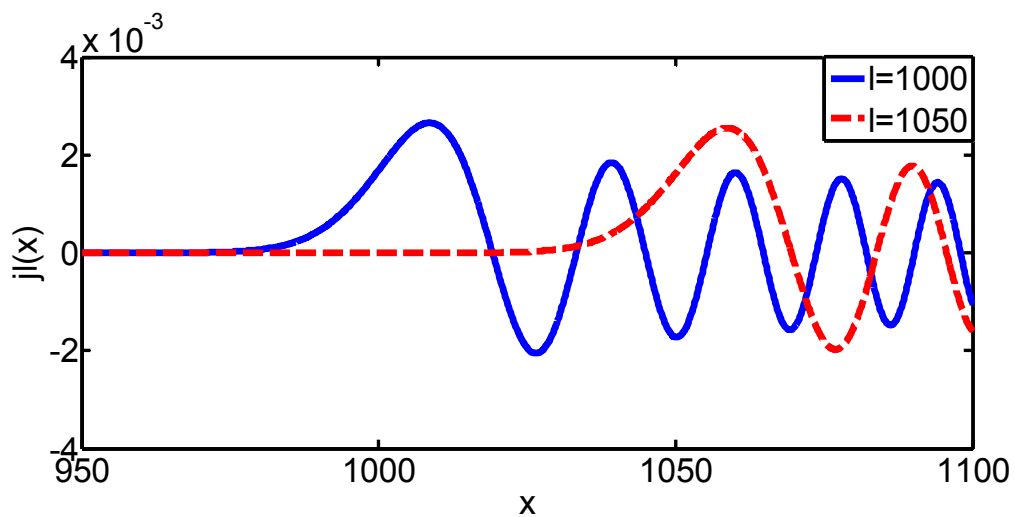


Fig. (3.2) Spherical Bessel function with large indices.

So for WGMs circulating within the microsphere, we should have,

$$l \approx n \frac{2\pi}{\lambda} a, \quad (3.9)$$

or

$$2\pi a \approx \frac{l}{n} \lambda. \quad (3.10)$$

l in this sense represents the number of wavelengths in the circumference and can also be also identified as the angular momentum in the quantum physics [2].

3.1.1.2 Polar Dependence of Fields

The equation of polar dependence can be expressed by

$$\frac{1}{\cos(\theta)} \frac{d}{d\theta} \left(\cos(\theta) \frac{d}{d\theta} \psi_\theta \right) - \frac{m^2}{\cos^2(\theta)} \psi_\theta + l(l+1) \psi_\theta = 0. \quad (3.11)$$

The solution of this differential equation assumes the form

$$\psi_\theta(\theta) \sim P_l^m(\cos\theta), \quad (3.12)$$

where $P_l^m(x)$ are the adjoint Legendre polynomials.

When $l = m$ and large enough, the field is concentrated around the equator plane (Fig. (3.3-a)). If $l \neq m$, the mode has oscillating structure (Fig. (3.3-b) & Fig. (3.3-c)). These oscillations increase when the difference between l and m is large. So it is reasonable that the l and m values of a WGM should be similar [3]. If we assume that the modes confined to the equator plane ($\theta \approx 0$, θ is measured from the equator plane) are the ones most strongly coupled to the fiber, we can make this approximation, $\tan(\theta) \approx \theta$. Equation (3.11) can be written as

$$\frac{d^2}{d\theta^2} \psi_\theta - \theta \frac{d}{d\theta} \psi_\theta - m^2(1 + \theta^2) \psi_\theta + l(l+1) \psi_\theta = 0, \quad (3.13)$$

where $\theta \ll \ll$ This yields

$$\psi_\theta(\theta) \cong N_\theta \exp\left[-\frac{m}{2}\theta^2\right] H_N(\sqrt{m}\theta), \quad (3.14)$$

where $N = l-m$, $H_N(x)$ are the Hermite polynomials, and N_θ is the normalization factor. It is chosen such that the integration of $|\psi_\theta|^2$ over the infinite θ domain gives unity.

Hence

$$N_\theta = \frac{\sqrt{m}}{2^N \sqrt{\pi} N!}. \quad (3.15)$$

3.1.1.3 Azimuthal Dependence of Fields

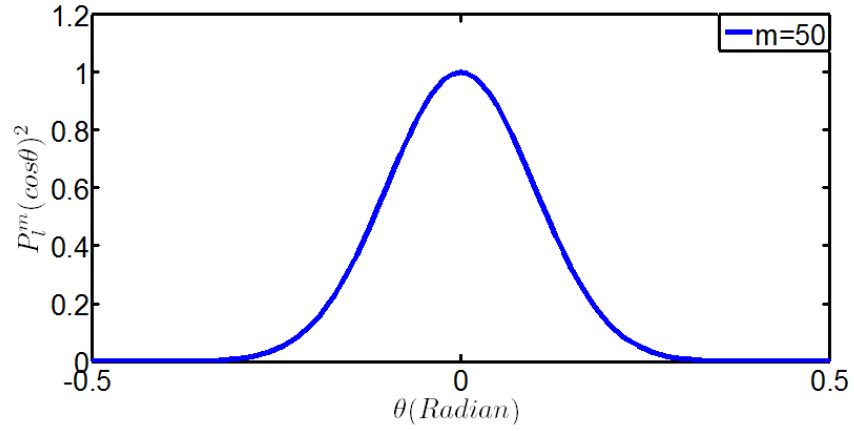
The azimuthal differential equation can be expressed as

$$\frac{1}{\psi_\varphi} \frac{d^2}{d\varphi^2} \psi_\varphi = \text{const} = -m^2. \quad (3.16)$$

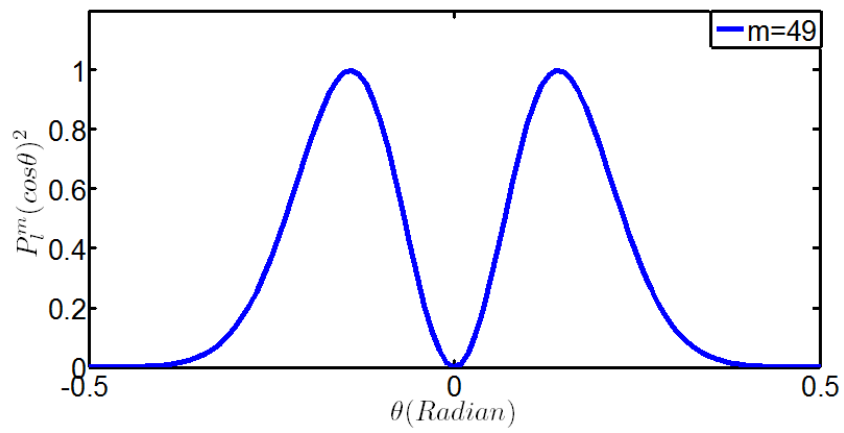
So, the azimuthal solution can be written as

$$\psi_\varphi = N_\varphi \exp(\pm im\varphi), \quad (3.17)$$

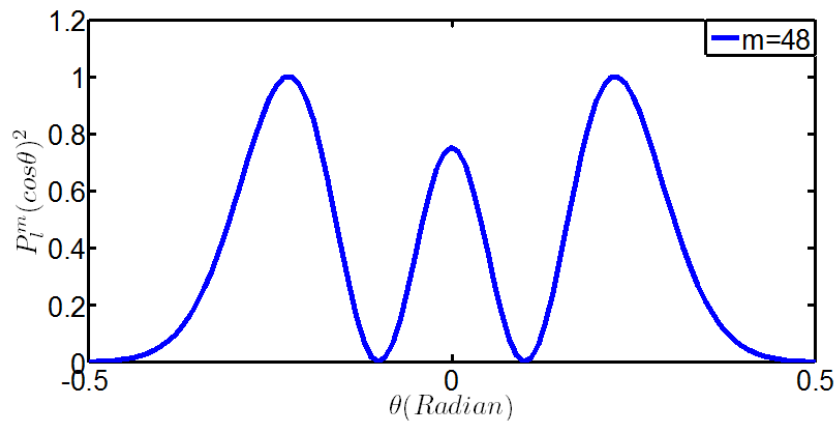
where N_φ is the normalization constant chosen so that the integration of $|\psi_\varphi|^2$ over one revolution is unity. By this definition, $N_\varphi = 1/\sqrt{2\pi}$. $|m| \leq l$. So, we have $2l+1$ degeneracy of the azimuthal modes.



(a)



(b)



(c)

Fig. (3.3) Squared Legendre polynomial representing the angular structure of the modes. The three examples have $l = 50$ and: (a) $m = 50$, (b) $m = 49$, and (c) $m = 48$.

3.1.2 Characteristic Equation

TM and TE modes are specified by the conditions [4]

$$\begin{cases} \mathbf{r} \cdot \mathbf{E}_{lm}^{(TM)} = -Z \frac{l(l+1)}{k} f_l(kr) Y_{lm}(\theta, \varphi), \\ \mathbf{r} \cdot \mathbf{H}_{lm}^{(TM)} = 0, \end{cases} \quad (3.18)$$

$$\begin{cases} \mathbf{r} \cdot \mathbf{H}_{lm}^{(TE)} = \frac{l(l+1)}{k} f_l(kr) Y_{lm}(\theta, \varphi), \\ \mathbf{r} \cdot \mathbf{E}_{lm}^{(TE)} = 0, \end{cases} \quad (3.19)$$

where Z is the medium impedance and

$$f_l(kr) = A j_l(kr) + B h_l^{(2)}(kr). \quad (3.20)$$

$Y_{lm}(\theta, \varphi)$ is a function representing the azimuthal and polar dependence. The normalized solution of these equations can be written as

$$\begin{cases} \mathbf{E}_{lm}^{(TM)} = i \frac{Z}{k} \nabla \times \mathbf{H}_{lm}^{(TM)}, \\ \mathbf{H}_{lm}^{(TM)} = f_l(kr) \mathbf{X}_{lm}(\theta, \varphi), \end{cases} \quad (3.21)$$

$$\begin{cases} \mathbf{E}_{lm}^{(TE)} = Z f_l(kr) \mathbf{X}_{lm}(\theta, \varphi), \\ \mathbf{H}_{lm}^{(TE)} = -\frac{i}{kZ} \nabla \times \mathbf{E}_{lm}^{(TE)}, \end{cases} \quad (3.22)$$

where

$$\mathbf{X}_{lm}(\theta, \varphi) = \frac{1}{\sqrt{l(l+1)}} \mathbf{L} Y_{lm}(\theta, \varphi), \quad (3.23)$$

with $\mathbf{L} = \frac{1}{i} \mathbf{r} \times \nabla$.

One can show that

$$\nabla \times f_l(kr)\mathbf{X}_{lm}(\theta, \varphi) = i \frac{\bar{\mathbf{n}}}{r} \sqrt{l(l+1)} f_l(kr) Y_{lm}(\theta, \varphi) + \frac{1}{r} \frac{\partial}{\partial r} [r f_l(kr)] \bar{\mathbf{n}} \times \mathbf{X}_{lm}(\theta, \varphi), \quad (3.24)$$

where $\bar{\mathbf{n}}$ is a unit vector in radial direction. Then, the normalized fields are

$$\begin{cases} \mathbf{E}_{lm}^{(TM)} = i \frac{Z}{k} \frac{1}{r} \frac{\partial}{\partial r} [r f_l(kr)] \bar{\mathbf{n}} \times \mathbf{X}_{lm}(\theta, \varphi), \\ \mathbf{H}_{lm}^{(TM)} = f_l(kr) \mathbf{X}_{lm}(\theta, \varphi), \end{cases} \quad (3.25)$$

$$\begin{cases} \mathbf{E}_{lm}^{(TE)} = Z f_l(kr) \mathbf{X}_{lm}(\theta, \varphi), \\ \mathbf{H}_{lm}^{(TE)} = -\frac{i}{k} \frac{1}{r} \frac{\partial}{\partial r} [r f_l(kr)] \bar{\mathbf{n}} \times \mathbf{X}_{lm}(\theta, \varphi). \end{cases} \quad (3.26)$$

Now, a silica microsphere coated with a film of nanomaterial is shown in Fig. (3.4).

Consider TM modes, the transverse \mathbf{H} and \mathbf{E} must be continuous at the boundary. So,

$$A_s j_l(k_s a) + B_s h_l^{(2)}(k_s a) = A_f j_l(k_f a) + B_f h_l^{(2)}(k_f a), \quad (3.27)$$

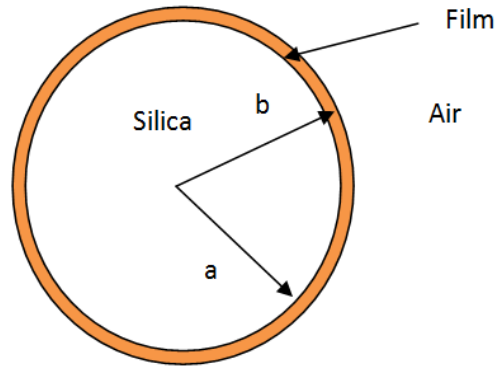


Fig. (3.4) Coated silica microsphere with film surrounded by air.

$$\begin{aligned} \frac{Z_s}{k_s} \left[\frac{\partial}{\partial r} (r j_l(k_s r)) \right]_{r=a} A_s + \frac{\partial}{\partial r} (r h_l^{(2)}(k_s r)) \Big|_{r=a} B_s = \\ \frac{Z_f}{k_f} \left[\frac{\partial}{\partial r} (r j_l(k_f r)) \right]_{r=a} A_f + \frac{\partial}{\partial r} (r h_l^{(2)}(k_f r)) \Big|_{r=a} B_f, \end{aligned} \quad (3.28)$$

$$A_f j_l(k_f b) + B_f h_l^{(2)}(k_f b) = A_o j_l(k_o b) + B_o h_l^{(2)}(k_o b), \quad (3.29)$$

$$\begin{aligned} & \frac{Z_f}{k_f} \left[\frac{\partial}{\partial r} (r j_l(k_f r)) \right]_{r=b} A_f + \frac{\partial}{\partial r} (r h_l^{(2)}(k_f r)) \Big|_{r=b} B_f = \\ & \frac{Z_o}{k_o} \left[\frac{\partial}{\partial r} (r j_l(k_o r)) \right]_{r=b} A_o + \frac{\partial}{\partial r} (r h_l^{(2)}(k_o r)) \Big|_{r=b} B_o \end{aligned} \quad (3.30)$$

where s, f , and o refer to silica, film, air, respectively.

By rearrangement,

$$\begin{aligned} & \left[\begin{array}{c} j_l(k_s a) \\ \frac{Z_s}{k_s} \frac{\partial}{\partial r} (r j_l(k_s r)) \Big|_{r=a} \end{array} \right]_{r=a} \begin{array}{c} h_l^{(2)}(k_s a) \\ \frac{Z_s}{k_s} \frac{\partial}{\partial r} (r h_l^{(2)}(k_s r)) \Big|_{r=a} \end{array} \left[\begin{array}{c} A_s \\ B_s \end{array} \right] = \\ & \left[\begin{array}{c} j_l(k_f a) \\ \frac{Z_f}{k_f} \frac{\partial}{\partial r} (r j_l(k_f r)) \Big|_{r=a} \end{array} \right]_{r=a} \begin{array}{c} h_l^{(2)}(k_f a) \\ \frac{Z_f}{k_f} \frac{\partial}{\partial r} (r h_l^{(2)}(k_f r)) \Big|_{r=a} \end{array} \left[\begin{array}{c} A_f \\ B_f \end{array} \right], \end{aligned} \quad (3.31)$$

$$\begin{aligned} & \left[\begin{array}{c} j_l(k_f b) \\ \frac{Z_f}{k_f} \frac{\partial}{\partial r} (r j_l(k_f r)) \Big|_{r=b} \end{array} \right]_{r=b} \begin{array}{c} h_l^{(2)}(k_f b) \\ \frac{Z_f}{k_f} \frac{\partial}{\partial r} (r h_l^{(2)}(k_f r)) \Big|_{r=b} \end{array} \left[\begin{array}{c} A_f \\ B_f \end{array} \right] = \\ & \left[\begin{array}{c} j_l(k_o b) \\ \frac{Z_o}{k_o} \frac{\partial}{\partial r} (r j_l(k_o r)) \Big|_{r=b} \end{array} \right]_{r=b} \begin{array}{c} h_l^{(2)}(k_o b) \\ \frac{Z_o}{k_o} \frac{\partial}{\partial r} (r h_l^{(2)}(k_o r)) \Big|_{r=b} \end{array} \left[\begin{array}{c} A_o \\ B_o \end{array} \right]. \end{aligned} \quad (3.32)$$

We can define

$$D_i(k_i, a) = \left[\begin{array}{c} j_l(k_i a) \\ \frac{Z_i}{k_i} \frac{\partial}{\partial r} (r j_l(k_i r)) \Big|_{r=a} \end{array} \right]_{r=a} \begin{array}{c} h_l^{(2)}(k_i a) \\ \frac{Z_i}{k_i} \frac{\partial}{\partial r} (r h_l^{(2)}(k_i r)) \Big|_{r=a} \end{array}, \quad (3.33)$$

So,

$$D_s(k_s, a) \begin{bmatrix} A_s \\ B_s \end{bmatrix} = D_f(k_f, a) \begin{bmatrix} A_f \\ B_f \end{bmatrix}, \quad (3.34)$$

$$D_f(k_f, b) \begin{bmatrix} A_f \\ B_f \end{bmatrix} = D_o(k_o, b) \begin{bmatrix} A_o \\ B_o \end{bmatrix}. \quad (3.35)$$

Now,

$$\begin{bmatrix} A_s \\ B_s \end{bmatrix} = D_s^{-1}(k_s, a) D_f(k_f, a) D_f^{-1}(k_f, b) D_o(k_o, b) \begin{bmatrix} A_o \\ B_o \end{bmatrix}. \quad (3.36)$$

Consider

$$D_s^{-1}(k_s, a) D_f(k_f, a) = \frac{1}{|D_s(k_s, a)|} \begin{bmatrix} a_1 & a_2 \\ a_3 & a_4 \end{bmatrix}, \quad (3.37)$$

$$D_f^{-1}(k_f, b) D_o(k_o, b) = \frac{1}{|D_f(k_f, a)|} \begin{bmatrix} b_1 & b_2 \\ b_3 & b_4 \end{bmatrix}. \quad (3.38)$$

By some derivations, we find

$$a_1 = \frac{Z_s}{k_s} \frac{\partial}{\partial r} (r h_l^{(2)}(k_s r)) \Big|_{r=a} j_l(k_f a) - h_l^{(2)}(k_s a) \frac{Z_f}{k_f} \frac{\partial}{\partial r} (r j_l(k_f r)) \Big|_{r=a}, \quad (3.39)$$

$$a_2 = \frac{Z_s}{k_s} \frac{\partial}{\partial r} (r h_l^{(2)}(k_s r)) \Big|_{r=a} h_l^{(2)}(k_f a) - h_l^{(2)}(k_s a) \frac{Z_f}{k_f} \frac{\partial}{\partial r} (r h_l^{(2)}(k_f r)) \Big|_{r=a}, \quad (3.40)$$

$$a_3 = -\frac{Z_s}{k_s} \frac{\partial}{\partial r} (r j_l(k_s r)) \Big|_{r=a} j_l(k_f a) + j_l(k_s a) \frac{Z_f}{k_f} \frac{\partial}{\partial r} (r j_l(k_f r)) \Big|_{r=a}, \quad (3.41)$$

$$a_4 = -\frac{Z_s}{k_s} \left[\frac{\partial}{\partial r} (r j_l(k_s r)) \Big|_{r=a} h_l^{(2)}(k_f a) + j_l(k_s a) \frac{Z_f}{k_f} \frac{\partial}{\partial r} (r h_l^{(2)}(k_f r)) \Big|_{r=a} \right], \quad (3.42)$$

$$b_1 = \frac{Z_f}{k_f} \frac{\partial}{\partial r} (r h_l^{(2)}(k_f r)) \Big|_{r=b} j_l(k_o b) - h_l^{(2)}(k_f b) \frac{Z_o}{k_o} \frac{\partial}{\partial r} (r j_l(k_o r)) \Big|_{r=b}, \quad (3.43)$$

$$b_2 = \frac{z_f}{k_f} \frac{\partial}{\partial r} (r h_l^{(2)}(k_f r)) \Big|_{r=b} h_l^{(2)}(k_o b) - h_l^{(2)}(k_f b) \frac{z_o}{k_o} \frac{\partial}{\partial r} (r h_l^{(2)}(k_o r)) \Big|_{r=b}, \quad (3.44)$$

$$b_3 = -\frac{z_f}{k_f} \frac{\partial}{\partial r} (r j_l(k_f r)) \Big|_{r=b} j_l(k_o b) + j_l(k_f b) \frac{z_o}{k_o} \frac{\partial}{\partial r} (r j_l(k_o r)) \Big|_{r=b}, \quad (3.45)$$

$$b_4 = -\frac{z_f}{k_f} \frac{\partial}{\partial r} (r j_l(k_f r)) \Big|_{r=b} h_l^{(2)}(k_o b) + j_l(k_f b) \frac{z_o}{k_o} \frac{\partial}{\partial r} (r h_l^{(2)}(k_o r)) \Big|_{r=b}. \quad (3.46)$$

Now, substitute in Eq. (3.36)

$$\begin{bmatrix} A_s \\ B_s \end{bmatrix} = \frac{1}{|D_s(k_s, a)| |D_f(k_f, a)|} \begin{bmatrix} a_1 & a_2 \\ a_3 & a_4 \end{bmatrix} \begin{bmatrix} b_1 & b_2 \\ b_3 & b_4 \end{bmatrix} \begin{bmatrix} A_o \\ B_o \end{bmatrix}. \quad (3.47)$$

For the innermost layer (silica), $B_s = 0$ because we must have a finite field at the origin. Also, for outer most layer (air), $A_o = 0$ because there is no incoming wave.

Therefore,

$$\begin{bmatrix} A_s \\ 0 \end{bmatrix} = \frac{1}{|D_s(k_s, a)| |D_f(k_f, a)|} \begin{bmatrix} (a_1 b_2 + a_2 b_4) B_o \\ (a_3 b_2 + a_4 b_4) B_o \end{bmatrix}. \quad (3.48)$$

We notice, then, that the characteristic equation should be

$$a_3 b_2 + a_4 b_4 = 0. \quad (3.49)$$

For simplicity, we define $\psi_l(z) = z j_l(z)$, and $\chi_l(z) = z h_l^{(2)}(z)$, where $\psi_l(z)$ and $\chi_l(z)$ are spherical Ricatti-Bessel function and Ricatti-Neumann function, respectively. The characteristic equation can be expressed by [5]

$$N_o \frac{\chi'_l(k_o n_o b)}{\chi_l(k_o n_o b)} = \frac{B_l \psi'_l(k_o n_f b) + \chi'_l(k_o n_f b)}{B_l \psi_l(k_o n_f b) + \chi_l(k_o n_f b)},$$

$$N_o = \begin{cases} \frac{n_o}{n_f} & \text{TE modes,} \\ \frac{n_f}{n_o} & \text{TM modes.} \end{cases} \quad (3.50)$$

Here, k_o is the resonance wavevector in air; n_s , n_f , and n_o are the refractive indices of the microsphere, film, and air, respectively; B_l is a coefficient and its expression is given by

$$B_l = \frac{N_1 \psi'_l(k_o n_s a) \chi_l(k_o n_f a) - \psi_l(k_o n_s a) \chi'_l(k_o n_f a)}{\psi_l(k_o n_s a) \psi'_l(k_o n_f a) - N_1 \psi'_l(k_o n_s a) \psi_l(k_o n_f a)},$$

$$N_1 = \begin{cases} \frac{n_s}{n_f} & \text{TE modes,} \\ \frac{n_f}{n_s} & \text{TM modes.} \end{cases} \quad (3.51)$$

The fraction of light energy in the silica microsphere, film, and air can be calculated from [5]

$$\begin{cases} \eta_i = \frac{n_i^2 I_i}{n_s^2 I_s + n_f^2 I_f + n_o^2 I_o} \text{ (TE modes),} \\ \eta_i = \frac{I_i}{I_s + I_f + I_o} \text{ (TM modes), } i = s, f, \text{ and } o, \end{cases} \quad (3.52)$$

where

$$I_s = \int_0^a [A_l \psi_l(k_o n_s r)]^2 dr,$$

$$I_p = \int_a^b [B_l \psi_l(k_o n_f r) + \chi_l(k_o n_f r)]^2 dr,$$

$$I_o = \int_b^\infty [C_l \chi_l(k_o n_o r)]^2 dr. \quad (3.53)$$

A_l and C_l are coefficients determined by

$$A_l = \frac{B_l \psi_l(k_o n_f a) + \chi_l(k_o n_f a)}{\psi_l(k_o n_s a)},$$

$$C_l = \frac{B_l \psi_l(k_o n_f b) + \chi_l(k_o n_f b)}{\chi_l(k_o n_o b)}. \quad (3.54)$$

For the uncoated microsphere, the same steps can be taken but the case now is much simpler. We can get the characteristic equation for the uncoated case from the expression

$$N \frac{\psi_l'(k_o n_s a)}{\psi_l(k_o n_s a)} = \frac{\chi_l'(k_o n_o a)}{\chi_l(k_o n_o a)},$$

$$N = \begin{cases} n_s & \text{TE modes,} \\ \frac{1}{n_s} & \text{TM modes.} \end{cases} \quad (3.55)$$

3.2 Q Factor

3.2.1 Q Factor of Coated Microsphere with Film of Nanomaterial

The loss of WGM in a functional microsphere can come from several sources including material absorption in silica, absorption in the ISAM film, scattering due to surface roughness, and taper-microsphere coupling [2, 6]. Their contribution for cavity Q factors can be respectively represented by Q_{silica} , Q_{film} , Q_{ss} , and $Q_{coupling}$. Given the large microsphere sizes ($\sim 250 \mu\text{m}$), we can safely ignore the contribution due to radiation losses, which are exceedingly small when the diameter to wavelength ratio is greater than $15 \mu\text{m}$ [2]. In this case, we can represent the total cavity Q factor as

$$\frac{1}{Q} \approx \frac{1}{Q_{silica}} + \frac{1}{Q_{film}} + \frac{1}{Q_{ss}} + \frac{1}{Q_{coupling}}, \quad (3.56)$$

where $\frac{1}{Q_{silica}}$ is the material absorption loss in silica and $\frac{1}{Q_{film}}$ is the material absorption loss in film. These can be determined as

$$\begin{cases} Q_{silica} = \frac{2\pi n_s}{\lambda_R \alpha_s \eta_s}, \\ Q_{film} = \frac{2\pi n_f}{\lambda_R \alpha_f \eta_f}, \end{cases} \quad (3.57)$$

where λ_R is the resonance wavelength, and α_s , and α_f are the optical attenuation coefficients of silica and film, respectively.

The Q factor due to scattering (Q_{ss}) is given by [7]

$$Q_{ss} = \frac{3\varepsilon(\varepsilon+2)^2(\lambda_R)^{7/2}D^{1/2}}{4\pi^3(\varepsilon-1)^{5/2}\sigma^2B^2}, \quad (3.58)$$

where ε is the permittivity of the medium, D is the diameter of the microsphere, σ is the r.m.s of surface roughness, and B is the correlation length. Q_{ss} can reach the value 10^{10} when the diameter is greater than 100 μm .

The possible solutions for resonance wavelength for uncoated microsphere with radius, $a = 125\mu\text{m}$ and wavelength around 1550 nm (1550-1552 nm). For TM modes, the possible solutions are shown in Fig. (3.5). The solutions at $l = 715, 702,$ and $692,$ respectively and the corresponding wavelengths are 1550.8145, 1551.9265, 1551.4975 nm, respectively.

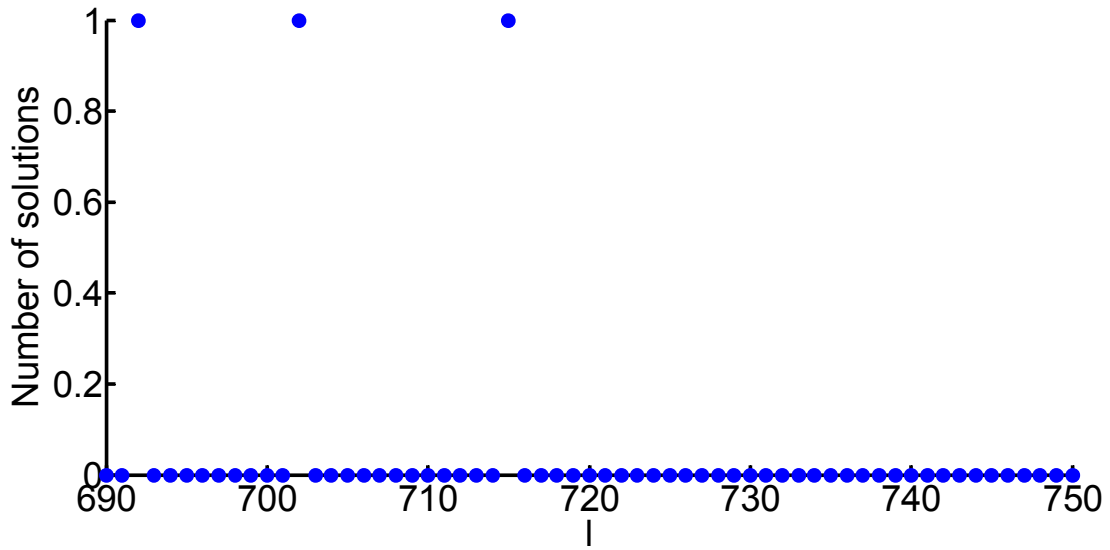


Fig. (3.5) Possible solutions for TM modes.

For TE modes, the possible solutions are shown in Fig. (3.6). The solutions at $l = 716$, 703, and 693, respectively and the corresponding wavelengths are 1550.6145, 1551.6395, 1551.1425 nm, respectively.

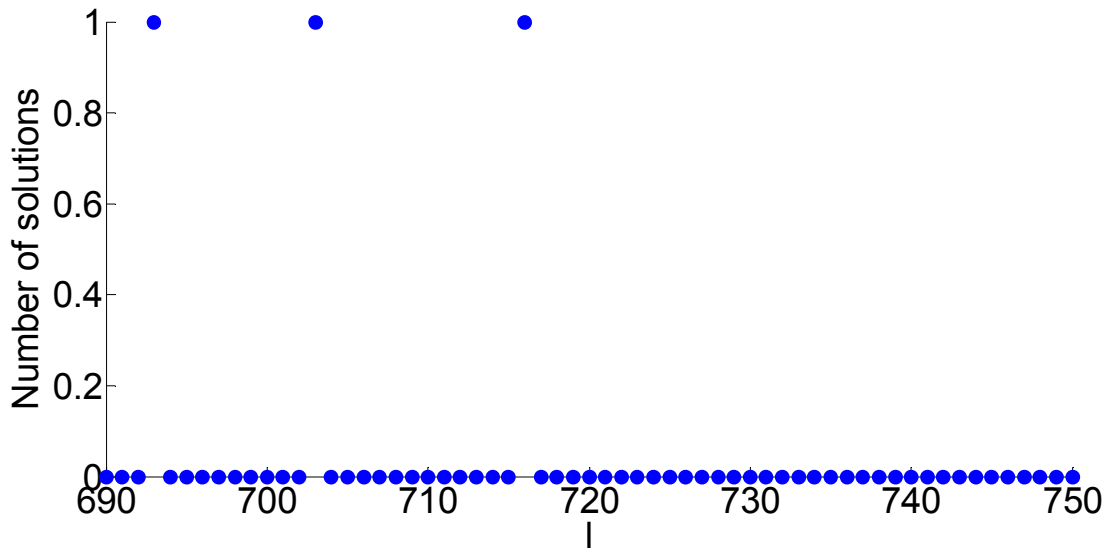


Fig. (3.6) Possible solutions for TE modes.

The radial field distribution is shown for TM modes in Fig. (3.7-a). The first three modes with $n = 1, 2, 3$ are depicted. For TM modes, $n = 1, l = 715$, and wavelength is 1550.8145 nm, $n = 2, l = 702$, and wavelength is 1551.9265 nm, $n = 3, l = 692$, and wavelength is 1551.4975 nm. In Fig. (3.7-b), comparison between the field distribution of the fundamentals modes of TM and TE modes is also shown.

In the following discussion, we consider what would happen if we coat the microsphere surface with a thin layer of polymers. Our analysis is based on perturbative analysis commonly used in quantum physics.

3.2.1.1 Wavelength Relative Shift

From quantum perspective, resonant modes contain photons with quantized angular momentum. This can be similar to electron on Bohr atom [8]. In case of absence of excess charge, the Helmholtz equation is

$$\nabla^2 \mathbf{E} + k^2 n^2 \mathbf{E} = 0. \quad (3.59)$$

Using the definition of angular momentum operator

$$\begin{aligned} \hat{L} &= -i(\vec{r} \times \nabla), \\ \nabla^2 &= \left(\frac{1}{r} \frac{\partial^2(r)}{\partial r^2} - \frac{\hat{L}^2}{r^2} \right). \end{aligned} \quad (3.60)$$

Now Eq. (3.59) becomes

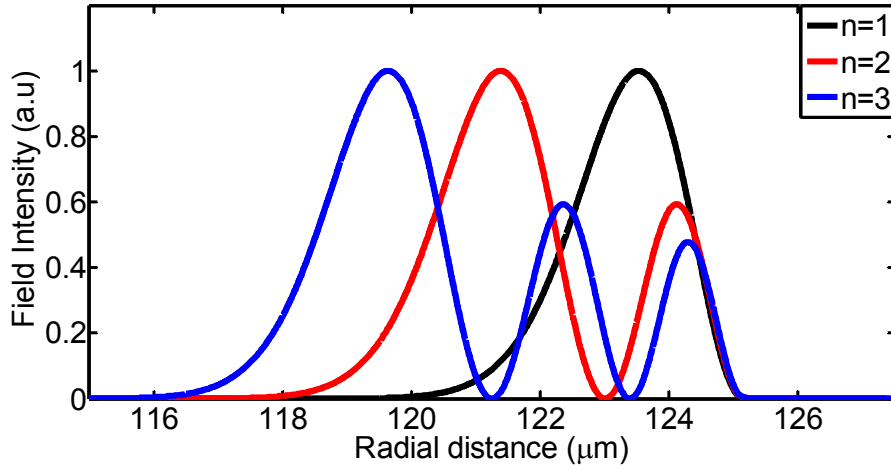
$$\left(\frac{1}{r} \frac{\partial^2(r)}{\partial r^2} - \frac{\hat{L}^2}{r^2} \right) \mathbf{E} + k^2 n^2 \mathbf{E} = 0. \quad (3.61)$$

Consider that the momentum operator commutes with its square, $[\hat{L}^2, \hat{L}] = 0$. For TE modes, \mathbf{E} can be written as $\hat{L} \psi$ and Eq. (3.61) would be

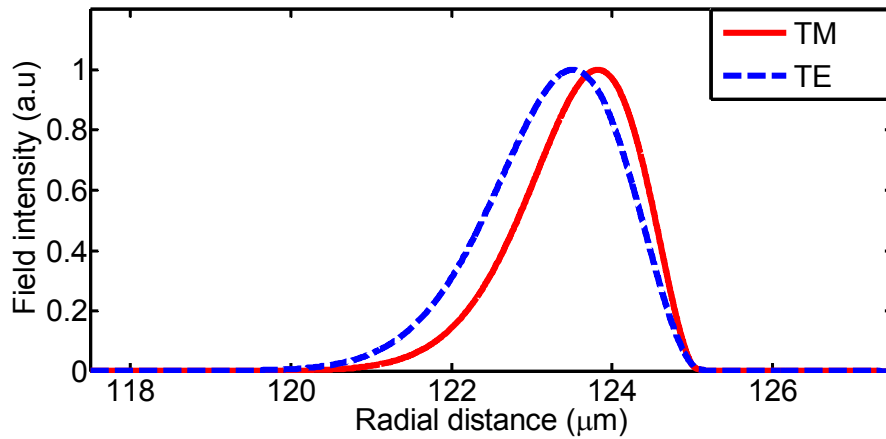
$$\hat{L} \left[\frac{\partial^2(r\psi)}{\partial r^2} - \frac{\hat{L}^2(r\psi)}{r^2} + k^2(r\psi) \right] = 0, \quad (3.62)$$

Vector Helmholtz equation is satisfied if the scalar quantity between the brackets equals zero. Then,

$$\left[\frac{\partial^2(r\psi)}{\partial r^2} - \frac{\hat{L}^2(r\psi)}{r^2} + k^2(r\psi) \right] = 0. \quad (3.63)$$



(a)



(b)

Fig. (3.7) The radial field distribution: (a) first three modes of TM modes, and (b) fundamental modes of TM and TE modes.

Define,

$$\begin{aligned} r\psi(r) &= \psi_r(r)\mathbf{Y}_{lm}, \\ \hat{L}^2\mathbf{Y}_{lm} &= l(l+1)\mathbf{Y}_{lm}. \end{aligned} \quad (3.64)$$

By rewriting Eq. (3.62)

$$\frac{d^2\psi_r(r)}{dr^2} + \left\{ k_o^2 - \left[k_o^2(1-n^2) + \frac{l(l+1)}{r^2} \right] \right\} \psi_r(r) = 0, \quad (3.65)$$

This equation is *Schrödinger* –like equation. The effective energy is K_o^2 and the effective potential is

$$V_{eff}(r; k_o, n, l) = k_o^2(1-n^2) + \frac{l(l+1)}{r^2}. \quad (3.66)$$

By adding a layer to microsphere surface, a perturbation in the potential occurs and can be expressed by

$$\delta V_{eff} = \delta[k_o^2(1-n^2)], \quad (3.67)$$

The first order perturbation in the energy of a quantum level is

$$\delta E_{eff} = \frac{\langle \psi_r | \delta V_{eff} | \psi_r \rangle}{\langle \psi_r | \psi_r \rangle}, \quad (3.68)$$

This equation can be written as

$$\delta(k_o^2) = \frac{\langle \psi_r | \delta[k_o^2(1-n^2)] | \psi_r \rangle}{\langle \psi_r | \psi_r \rangle}, \quad (3.69)$$

By rearranging

$$\delta(k_o^2)\langle \psi_r | \psi_r \rangle = \delta(k_o^2)\langle \psi_r | \psi_r \rangle + \langle \psi_r | -k_o^2(n_f^2 - n_o^2) | \psi_r \rangle + \langle \psi_r | -2k_o\delta k_o n_s^2 | \psi_r \rangle,$$

(3.70)

where $\delta(n^2) = (n_f^2 - n_o^2)$.

After some simplifications,

$$\langle \psi_r | -k_o^2(n_f^2 - n_o^2) | \psi_r \rangle + \langle \psi_r | -2k_o \delta k_o n_s^2 | \psi_r \rangle = 0, \quad (3.71)$$

By writing Eq. (3.71) in the integral form, we get

$$\int_a^b -k_o^2(n_f^2 - n_o^2) |\psi_r|^2 dV + \int_0^\infty -2k_o \delta k_o n_s^2 |\psi_r|^2 dV = 0. \quad (3.72)$$

The first term in Eq. (3.72) can be evaluated by

$$\int_a^b -k_o^2(n_f^2 - n_o^2) |\psi_r|^2 dV \cong -k_o^2(n_f^2 - n_o^2) |\psi_r(a)|^2 4\pi a^2 t. \quad (3.73)$$

For the second term, most of the energy is inside the microsphere. So,

$$\int_0^\infty -2k_o \delta k_o n_s^2 |\psi_r|^2 dV \cong \int_0^a -2k_o \delta k_o n_s^2 |\psi_r|^2 dV. \quad (3.74)$$

In the range in which the wavelength is much smaller than the microsphere radius, the integral can be

$$\int_0^a r^2 |\psi_r(r)|^2 dr \approx a^3 (1 - n_o^2 n_s^{-2}) |\psi_r(a)|^2 / 2, \quad (3.75)$$

Finally, from Eq. (3.73) and Eq. (3.75), the fractional shift in wavelength for TE modes is

$$\frac{\delta \lambda}{\lambda} = -\frac{\delta k_o}{k_o} = \frac{(n_f^2 - n_o^2) t}{(n_s^2 - n_o^2) a}. \quad (3.76)$$

In general, the fractional shift in wavelength can be written as

$$\frac{\delta \lambda}{\lambda} = \frac{\int_a^b \delta \varepsilon_r |\vec{E}_{WGM}(r, \theta, \varphi)|^2 dV}{2 \int_0^\infty \varepsilon_r |\vec{E}_{WGM}(r, \theta, \varphi)|^2 dV}, \quad (3.77)$$

For TM modes, the electric field can be expressed as [9]

$$\vec{\mathbf{E}}_{WGM}(r, \theta, \varphi) = \frac{\exp(im\varphi)}{k_o^2 n^2(r)} \left[\frac{1}{r} S'(r) \mathbf{Y}_{lm}(\theta) + \frac{1}{r^2} S(r) \mathbf{Z}_{lm}(\theta) \right], \quad (3.78)$$

The angular function $\mathbf{Y}_{lm}(\theta)$ and $\mathbf{Z}_{lm}(\theta)$ are given, respectively by

$$\begin{aligned} \mathbf{Y}_{lm}(\theta) &= \hat{\mathbf{e}}_r \times \mathbf{X}_{lm}(\theta), \\ \mathbf{Z}_{lm}(\theta) &= l(l+1) P_l^m(\cos \theta) \hat{\mathbf{e}}_r. \end{aligned} \quad (3.79)$$

where $\overline{X}_{lm}(\theta, \phi)$ is the angular vector function of WGM, and $S(r)$ is the radial field which can be expressed as

$$S(r) = \begin{cases} \psi_l(n_1 k_o r), & r < a, \\ B_l \chi_l(n_2 k_o r), & r > a. \end{cases} \quad (3.80)$$

B_l can be easily determined from the continuity at the interface and given by

$$B_l = \frac{\psi_l(n_1 k_o a)}{\chi_l(n_2 k_o a)}, \quad (3.81)$$

and

$$\mathbf{X}_{lm}(\theta) = \frac{im}{\sin \theta} P_l^m(\cos \theta) \hat{\mathbf{e}}_\theta - \frac{\partial}{\partial \theta} P_l^m(\cos \theta) \hat{\mathbf{e}}_\varphi, \quad (3.82)$$

where $\hat{\mathbf{e}}_\theta$ and $\hat{\mathbf{e}}_\varphi$ are unit vectors on the related directions.

Define,

$$W_{lm} = \iint |\mathbf{X}_{lm}(\theta)|^2 \sin \theta d\theta d\varphi, \quad (3.83)$$

Then,

$$\begin{aligned}
\int_0^a \varepsilon_r |\vec{E}_{WGM}(r, \theta, \varphi)|^2 dV &= \frac{W_{lm}}{k_o^4} \int_0^\infty \frac{1}{n^4(r)} \left\{ [S'(r)]^2 + \frac{l(l+1)}{r^2} [S(r)]^2 \right\} dr \\
&= \frac{W_{lm}}{k_o^4} \left(\frac{n_s^2}{n_o^2} - 1 \right) [S(a)]^2 \left\{ \left[\frac{\chi_l'(k_o n_o a)}{\chi_l(k_o n_o a)} \right]^2 + \frac{l(l+1)}{(k_o n_s a)^2} \right\},
\end{aligned} \tag{3.84}$$

and

$$\int_a^b \delta \varepsilon_r |\vec{E}_{WGM}(r, \theta, \varphi)|^2 dV = -\frac{W_{lm}}{k_o^2} [S(a)]^2 \left\{ n_f^2 \left[\frac{\chi_l'(k_o n_o a)}{\chi_l(k_o n_o a)} \right]^2 + \frac{l(l+1)}{(k_o a)^2} \right\} (n_o^{-2} - n_f^{-2}) t, \tag{3.85}$$

Now, the fractional shift in wavelength for TM modes can be expressed as

$$\frac{\delta \lambda}{\lambda} = R_l \frac{(n_f^2 - n_o^2) t}{(n_s^2 - n_o^2) a} \tag{3.86}$$

For large l , R_l is

$$R_l \approx 1 + \frac{n_f^{-2} - n_s^{-2}}{n_o^{-2} - (k_o a/l)^2 + n_s^{-2}}, \tag{3.87}$$

and then,

$$\left(\frac{\Delta \lambda}{\lambda} \right)_{TM} = \frac{n_f^2 - n_o^2}{n_s^2 - n_o^2} \frac{t}{a} R_l = \left(\frac{\Delta \lambda}{\lambda} \right)_{TE} R_l. \tag{3.88}$$

3.2.1.2 Q Factor of added Film

Using $a = 125 \text{ } \mu\text{m}$, $n_o = 1$ (air as surrounding medium), resonance wavelength equals 1550 nm and $n_s = 1.44$ for silica. For the fundamental modes, use $l = 715$ for $n = 1$, use $l = 702$ for $n = 2$, use $l = 692$ for $n = 3$. Using the corresponding wavelengths, then the TM-to-TE ratio, R_l is shown in Fig. (3.8) as a function of the film refractive index, n_f .

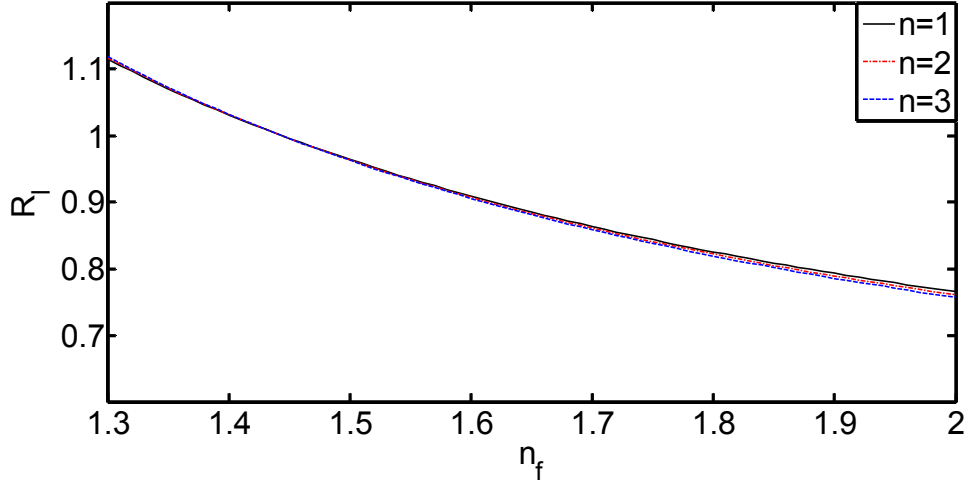


Fig. (3.8) TM-to-TE ratio plotted as a function of refractive index of added film.

Consider a nonmaterial with refractive index, $n_f = 1.8$, optical attenuation coefficients, $\alpha_f = 4.5$ dB/mm. Use $a = 125$ μm , film thickness, $t = 1.3$ nm for one bilayer. Consider 20 bilayers of this film. Figure (3.9) illustrates the percentage of power on the added film. The quality factor due to material absorption of added film is shown in Fig. (3.10).

It is obvious that the percentage of power in the film for fundamental TE modes is higher than that of the fundamental TM modes. The reason is related to field distribution of TE and TM modes on the added region. For low number of film layers, the power percentage is almost linearly proportional with film thickness. Back to the quality factor due to the added film (Eq. (3.57)), we can plot it as a function of the film thickness. The quality factor should be inversely proportional to the power percentage on the film. In this sense, it should be inversely proportional to the film thickness.

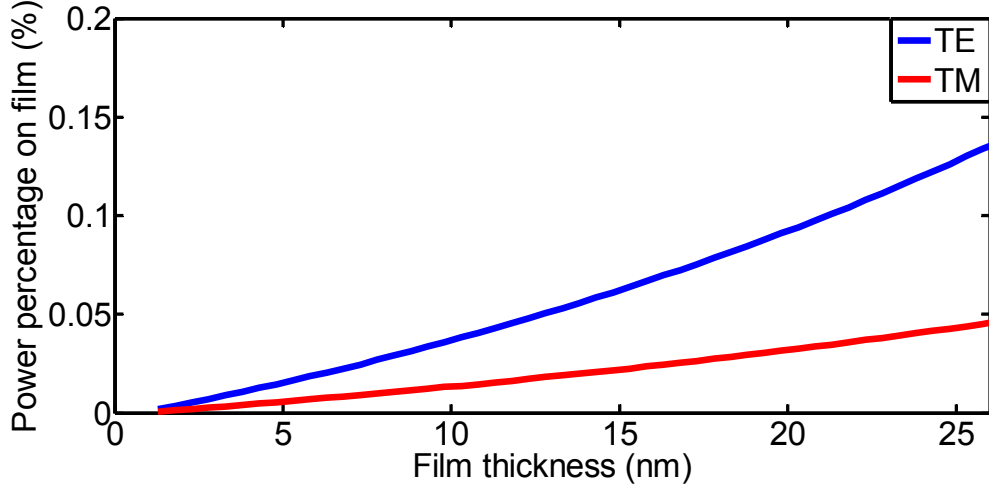


Fig. (3.9) Percentage of power in the added film for the fundamental modes of TM and TE modes.

3.2.2 Q Factor of Coated Microsphere with Au NPs

First of all, we consider the portion of the Q factor of a NP-coated microsphere that is induced by the absorption and scattering of the Au NPs. The cavity Q factor associated with Au NPs is given by

$$Q_{NP} = \omega \frac{W}{P_{NPs}}, \quad (3.89)$$

where ω is the angular frequency, P_{NPs} represents power loss induced by NPs scattering and absorption, and W is the modal energy of WGM which can be written as [10]

$$W = \frac{1}{2} \iiint \varepsilon_o \varepsilon_r |\vec{E}_{WGM}(r, \theta, \varphi)|^2 dV, \quad (3.90)$$

where ε_o is the air permittivity, and ε_r is the relative permittivity of silica.

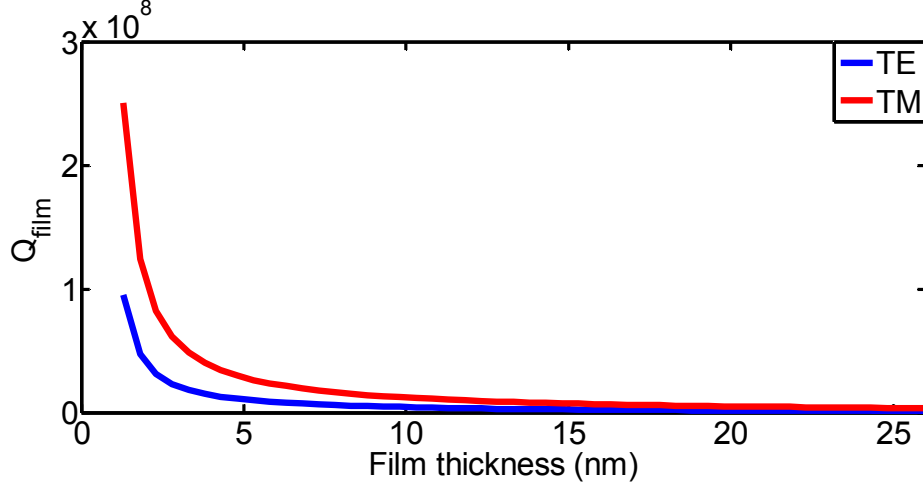


Fig. (3.10) Q factor due the absorption on the added film.

For TE modes, the electric field can be expresses as [9]

$$\vec{E}_{WGM}(r, \theta, \varphi) = \frac{\exp(im\varphi)}{k_0 r} S(r) \mathbf{X}_{lm}(\theta). \quad (3.91)$$

Assuming homogenous medium with constant ϵ_r , the modal energy becomes

$$W = \frac{1}{2k_0^2} \epsilon_o \epsilon_r \iiint |S(r)|^2 |\mathbf{X}_{lm}(\theta)|^2 \sin\theta d\theta d\varphi dr. \quad (3.92)$$

The power loss caused by a single nanoparticle, p_{NP} can be expressed by

$$p_{NP} = \frac{|\vec{E}_{WGM}(a_i, \theta_i, \phi_i)|^2}{2\eta_o} \sigma_{ex}, \quad (3.93)$$

where η_o is the free space impedance, $\vec{E}_{WGM}(a_i, \theta_i, \phi_i)$ is the electric field at the location of the i th NP located on the surface, and σ_{ex} is the total extinction cross section area of the gold nanoparticle (includes both scattering and absorption). Assuming NPs are randomly distributed over microsphere surface with uniform probability, the total

scattered and absorbed power from all particles on the surface, P_{NPs} can then be expressed by

$$P_{NPs} = \frac{N_p}{2\eta_0} \sigma_{ex.} \iint |\vec{E}_{WGM}(a, \theta, \varphi)|^2 dA, \quad (3.94)$$

where is N_p the Au NPs density on the surface of microsphere. The integration is done over the surface area A of the microsphere. So, the quality factor can be rewritten as

$$Q_{NPs} = \omega \frac{\varepsilon_0 \varepsilon_r \eta_0 \iiint |S(r)|^2 |\mathbf{X}_{lm}(\theta)|^2 \sin\theta d\theta d\varphi dr}{N_p \sigma_{ex.} \iint |S(a)|^2 |\mathbf{X}_{lm}(\theta)|^2 \sin\theta d\theta d\varphi}. \quad (3.95)$$

This can be simplified to

$$Q_{NPs} = \omega \frac{\varepsilon_0 \varepsilon_r \eta_0 \left[\int_0^\infty |S(r)|^2 dr \right]}{N_p \sigma_{ex.} |S(a)|^2}. \quad (3.96)$$

More simplification can be done . The integral $\int_0^\infty |S(r)|^2 dr$ can be approximated as $\int_0^a |S(r)|^2 dr$. This approximation is acceptable as most of the field intensity is concentrated inside the microsphere. Furthermore, $\int_0^a |S(r)|^2 dr$ is $\sim a(1 - n_0^2 n_s^{-2}) |S(a)|^2 / 2$ [10, 11].

Now,

$$Q_{NPs} = \omega \frac{\varepsilon_0 \eta_0 a (n_s^2 - n_0^2)}{2 N_p \sigma_{ex.}}. \quad (3.97)$$

In the case of small Au NP which is our case, the total (extinction) cross section can be given by [12]

$$\sigma_{ex.} = 4\pi a^2 \left\{ \frac{m^2 - 1}{m^2 + 2} \left[1 + \frac{x^2}{15} \left(\frac{m^2 - 1}{m^2 + 2} \right) \frac{m^4 + 27m^2 + 38}{2m^2 + 3} \right] \right\} + \frac{8}{3} x^4 \text{Re} \left\{ \left(\frac{m^2 - 1}{m^2 + 2} \right)^2 \right\}, \quad (3.98)$$

where m is the ratio of refractive index of the Au NPs and air, and $x = 2\pi a / \lambda$.

In this case, the total Q factor can be expressed as

$$\frac{1}{Q} \approx \frac{1}{Q_{silica}} + \frac{1}{Q_{NPs}} + \frac{1}{Q_{coupling}}, \quad (3.99)$$

Using the same procedure for the thin film layer, we can get a formula for the Q factor in case of TM modes which given by

$$(Q_{NPs})_{TE} = (Q_{NPs})_{TM} \times R'_l, \quad (3.100)$$

where

$$R'_l = 1 + \frac{n_o^{-2} - n_s^{-2}}{n_o^{-2} - (k_o a / l)^2 + n_s^{-2}}, \quad (3.101)$$

where n_f was replaced by n_o .

References

- [1] Tobias Jan August Kippenberg, Nonlinear Optics in Ultra-high-Q Whispering Gallery Optical Microcavities. California Institute of Technology, 2004.
- [2] Alessandro Chiasera, *et al.*, Spherical whispering-gallery-mode microresonators, *Laser Photon. Rev.* **4**, 457-482 (2010).
- [3] A. N. Oraevsky, Whispering-gallery waves, *Quantum Electron.* **32**, 377-400 (2002).
- [4] J. D. Jackson, *Classical electrodynamics*, John Wiley & Sons, Inc., 1998.
- [5] Nai Lin, *et al.*, Simulation and optimization of polymer-coated microsphere resonators in chemical vapor sensing, *J. Appl. Opt.* **50**, 5465-5472 (2011).
- [6] M. L. Gorodetsky, A. A. Savchenkov, and V. S. Ilchenko, Ultimate Q of optical microsphere resonators, *Opt. Lett.* **21**, 453-455 (1996).
- [7] D. W. Vernooy, *et al.*, High-Q measurements of fused-silica microspheres in the near infrared, *Opt. Lett.* **23**, 247-249 (1998).
- [8] B. Di Bartolo and O. Forte, *Frontiers of Optical Spectroscopy*, (Springer, Netherlands, 2005).
- [9] I. Teraoka and S. Arnold, Theory of resonance shifts in TE and TM whispering gallery modes by nonradial perturbations for sensing applications, *J. Opt. Soc. Am. B* **23**, 1381-1389 (2006).
- [10] S. Arnold, S. I. Shopova, and S. Holler, Whispering gallery mode bio-sensor for label-free detection of single molecules: thermo-optic vs. reactive mechanism, *Opt. Express* **18**, 281-287 (2010).
- [11] S. I. Shopova, Nanoparticle-coated optical microresonators for whispering-gallery lasing and other applications, University of Sofia Kliment Ohridski, 1989.

[12] Craig F. Bohren and Donald R. Huffman, *Absorption and Scattering of Light by Small Particles*, (John Wiley & Sons, Inc., New York, 1998).

CHAPTER 4

Functionalization and Characterization of Silica Microspheres

In current literature, a few methods have been developed for the functionalization of silica-based high Q resonators. However, all such approaches are limited to specific nanomaterials and cannot be generalized easily. A few relevant examples include recent demonstrations of silica high Q resonators coated with polymer [1], Au NPs [2, 3], and nonlinear molecules [4, 5]. The method of self-assembly has several important advantages compared with these methods. First, by depositing one monolayer of nanomaterial at a time, the self-assembly approach can control microsphere functionalization with nanoscale accuracy and maintain exceptional surface smoothness. Second, the self-assembly approach relies on electrostatic interaction and is therefore compatible with a wide range of nanomaterials including nonlinear molecules, dyes, quantum dots, and plasmonic NPs. By selecting appropriate aqueous solutions for self-assembly, we can therefore incorporate a large variety of functional materials onto the same microsphere, which can be difficult to accomplish with alternative approaches. Finally, the self-assembly process is simple, straightforward, and can be carried out without using any specialized equipment or environmental controls.

4.1 Microsphere Fabrication and Experimental Setup

Silica microspheres were fabricated by following the procedure in Ref [6]. Briefly, we placed a silica multimode (50 μm core and 125 μm cladding, purchased from Corning Inc.) fiber between two fiber clamps. We focused a high power CO₂ laser beam ($\sim 10\text{W}$) on the silica fiber to heat silica above the melting point. After melting and stretching the

fiber we applied high laser power (about 25 W) to cut the fiber. We used this high power again to formulate the microsphere with the help of surface tension. The fabrication parameters were adjusted to ensure microsphere diameters were in the range of 240-260 μm . The actual setup is shown in Fig. (4.1). The procedures for microsphere fabrication are shown Fig. (4.2).

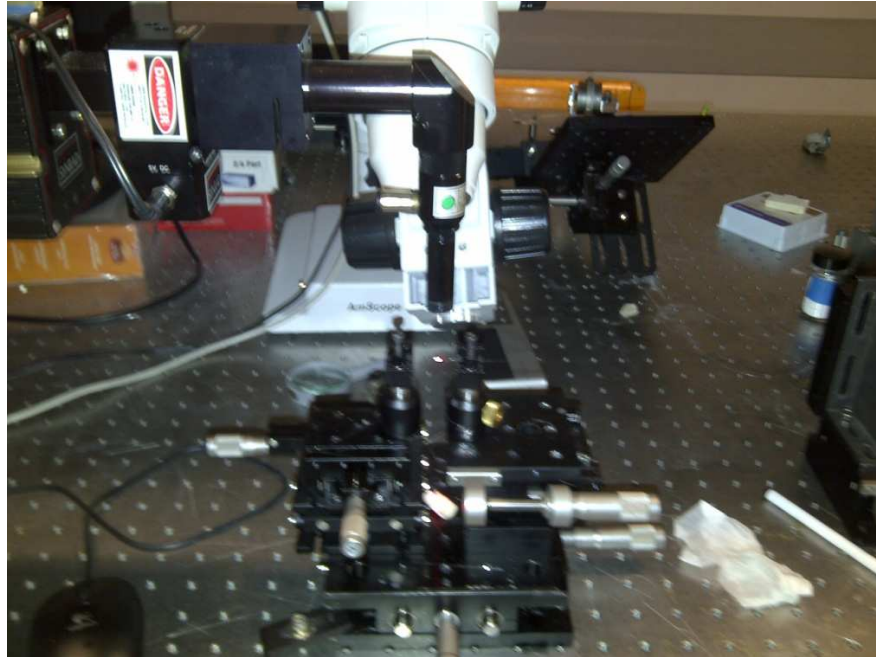
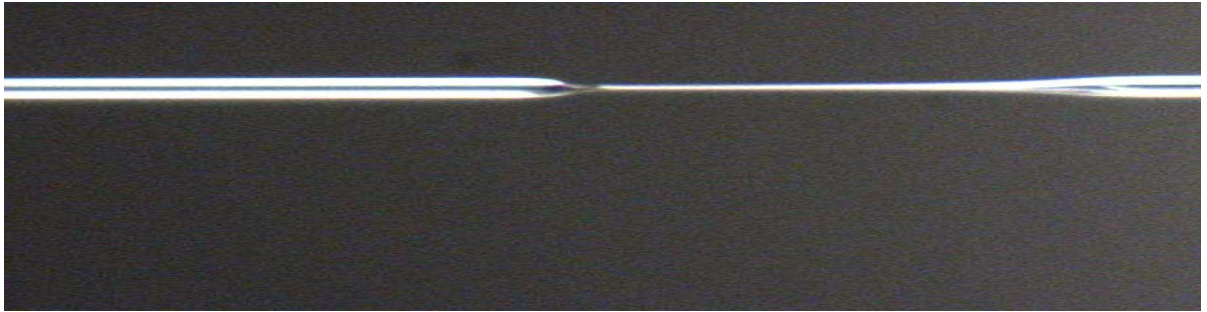


Fig. (4.1) Setup for microsphere fabrication.

After microsphere fabrication, we coated the silica surface with two different ISAM films, with one composed of alternating layers of (poly (allylamine hydrochloride)) (PAH) and (poly {1-[p-(3'-carboxy-4'-hydroxyphenylazo) benzenesulfonamido]-1, 2-ethandiyl} (PCBS) and the other composed of PAH and Procion Brown (PB). ISAM films of PAH/PCBS and PAH/PB have been shown to possess net polar order and substantial second order nonlinear optical susceptibilities [7, 8].



(a)



(b)



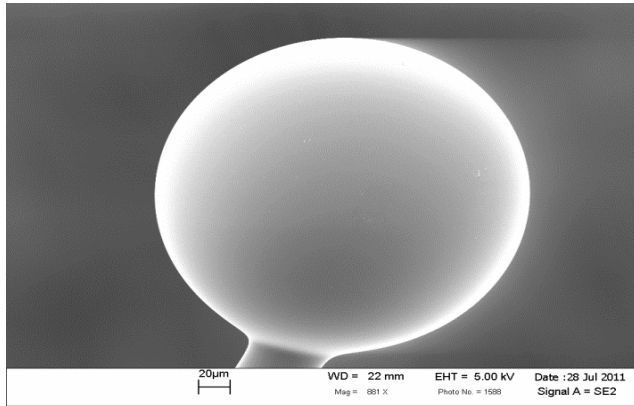
(c)

Fig. (4.2) Microsphere fabrication: (a) melting the fiber by CO₂ laser beam and stretching it, (b) cutting the fiber with very high power, and (c) forming the microsphere.

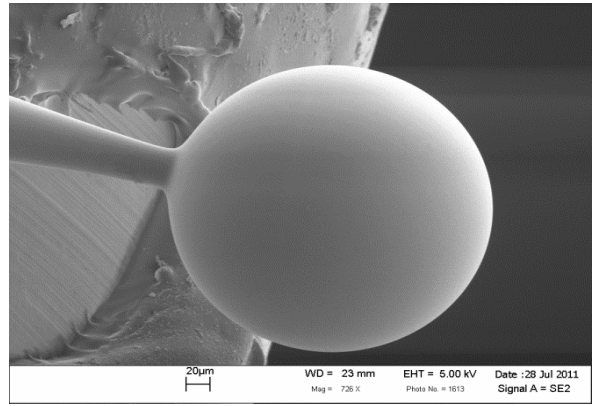
The self assembly procedure is as follows. First, we placed the microsphere in the positively-charged polycation (PAH) solution for 3 minutes followed by 2 minutes deionized (DI) water rinsing to ensure uniform PAH coverage. Afterwards, we placed the microsphere in the negatively-charged polyanion solution containing PCBS (or PB) for 3 minutes to cover the PAH layer with a monolayer of PCBS (or PB). This step is again followed by 2 minutes DI water rinsing to remove any residual polyanion. Because self-assembly relies on electrostatic interaction, the process is self-limiting, and each polymer layer with a well-defined thickness (typically 0.3 - 10.0 nm dependent on solution pH and ionic strength) is added at each deposition step. As a result, the thickness of the ISAM film can be controlled with nanoscale resolution (i.e., the thickness of a single polymer layer). We can also easily reach the desired ISAM film thickness by repeating the process described above until a sufficient number of polymer monolayer has been deposited. For this experimental study, PAH, PCBS, and PB were purchased from SIGMA-ALDRICH. The concentrations and the pH values are respectively 0.93 mg/mL and PH ~7 for PAH solution, 3.7 mg/mL and pH ~7 for PCBS solution, and 1 mg/mL and pH ~10.5 for PB solution. For the fabrication of PAH/PB ISAM films, we added sodium chloride into the PB solution at a concentration of 30 mg/mL. The Na⁺ ions screen the repulsions of the negatively-charged enabling close packing of PB on the surface [9].

The assembly of Au NPs was carried out using the same principle. We first coated the silica microsphere with a monolayer of positively-charged PAH. Then we placed the PAH-coated microsphere in an aqueous solution containing negatively-charged Au NPs (30 nm in diameter, British Biocell International). The density of Au nanospheres adsorbed on the microsphere surface can be readily adjusted by controlling deposition

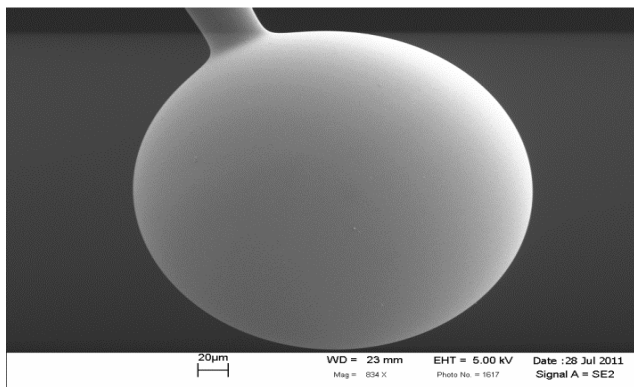
time. More details can be found in Ref [10] and Chapter 5, where we provided an analytical model that describes the density of adsorbed Au nanospheres as a function of deposition time. The fabrication procedure described above can produce functional microspheres with very smooth surfaces. Coated microspheres with different number of bilayers of PAH/PCBS can be shown in Fig. (4.3).



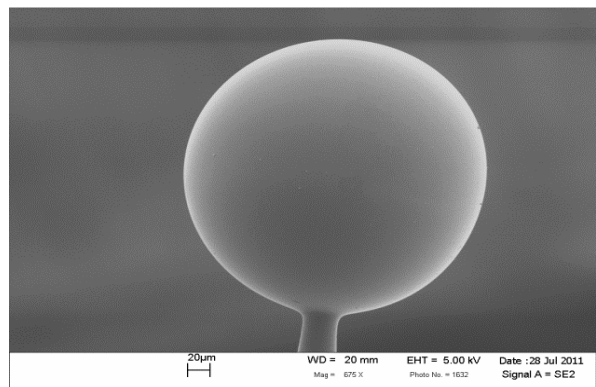
(a)



(b)



(c)



(d)

Fig. (4.3) SEM images for different number of bilayers of PAH/PCBS: (a) 1Bilayer, (b) 10 Bilayers, (c) 15 Bilayers, and (d) 20 Bilayers.

Also, SEM images of microspheres coated with Au NPs are shown in Fig. (4.4).

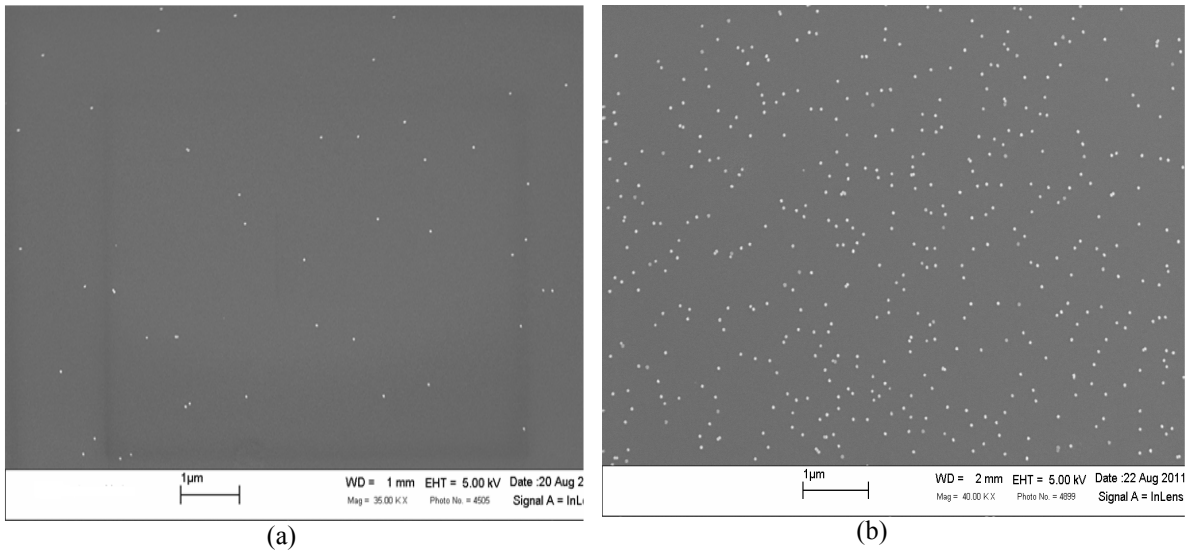


Fig. (4.4) SEM images for different deposition times of Au NPs on a microsphere: (a) 0.5 min in 10% diluted solution, (b) 20 min. in 10% diluted solution.

Silica fiber tapers were fabricated using a heating and pulling method. The outer jacket was removed and the silica multimode fiber (50 μm core and 125 μm cladding, Corning Inc.) was fixed between two fiber clamps. We used a propane-oxygen flame to heat the fiber. A tube was placed between the fiber and the flame to ensure uniform heating along the fiber taper section (Fig.4.5).

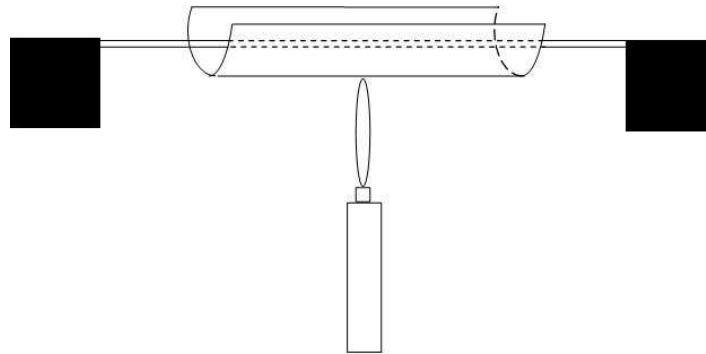


Fig. (4.5) Heating the fiber to make a fiber taper.

As the glass softened under high temperature, we used two Newport motion stages to pull the two clamps apart. The pulling speed of the motion stages was determined by

computer software (Fig. (4.6)), which enabled us to control the taper waist and its spatial profile.

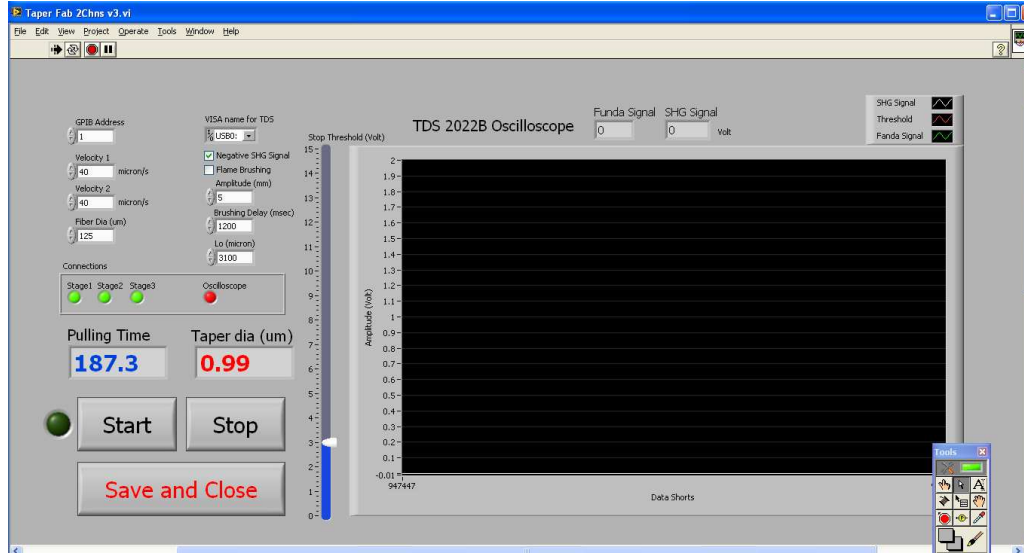


Fig. (4.6) Software to control the motion stages showing the diameter of taper.

We heated the fiber until the transmission spectrum reached its steady state. At this point, no fluctuations in the spectrum were observed, and the diameter is around $\sim 1 \mu\text{m}$. SEM image for the fiber taper is shown in Fig. (4.7).

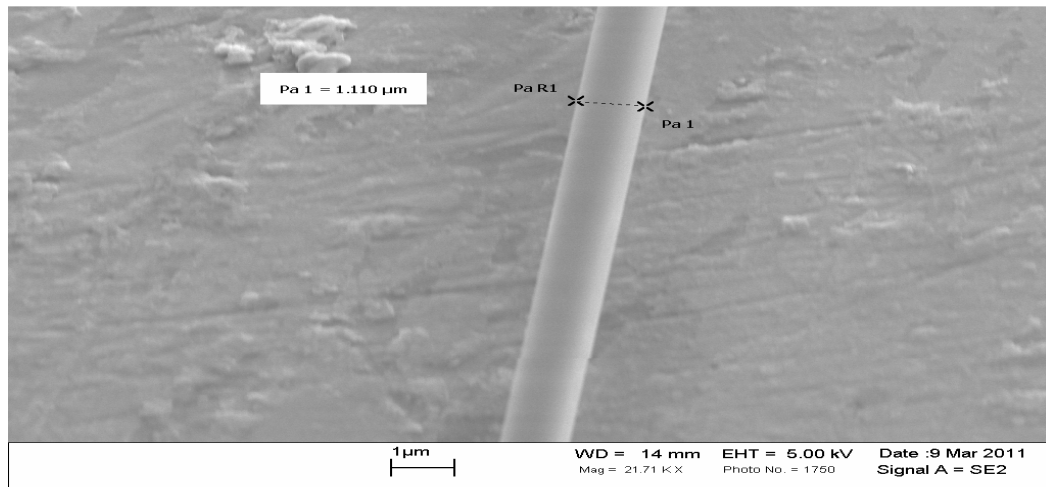


Fig. (4.7) SEM of fiber taper.

4.2 Experimental Characterization and Analysis

The WGMs within the functionalized microspheres were characterized using the experimental setup in Fig. (4.8). The output of a NEW FOCUS 6300 tunable laser diode was coupled into the microsphere using a $\sim 1 \mu\text{m}$ diameter fiber taper. The wavelength of the tunable laser was controlled using the voltage signal produced by a function generator, where the 2 V (peak to peak) signal corresponded to a 0.16 nm tuning range. The photodetector converted the optical signals in the taper (after microsphere transmission) into electronic signals. The transmission spectra were then recorded by the oscilloscope. We used a fiber paddle to adjust the polarization of the laser input. In following studies, we always adjust the polarization state of the input laser light to find the WGMs with the highest Q factors. The WGM Q factors were calculated using [6]

$$Q = \frac{\lambda_R}{\Delta\lambda} \quad (4.1)$$

where λ_R and $\Delta\lambda$ are the central wavelength and the full width half maximum of the measured transmission dips, respectively.

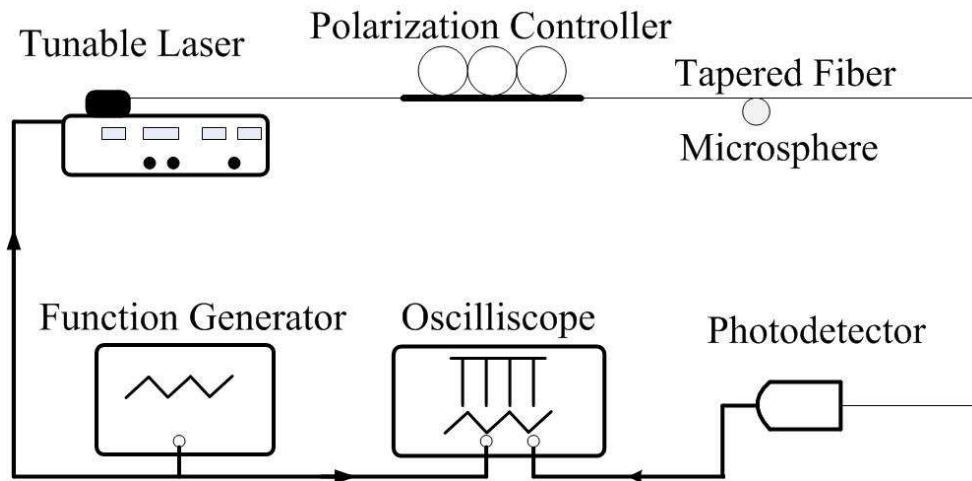


Fig. (4.8) Coupling system between the microsphere and fiber taper.

A representative example of WGM transmission spectrums are shown in Fig. 4.9, which was obtained using a microsphere coated with 1, 5, 20 bilayers of PAH/PCBS. The transmission is plotted against the deviation from 1550 nm. For our work, all Q factor measurements were carried out near 1550 nm. If multiple WGMs are found within the scanning range, we only record the highest Q factor.

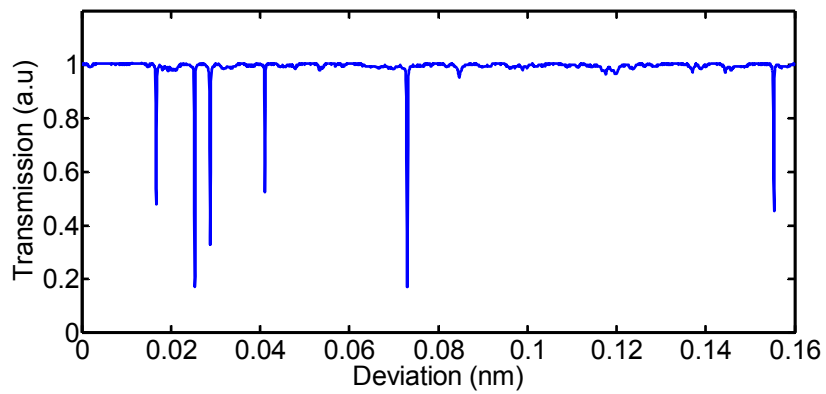
The Q factor of coated microsphere with ISAM films can be separated into four terms, as made clear by Eq. (3.56). First of all, the loss in the silica due to absorption and Rayleigh scattering can be quantized by the quality factor Q_{silica} . Q_{silica} can reach 10^{11} when the resonance wavelength is around 1550 nm [6].

Another factor that may lower cavity Q factor is surface scattering. The Q factor due to surface scattering (Q_{ss}) can be calculated from Eq. (3.58). Figure (4.10) shows a surface- morphology scan obtained by using the Atomic Force Microscopy (AFM) taken over $500 \text{ nm} \times 500 \text{ nm}$ grids ($768 \text{ point} \times 768 \text{ point}$). This figure shows 3D images for the roughness level of the surface for different sample with different number of bilayers of PAH/PCBS (1 Bilayer, 5 Bilayers, and 20 Bilayers). The roughness would increase with increasing the number of bilayers as roughness is a cumulative quantity. The AFM calculate the root mean square (rms) value of roughness level.

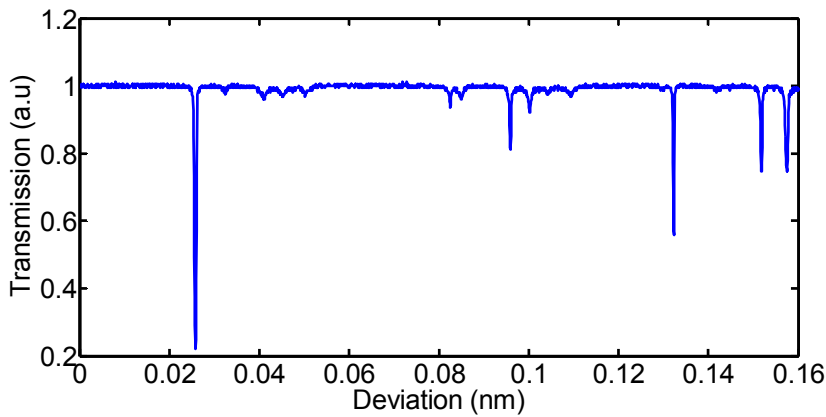
Now, we need to calculate the correlation length, B which can be obtained from the equation [12]

$$R(u) = R(0) \exp\left(-\left(\frac{u}{B}\right)^2\right) \quad (4.2)$$

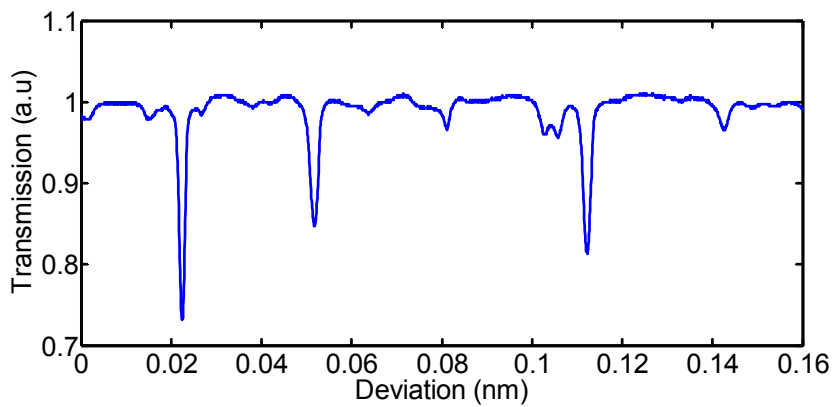
where R is the correlation function, u is the separation between different positions, and $R(0)$ is the correlation function for separation 0.



(a)



(b)



(c)

Fig. (4.9) Transmission spectrum of microsphere coated with: (a) 1 Bilayer of PAH/PCBS, (b) 5 Bilayers, and (c) 20 Bilayers.

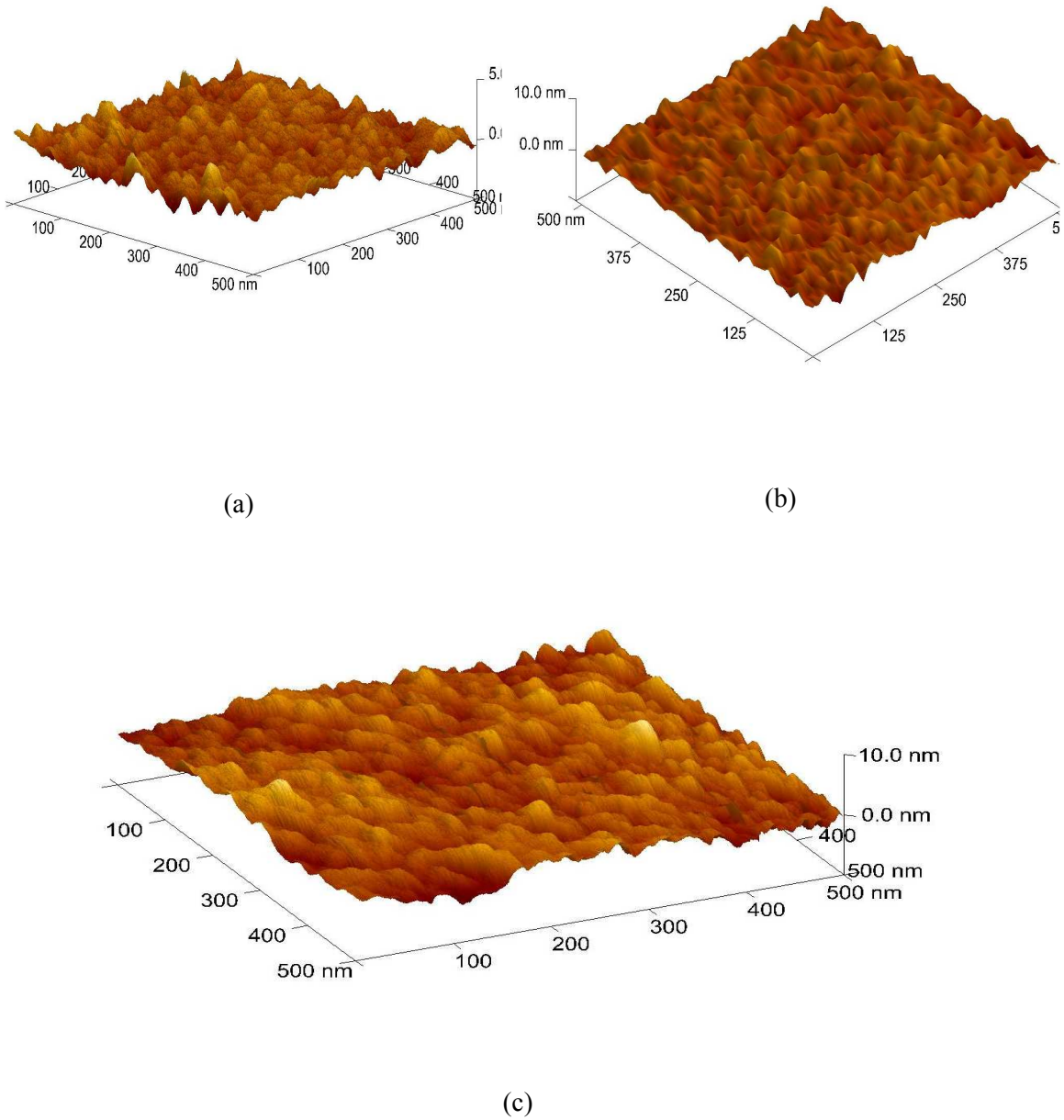


Fig. (4.10) Surface data obtained by AFM on a 500-nm square grid of 768×768 points :(a) 1 Bilayer, (b) 5 Bilayers, and (c) 20 Bilayers.

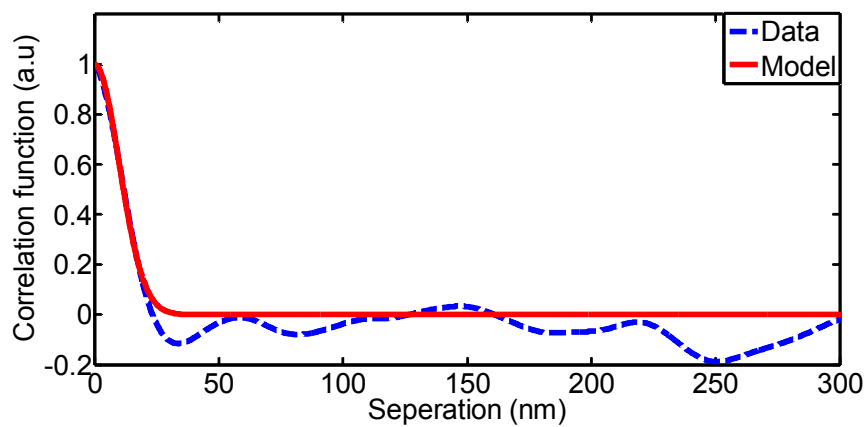
If we use $h(x, y)$ to denote surface height measured by AFM, we can define its correlation function as

$$R(u) = \iint h(x, y)h(x + u, y)dx dy \quad (4.3)$$

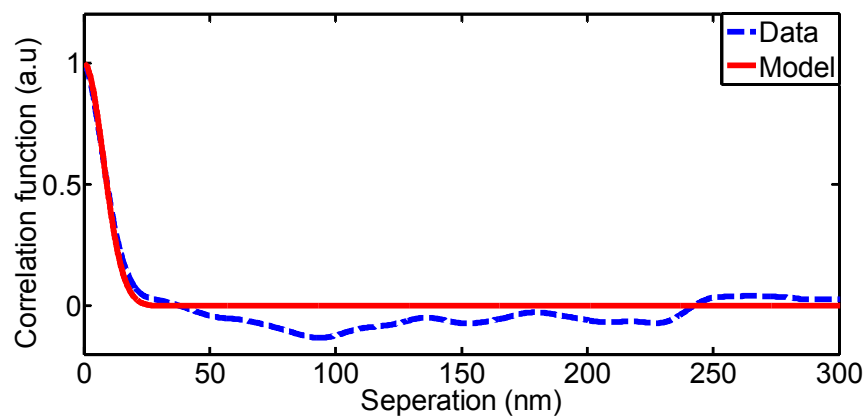
where u is the separation between two successive points in the same row.

The correlation length B can then be extracted by fitting the correlation function (Eq. (4.2)). The theoretical fit and the experimentally measured correlation function are shown in Fig. (4.11) for different number of bilayers. The red line represents the theoretical fitting according to Eq. (4.2) and the blue line corresponds to experimental measurements (Eq. (4.3)). The correlation length, according to Eq. (4.2), is the distance at which the correlation function is reduced to about 0.37 of its maximum value.

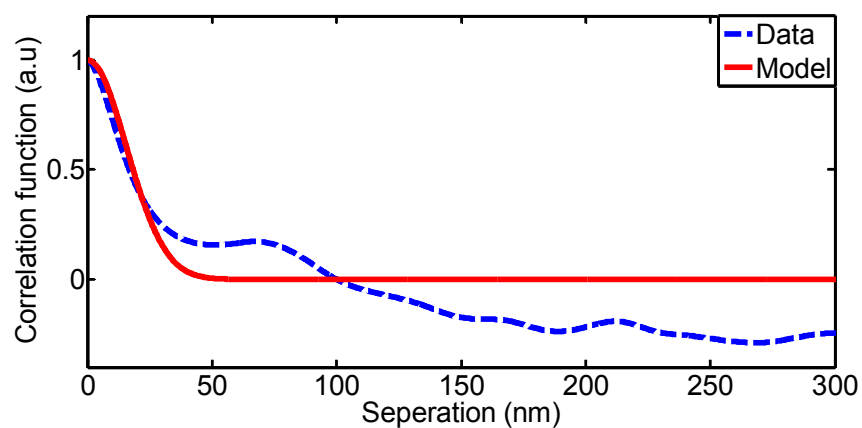
Table 1 summarizes the results for different bilayer numbers of PAH/PCBS. The data include rms roughness, correlation length, and calculated Q_{ss} from Eq. (3.58). From the summarized results in Table 1, it can be noticed that the Q_{ss} for a coated microsphere with PAH/PCBS is on order of 10^{10} to 10^{11} . In comparison, the experimentally measured Q factors of silica microspheres coated with <20 bilayers of PAH/PCBS are typically in the range of 10^6 to 10^7 (Fig. (4.13-a). This result suggests that for microspheres coated with PAH/PCBS, the excessive loss is dominated by material absorption within the ISAM film. Due to the difficulty of carrying out AFM measurements on a curved surface of mechanically fragile microspheres, we did not carry out similar studies using microspheres coated with PAH/PB. However, since deposition of PAH/PCBS and PAH/PB are carried out similarly and both ISAM films possess exceptionally smooth surface morphology on planar structures [13], the scattering losses for PAH/PB and PAH/PCBS microspheres are likely to be of the same order of magnitude.



(a)



(b)



(c)

Fig. (4.11) Theoretical and experimental correlation function: (a) 1 Bilayer, (b) 5 Bilayer, and (c) 20Bilayer of PAH/PCBS.

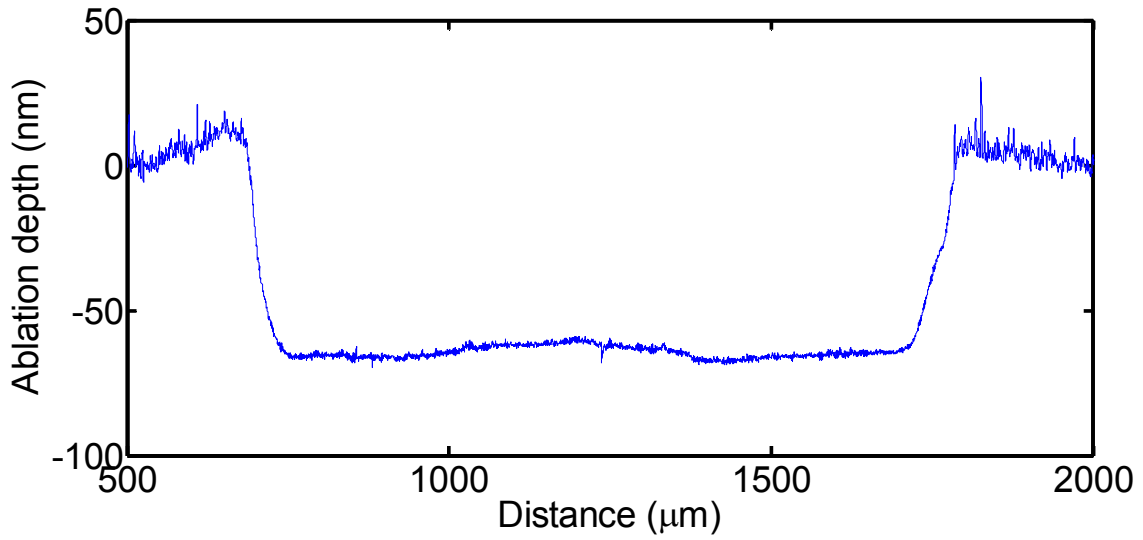
Table 1 rms roughness (nm), correlation length (nm), and quality factor due to surface scattering for different bilayer numbers of PAH/PCBS.

Bilayer number	rms Surface roughness, σ	Correlation length, B	Q_{ss}
1	0.341	14	1.18e+011
5	0.601	11	6.1e+010
20	0.790	22	3.47e+010

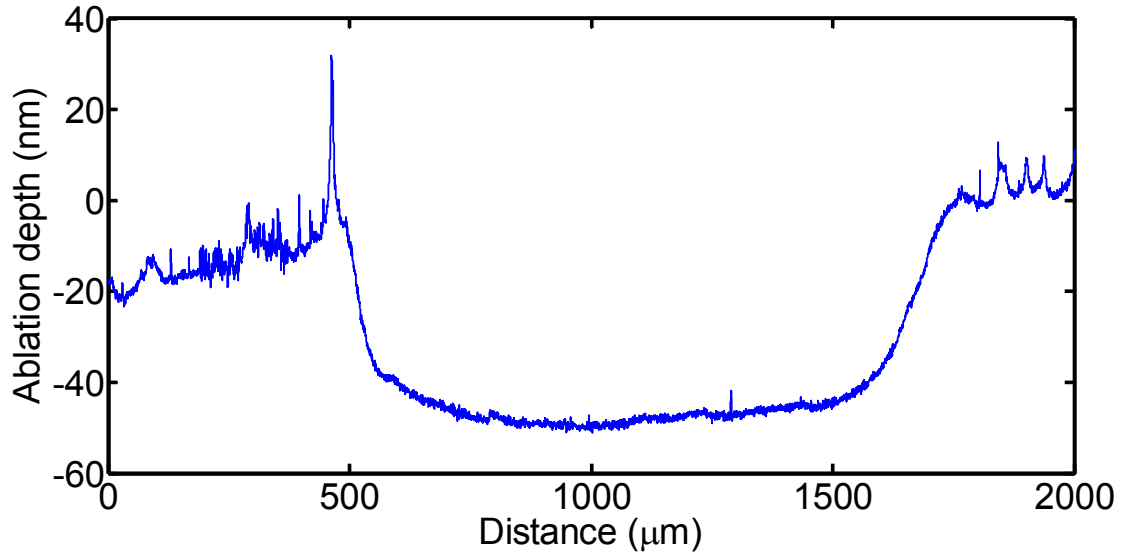
To further quantify the relationship between material absorption and cavity Q factors, we need to investigate the impact of taper-microsphere coupling loss. In particular, to minimize the impact due to changes in coupling loss, all cavity Q factors were measured when the silica microspheres are in direct contact with the coupling taper. Additionally, we also measured the Q factors of four different bare silica microspheres under this direct-contact scenario. The maximum cavity Q factors are respectively 1.73×10^7 , 1.88×10^7 , 1.95×10^7 , and 2.5×10^7 . The average Q factor is $\sim 2 \times 10^7$, with a standard deviation of 0.34×10^7 . All four bare silica microspheres possess similar diameters ($\sim 250 \mu\text{m}$). For the direct-contact cases, the cavity Q factors should be dominated by Q_{coupling} . Consequently, for functionalized microspheres with similar diameters, we can approximate their Q_{coupling} as $\sim 2 \times 10^7$.

The thickness of one bilayer, t was measured to be $\sim 1.3 \text{ nm}$ for PAH/PB and $\sim 0.9 \text{ nm}$ for PAH/PCBS. Briefly, we use a UV excimer laser beam with fluence above the film threshold but below glass threshold to remove a small area on the film layer. We use the UV laser for 5 minutes which is sufficient to remove 50 bilayers of PAH/PCBS or

PAH/PB from certain area. Then the film thickness was determined by using a Dektak Profilometer. The surface profile of glass substrate with 50 bilayers of PAH/PB is shown in Fig. (4.12-a) and with 50 bilayers of PAH/PCBS is shown in Fig. (4.12-b).



(a)



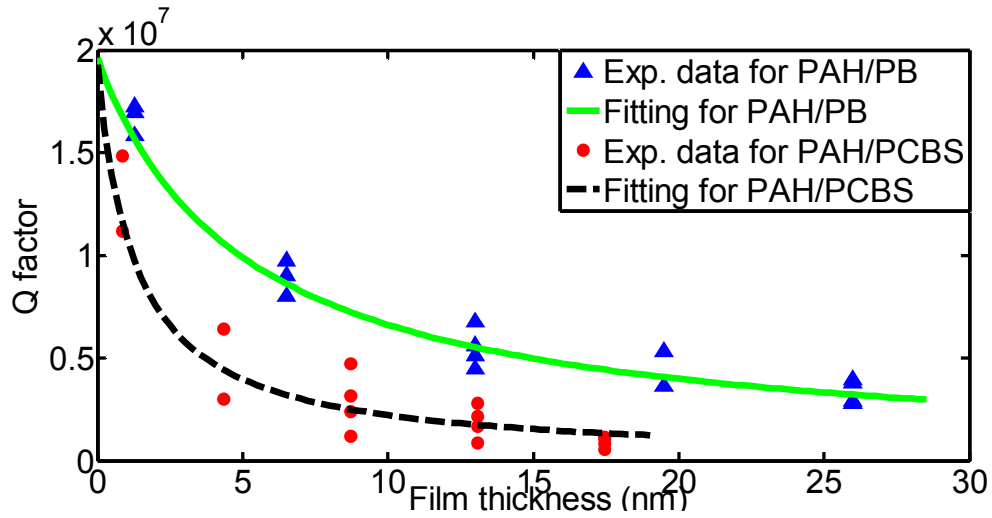
(b)

Fig. (4.12) Surface profile of film after ablation for: (a) 50PAH/PB, and (b) 50PAH/PCBS.

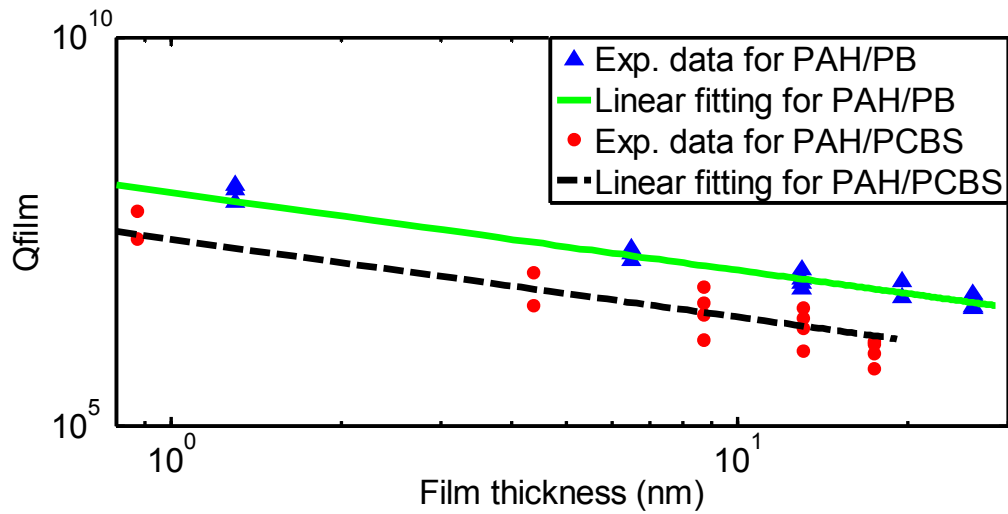
The measured Q factor of microspheres coated with different numbers of PAH/PCBS and PAH/PB bilayers is shown in Fig. (4.13-a). From graph, Q_{coupling} is $\sim 1.96 \times 10^7$ for PAH/PB and is $\sim 1.93 \times 10^7$ for PAH/PCBS.

In Fig. (4.13-b), we show the experimentally measured Q_{film} , which are calculated by subtracting coupling loss from the total Q factors. As discussed earlier, loss due to silica absorption and scattering are much smaller compared with coupling loss, and are consequently ignored. To extract the relationship between Q factors and film thickness, we performed a linear fitting between Q_{film} and film thickness in logarithmic scale. For PAH/PB, the slope of the linear fitting is -1.1 and for PAH/PCBS it is -1.14.

A natural explanation for this result is that cavity loss of the functional microspheres is dominated by material absorption within the ISAM film. In this case, the modal loss should increase linearly as a function of the total volume of the polymer coating. Since film thickness is approximately 1.3 nm per PAH/PB bilayer and 0.9 nm per PAH/PCBS bilayer, the rate of material absorption, which is represented by $1/Q_{\text{film}}$, should be proportional to the total bilayer number of the ISAM film, i.e., $1/Q_{\text{film}} \propto N_{\text{ISAM}}$. This theoretical prediction is very close to our experimental results. The deviation from the theoretical fitting curve can be explained by several factors. First of all, the coupling between the fiber taper and the microsphere may not be identical for different microsphere samples. The geometrical dimensions of different microspheres may not be identical. The process of ISAM film deposition is not perfect clean, thus some dust particles may accumulate on the surface of the microsphere and cause the Q factor to drop in an uncontrollable fashion.



(a)



(b)

Fig. (4.13): (a) Q factors as a function of film thickness (t) for microsphere coated with PAH/PB and PAH/PCBS, (b) theoretical and experimental result for quality factor due to added film as a function of film thickness (t) for microsphere coated with PAH/PB and PAH/PCBS. The green and black lines are the fitting curves for PAH/PB and PAH/PCBS, respectively.

To investigate the impact of Au NPs on WGM Q factors, we fabricated multiple samples with different Au NP density on the microsphere surface. This was accomplished by adjusting the duration in which microspheres were immersed in solution. After Q factor measurement, we took SEM images of the microsphere samples, and obtained NP density from the SEM images. The measured microsphere Q factors were plotted as a function of NP density, and shown in Fig. (4.15). As expected, the cavity Q factors decrease as NP density increases. To further quantify the behavior of cavity Q factors as a function of NP density, we can use the theoretical model described in Chapter 3. The ratio between Q factor of TE modes and Q factor of TM Q is the factor R'_l (Eq. (3.100)). In Fig. (4.14), we plotted the ratio, R'_l for the fundamental modes. In our calculations, the radius of microsphere is 125 μm . The refractive index of silica at 1550 nm is 1.44. We can see that if the refractive index of surrounding medium equals 1 (air), the ratio, R'_l is 1.532. This suggests that a long as we measure the highest Q factor in the transmission spectrum, we assume that we measure the Q factor of the fundamental TE mode.

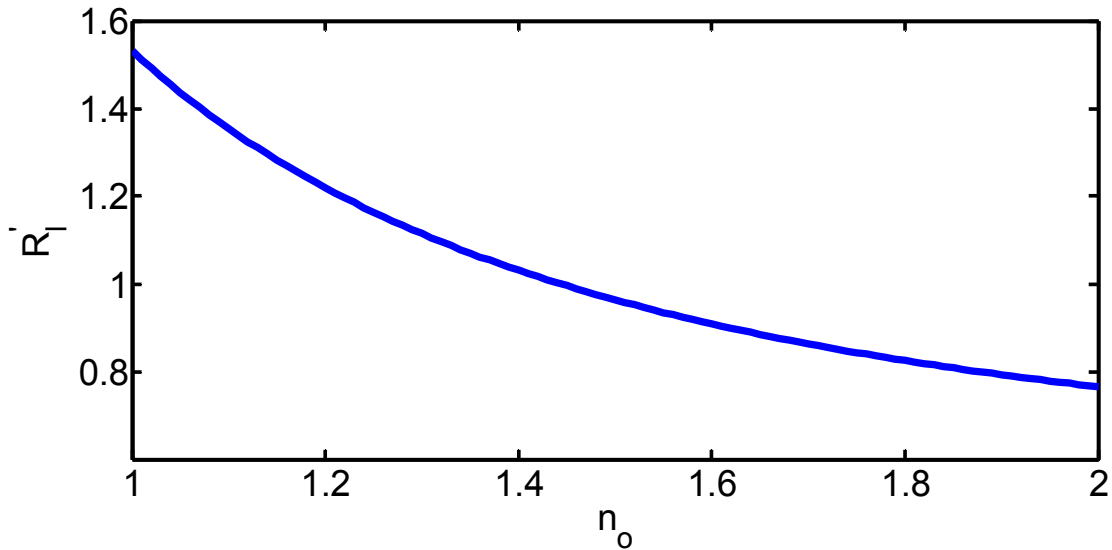


Fig. (4.14) TE-to-TM Q factor ratio plotted as a function of refractive index of surrounding medium.

The theoretical Q factor of TE fundamental can be calculated from Eq. (3.97) and Eq. (3.99). In Fig. (4.15), we compare the experimentally measured and the theoretically estimated Q factors. In our theoretical estimate, the radius of Au NP is 15 nm, while the radius of the microsphere is 125 μm on average. The refractive index of Au at wavelength 1550 nm is $0.52406+i 10.72$ based on the data in Ref [14]. A good agreement can be noticed for low particles density. It should be pointed out that the higher density of Au NPs is expected to cause a difference between the theory and experiment since the loss due to aggregation of particles has not been considered.

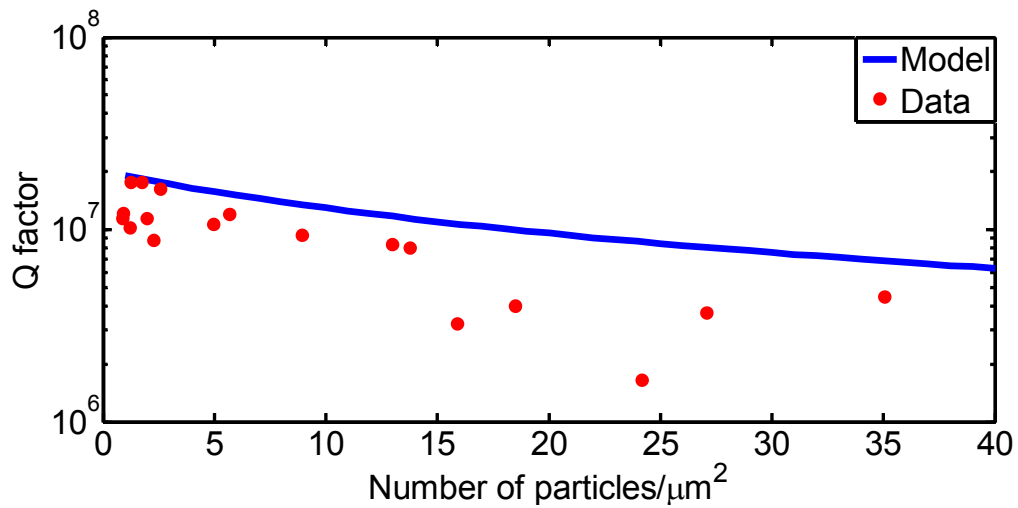


Fig. (4.15). Theoretical and experimental results for Q factor as a function of Au NPs density on the surface of silica microsphere.

Reference

- [1] Hong Seok Choi, Xiaomin Zhang, and Andrea M. Armani, Hybrid silica-polymer ultra-high- Q microresonators, *Opt. Lett.* **35**, 459-461 (2010).
- [2] S.I Shopova, C.W Blackledge, and A.T Rosenberger, Enhanced evanescent coupling to whispering-gallery modes due to gold nanorods grown on the microresonator surface, *Appl. Phys. B* **93**, 183-187 (2008).
- [3] Miguel A. Santiago-Cordoba, Svetlana V. Boriskina, Frank Vollmer and Melik C. Demirel, Nanoparticle-based protein detection by optical shift of a resonant microcavity, *Appl. Phys. Lett.* **99**, 073701:1-3 (2011).
- [4] Gregory Kozyreff, Jorge Luis Dominguez-Juarez, and Jordi Martorell, Nonlinear optics in spheres: from second harmonic scattering to quasi-phase matched generation in whispering gallery modes, *Laser Photonics Rev.* **5**, 737-749 (2011).
- [5] J.L. Dominguez-Juarez, G. Kozyreff and Jordi martorell, Whispering gallery microresonators for second harmonic light generation from a low number of small molecules, *Nature Commun.* **2**, 1-8 (2011).
- [6] Alessandro Chiasera, *et al.*, Spherical whispering-gallery-mode microresonators, *Laser Photonics Rev.* **4**, 457-482 (2010).
- [7] Akhilesh Garg, *et al.*, Polar orientation of a pendant anionic chromophore in thick layer-by-layer self-assembled polymeric films, *Appl. Phys.* **104**, 053116:1-8 (2008).
- [8] Kevin E. Van Cott, *et al.*, Layer-By-Layer Deposition and Ordering of Low-Molecular-Weight Dye Molecules for Second-Order Nonlinear Optics, *Angew. Chem. Int. Ed.* **41**, 3236 - 3238 (2002).

- [9] James R. Heflin, *et al.*, Efficient, Thermally Stable, Second Order Nonlinear Optical Response in Organic Hybrid Covalent/Ionic Self-Assembled Films, *Langmuir* **22**, 5723-5727 (2006).
- [10] Jihaeng Yi, Chih-Yu Jao, Ishac L.N. Kandas, Bo Liu, Yong Xu, *et al.*, Irreversible adsorption of gold nanospheres on fiber optical tapers and microspheres,” *Appl. Phys Lett.* **100**, 153107: 1-4 (2012).
- [11] M. L. Gorodetsky, A. A. Savchenkov, and V. S. Ilchenko, ”Ultimate Q of optical microsphere resonators,” *Opt. Lett.* **21**, 453-455 (1996).
- [12] F. P. Payne and J. P. R. Lacey, A theoretical analysis of scattering loss from planar optical waveguides, *Opt. Quantum Electron.* **26**, 977-986 (1994).
- [13] Chalongrat Daengngam, *et al.*, Demonstration of a cylindrically symmetric second-order nonlinear fiber with self-assembled organic surface layers, *Opt. Express* **19**, 10326-10335(2011).
- [14] P. B. Johnson and R. W. Christy, Optical Constants of the Noble Metals, *Phys. Rev. Lett.* **6**, 4370-4379 (1972).

CHAPTER 5

Irreversible Adsorption of Au NPs on Flat Surfaces and Microspheres

5.1 Adsorption of NPs

Plasmonic resonances in metal NPs have attracted the attention recently in sensors and other applications [1-3] . In many applications, NPs are deposited from a suspended liquid form a plasmonically active surface [4-8]. Usually, the used surface is flat, but other geometries like cylindrical and spherical shapes can be used and have interesting applications. The dependence of deposition of Au NPs on the surface geometry is fully studied [9]. At short deposition times, the NP adsorption is largely independent of substrate geometry, while at long times, deposition is significantly faster onto the curved surfaces. The crossover occurs when the NP diffusion length equals the radius of curvature of the surface.

The problem of particle adsorption on a collecting surface is of great technological importance in fields such as materials science, food and pharmaceutical fabrication, electrophoresis, catalysis, etc. It is also of interest in biomedicine in describing processes such as ligand binding to macromolecules or digestion by microbes and cells [10, 11]. It is then not surprising that the problem has been studied for a long time and those theoretical treatments have reached a high degree of sophistication [12- 14]. However, the bulk of the experimental work in this field has been done on planar surfaces, and studies of adsorption onto curved collecting surfaces [11, 15, 16] have generally

concerned regimes that are not directly applicable to optical and plasmonic device fabrication.

5.2 Diffusion Model of Irreversible Adsorption of Au NPs on Microspheres

For our theoretical treatment, we confine ourselves to the simplest possible case, where we first assume that the collecting surfaces are perfect sinks, *i.e.* that any particle that gets within a certain small distance from a surface sticks immediately and irreversibly, which is reasonable for small particles at low concentrations [17, 18] and at time scales where the fast adhesion kinetics is masked by the slower particle transport to the surface. We also assume that the drag experienced by a particle near a surface is balanced by attractive dispersion forces (the Smoluchowski-Levich approximation), so that we can take the diffusion coefficient to be constant everywhere and ignore the presence of the surface. Finally, we treat only the case where there are no external forces and no liquid flow present (quiescent conditions). In the absence of flow, the motion of the particles in the liquid is governed by the diffusion equation

$$\frac{\partial n(r,t)}{\partial t} = D\Delta n(r,t). \quad (5.1)$$

Under spherical symmetry, the diffusion equation can be expressed by

$$\begin{cases} \frac{\partial n(r,t)}{\partial t} = \frac{1}{r^2} \frac{\partial}{\partial r} \left(Dr^2 \frac{\partial n(r,t)}{\partial r} \right), \\ n(a,t) = 0, \\ n(r > a, 0) = n_0, \end{cases} \quad (5.2)$$

where a is the radius of a microsphere, D is the diffusion constant, which is independent of position and concentration, and n_0 is the nominal particle concentration.

The differential equation (Eq. (5.2)) is separable, so its solution can be written as

$$n(r, t) = \int R_\beta(r) T_\beta(t) d\beta \quad (5.3)$$

Then, we have

$$\frac{1}{D} \frac{T'}{T} = \frac{R''}{R} + \frac{2}{r} \frac{R'}{R} = -\beta^2, \quad (5.4)$$

where β is a real positive number. The solutions for T and R become

$$\begin{cases} T_\beta(t) = e^{-Dt\beta^2}, \\ R_\beta(r) = A_\beta \frac{\sin \beta r}{\beta r} + B_\beta \frac{\cos \beta r}{\beta r}, \end{cases} \quad (5.5)$$

where A_β and B_β are constants.

Each of the particular solutions must satisfy the boundary condition, $R_\beta(a) = 0$ which means that

$$R_\beta(r) = \frac{C_\beta}{\beta r} (\sin \beta r \cos \beta a - \sin \beta a \cos \beta r) = \frac{C_\beta}{\beta r} \sin \beta(r - a), \quad (5.6)$$

where C_β is another constant. We must search for C_β such that the initial conditions are satisfied. In other words, we must have

$$\int_0^\infty \frac{C_\beta}{\beta r} \sin \beta(r - a) d\beta = n_0, r > a. \quad (5.7)$$

To solve this, we reformulate the initial condition as $n(r > a, 0) = \lim_{Q \rightarrow \infty} n_0 \Pi(2Q)$,

where $\Pi(x)$ is the rectangle function. By making the substitution $p = r - a$, we have

$$\int_0^\infty \frac{C_\beta}{\beta} \sin \beta p d\beta = (p + a)n_0 \Pi(2Q) \quad p > 0. \quad (5.8)$$

We cannot actually take the exact sine transform of this equation, since the right hand side is only defined for $p > 0$. Instead we act with $\int_0^\infty \sin(vp) dp$ on the equation

$$\int_0^\infty \int_0^\infty \frac{C_\beta}{\beta} \sin(\beta p) \sin(vp) d\beta dp = n_o \int_0^Q (p + a) \sin(vp) dp. \quad (5.9)$$

Since $\sin(\beta p)$ is odd in p , we can take

$\int_0^\infty \sin(\beta p) \sin(vp) dp = \frac{1}{2} \int_{-\infty}^\infty \sin(\beta p) \sin(vp) dp$ on the left hand side, and then reverse the order of integration. The left-hand side of the equation is then

$$\int_0^\infty \frac{C_\beta}{2\beta} \int_{-\infty}^\infty \sin(\beta p) \sin(vp) dp d\beta = \int_0^\infty \frac{C_\beta}{2\beta} \pi (\delta(v - \beta) + \delta(v + \beta)) d\beta = \frac{\pi}{2} \left(\frac{C_\beta}{\beta} - \frac{C_{-\beta}}{\beta} \right) \quad (5.10)$$

β must be positive for the differential equation to make sense, so $C_{-\beta} = 0$. After some calculations, the right hand side can be expressed as

$$n_o \int_0^Q (p + a) \sin(vp) dp = \frac{n_o a}{\beta} \left[1 - \left(\frac{Q}{a} + 1 \right) \cos(\beta Q) + \frac{\sin \beta Q}{\beta a} \right]. \quad (5.11)$$

So,

$$C_\beta = \frac{2n_o a}{\pi} \left[1 - \left(\frac{Q}{a} + 1 \right) \cos(\beta Q) + \frac{\sin \beta Q}{\beta a} \right]. \quad (5.12)$$

As $Q \rightarrow \infty$, the contribution of the middle term in this expression to $n(r, t)$ goes to 0, so we obtain

$$n(r, t) = \frac{2n_o a}{\pi} \lim_{Q \rightarrow \infty} \int_0^\infty e^{-Dt\beta^2} \left(1 + \frac{\sin(\beta Q)}{\beta a} \right) \left(\frac{\sin \beta(r-a)}{\beta r} \right) d\beta. \quad (5.13)$$

This gives

$$\Phi_{\text{sph}}(t) = D \frac{\partial n(a,t)}{\partial r} = \frac{2n_0 D}{\pi} \lim_{Q \rightarrow \infty} \int_0^\infty e^{-Dt\beta^2} \left(1 + \frac{\sin(\beta Q)}{\beta a}\right) d\beta = n_0 \left(\sqrt{\frac{D}{\pi t}} + \frac{D}{a}\right), \quad (5.14)$$

where $\Phi_{\text{sph}}(t)$ is the flux of particles, which can be integrated to yield

$$\langle N_{\text{sph}} \rangle = n_0 \left(2\sqrt{\frac{Dt}{\pi}} + \frac{Dt}{a}\right). \quad (5.15)$$

In other words, at short times, we recover the flat surface result, while deposition is faster at long times, reaching a constant rate when $t \gg \frac{a^2}{D}$. For a flat surface, we can consider the first term only, so

$$\langle N_{\text{flat}} \rangle = 2n_0 \sqrt{\frac{Dt}{\pi}}. \quad (5.16)$$

The formula $\langle N_{\text{flat}} \rangle$ for is well-known and has been repeatedly been shown to describe irreversible particle deposition onto flat adhesive surfaces quite well [19, 20, 21], so long as the surface particle density is low enough that the assumption of a perfectly adhesive surface remains valid.

5.3 Experimental Verification and Analysis

To make the flat and spherical surfaces adhesive, we coated them with a single nm-thick layer of poly(allylamine hydrochloride) (PAH) to generate a uniform positive surface charge. We then placed the samples in an aqueous solution containing negatively charged citrate-terminated, surfactant free gold nanospheres (30 nm diameter, from British Biocell International) to initiate the deposition. We adjusted the NP concentration (n_0) as well as the deposition time (t) to achieve different surface particle densities, which were then

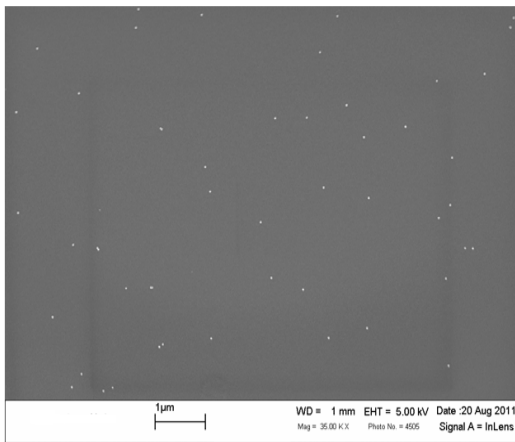
determined by SEM imaging. The NP size d and stock suspension concentration n_s were verified with TEM and inductively coupled plasma atomic emission spectroscopy (ICP-AES), and found to be 28.7 nm and 1.95×10^{11} particles/cm³ respectively, quite close to the values provided by the manufacturer (30 nm and 2.00×10^{11} particles/cm³). From d , the temperature of the suspension (22°C) and the viscosity of water at that temperature (0.96 cP), we calculated the diffusion constant for the NPs $D = 1.57 \times 10^{-7}$ cm²/s with the Einstein-Stokes equation. To reduce the number of NPs adsorbed onto the surfaces during long depositions to the point where particle surface blocking⁷ was not a factor, the stock NP suspension was diluted with DI water so that n_0 ranged between 3.0% and 10% of n_s .

For a flat glass substrate, we used the RCA cleaning method to clean the surface and charge it with negative charge before coating it with a PAH layer. As a first step, we make a solution of DI water, NH₄ OH, and H₂O₂ with ratios 5:1:1 v: v respectively. Then, we insert the substrates in the solution and heat the solution for 10 minutes while the temperature is kept between 75 and 80 C°. After that, we rinse the sample with DI water. In the second step, we make a solution of DI water, HCl, and H₂O₂ with ratios 6:1:1 v: v respectively. Then, we insert the substrates in the solution and heat the solution for 10 minutes while the temperature is kept between 75 and 80 C°.

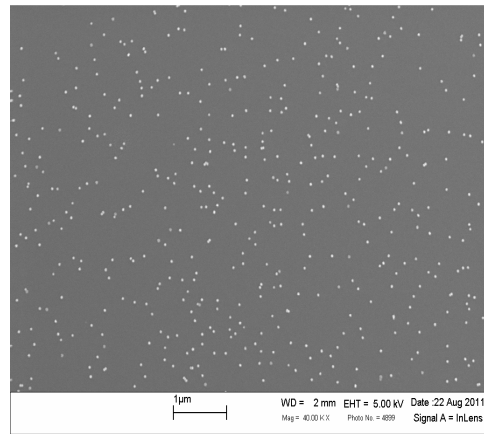
First, we deposit a PAH layer on a flat substrate (after RCA cleaning) and a microsphere surface for 3 minutes. The PAH solution is made from 465 gm (PAH) and 500 mL of DI water. Then, we leave the solution on the stirring stage for sufficient time (more than 12 hours). The PH value of this solution is set to be 7. After PAH depositions on the flat surface and microsphere surface, we rinse the sample in DI water for 2

minutes. Then, we immerse them into Au NPs solution for different deposition time. We used 30% percent diluted solution of Au NPs for the flat surface. For the microsphere, we used 10% percent diluted solution for short time (up to 2 hours) and 3% percent diluted solution for long time (greater than 2 hours) to avoid aggregation of particles.

For a microsphere, we made a deposition of Au NPs with time from 0.5 minutes to 12 hours. The number of particles is generally increased with increased deposition time. For long deposition time (greater than 2 hours), aggregation may occur. So, we used 3 percent diluted solution in this case and made a scaling factor of 10/3 for the measured values in order to be able to draw all the data in one graph. A SEM image for different deposition times is shown in Fig.(5.1) for microsphere and in Fig. (5.2) for a flat substrate.



(a)



(b)

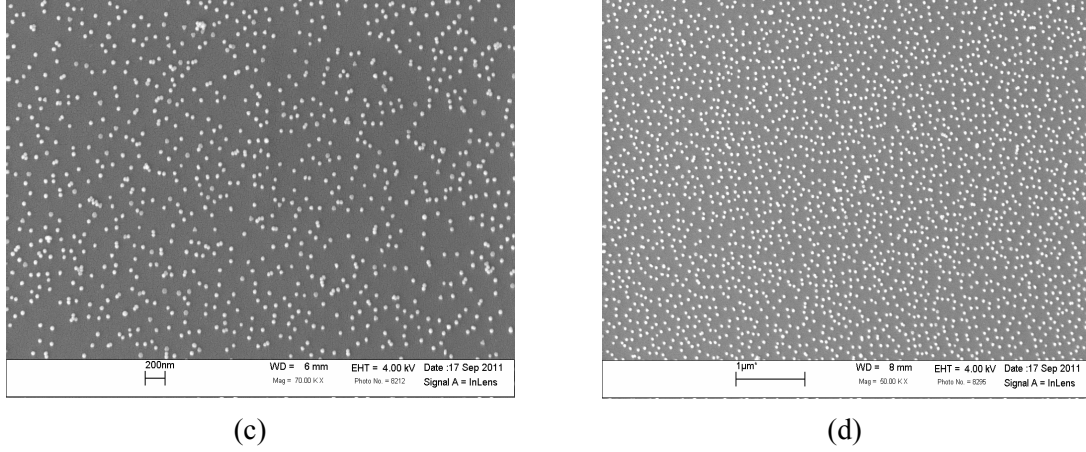


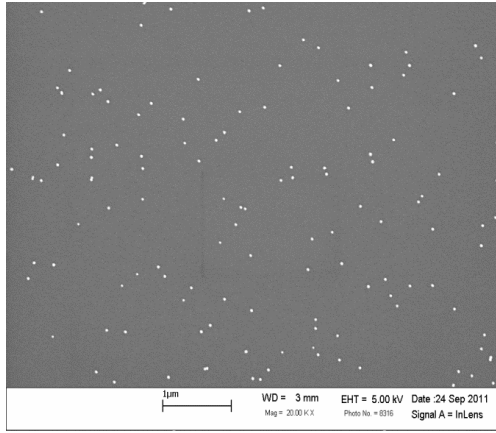
Fig. (5.1) SEM images for different deposition times of Au NPs on a microsphere: (a) 0.5 min in 10% diluted solution, (b) 20 min. in 10% diluted solution, (c) 6 hour in 3% diluted solution, and (d) 12 hours in 3 % diluted solution.

We counted the particle density (Number/ μm^2) in each case. We took five different positions in each sample and also used 3 or 4 samples for each deposition time.

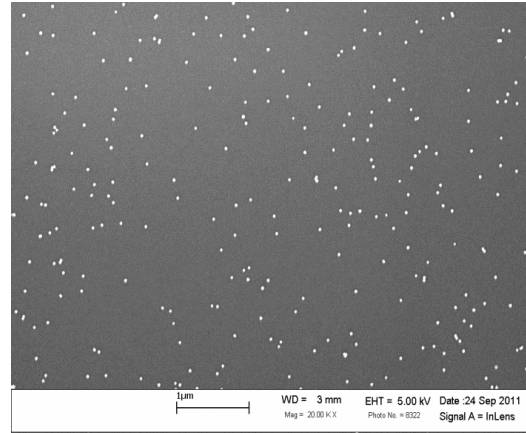
The diffusion constant, D , for spherical particles in a liquid is given by $\frac{kT}{6\pi\eta r_s}$, where η is the dynamical viscosity of the fluid, and r_s is the particle radius. Using $\eta = 1.0 \times 10^{-3}$ Pa·s for water at 22 °C, and r_s was measured to be 14.35 nm on average (nominal value is 15 nm); we obtain $D = 1.57 \times 10^{-7}$ cm²/s. Also we measured the particle concentration, n_o to be 1.95×10^{11} /mL while the Ted Pella's nominal value is 2×10^{11} /mL. To simplify matters, we introduce dimensionless measures of time (normalized time), $\tau = Dt/a^2$ and normalized particle density, $\langle v(\tau) \rangle = \langle N \rangle / n_o a$.

$$\langle v_{sph}(\tau) \rangle = 2 \sqrt{\frac{\tau}{\pi}} + \tau. \quad (5.17)$$

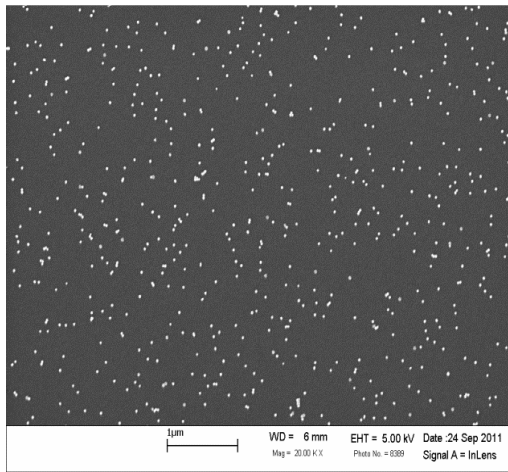
$$\langle v_{flat}(\tau) \rangle = 2 \sqrt{\frac{\tau}{\pi}} \quad (5.18)$$



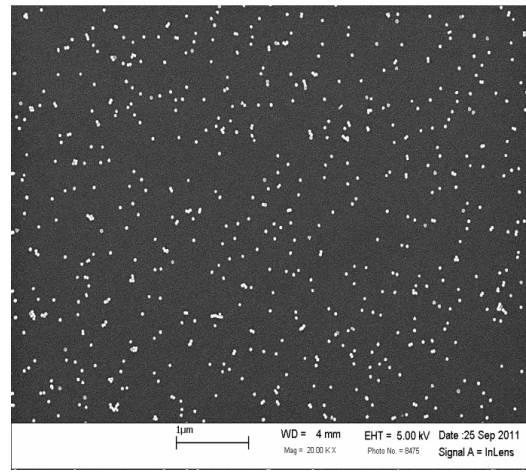
(a)



(b)



(c)



(d)

Fig. (5.2) SEM images for different deposition times of Au NPs on flat surface using 30% diluted solution: (a) 5 min. , (b) 20 min., (c)80 min. , and (d) 120 min.

$\tau = 1$ corresponds to the time when the particle diffusion length \sqrt{Dt} equals a . Therefore, for $\tau \ll 1$, the surface appears flat over the scale of the diffusion length, and consequently all the surfaces (flat and spherical) behave as the planar case, where a gradual depletion of the particles closest to the surface reduces the deposition rate over time, so that $\langle v(\tau) \sim \sqrt{\tau}$. When $\tau \gg 1$, the spherical surface is too small to appreciably deplete the particles from the suspension, and the deposition rate is therefore constant, and hence $\langle v_{sph}(\tau) \sim \tau$.

The relation between normalized density of Au NPs and the normalized time is shown in Fig. (5.3) for both a flat surface and a microsphere surface. We can conclude that, the results of a flat surface are fitted with the theory very well. For the microsphere, however, the density of particles is higher than what expected from theory at long time. One reason may be that, on this theory we did not take into consideration the liquid flow around the microsphere, which is likely not strictly true. For a flat surface, this is not that important, since at low Reynolds numbers, the flow across the surface is laminar with no component perpendicular to the surface, and will not therefore lead to mixing between layers with different NPs concentrations. For a microsphere, we are not so lucky, and even slow flow around the microsphere will lead to a higher deposition rate than the theory predicts, as the flow brings liquid with higher concentrations of particles closer to the microsphere. This is possibly the origin of the seemingly random fluctuations in deposition rates over time.

The slope of the fitted data should be the power of the time, t in the theoretical equations. For a microsphere, at short time, the slope is ~ 0.57 which is close to 0.5 (flat surface approximation), but for long time, the slope becomes ~ 0.84 which means that the relation is approximately linear. The slope of flat surface data is 0.504 (typical value is 0.5).

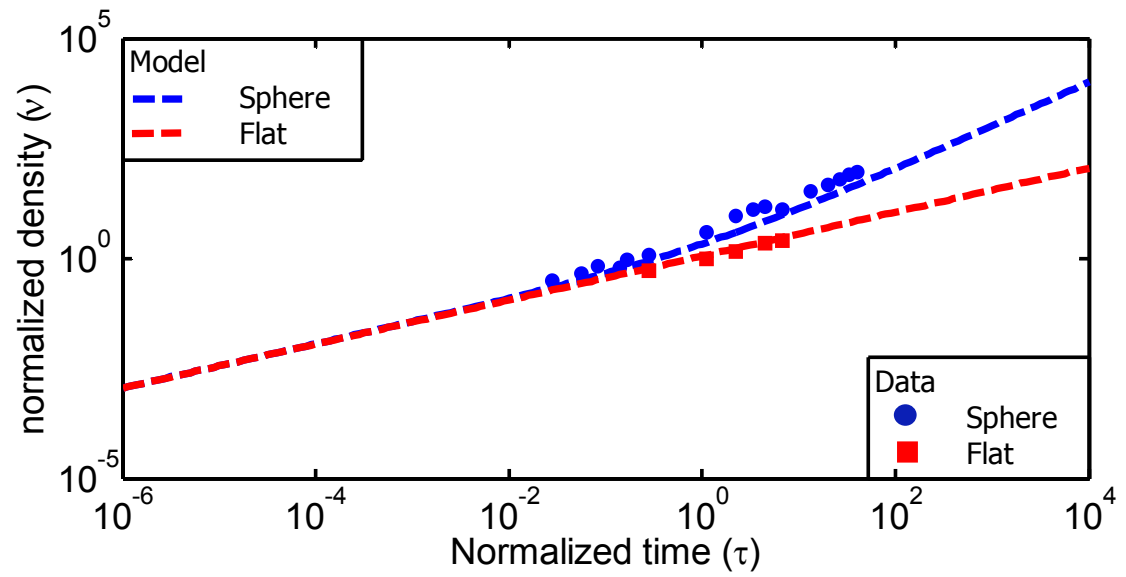


Fig. (5.3) Normalized density of Au NPs for microsphere surface and flat surface.

References

- [1] T. Sannomiya and J. Voros, Single plasmonic nanoparticles for biosensing, *Trends Biotechnol.* **29**, 343-351 (2011)
- [2] S.W. Zeng, K.T. Yong, I. Roy, X.Q. Dinh, X. Yu, and F. Luan, A Review on Functionalized Gold Nanoparticles for Biosensing Applications *Plasmonics* **6**, 491-506 (2011).
- [3] B. Sepulveda, P.C. Angelome, L.M. Lechuga, and L.M. Liz-Marzan, LSPR-based nanobiosensors, *Nano Today* **4**, 244-251 (2009).
- [4] K. Mitsui, Y. Handa, and K. Kajikawa, Optical fiber affinity biosensor based on localized surface plasmon resonance, *Appl. Phys. Lett.* **85**, 4231-4233 (2004).
- [5] N. Nath and A. Chilkoti, A Colorimetric Gold Nanoparticle Sensor To Interrogate Biomolecular Interactions in Real Time on a Surface *Anal. Chem.* **74**, 504-509 (2002).
- [6] S.F. Cheng and L.K. Chau, Colloidal Gold-Modified Optical Fiber for Chemical and Biochemical Sensing, *Anal. Chem.* **75**, 16-21 (2003).
- [7] J. Zhao, X. Zhang, C.R. Yonzon, A.J. Haes, and R.P. Van Duyne, Localized surface plasmon resonance biosensors *Nanomed.* **1**, 219-228 (2006).
- [8] G.J. Nusz, A.C. Curry, S.M. Marinakos, A. Wax, and A. Chilkoti, Rational Selection of Gold Nanorod Geometry for Label-Free Plasmonic Biosensors, *ACS Nano* **3**, 795-806 (2009).
- [9] Jihaeng Yi, Chih-Yu Jao, Ishac L.N. Kandas, Bo Liu, Yong Xu, *et al.*, Irreversible adsorption of gold nanospheres on fiber optical tapers and microspheres, *Appl. Phys. Appl. Lett.* **100**, 153107:1-4 (2012).

- [10] J.K. Wagner, S. Setayeshgar, L.A. Sharon, J.P. Reilly, and Y.V. Brun, A nutrient uptake role for bacterial cell envelope extensions, *Proc. Nat. Acad. Sci. USA* **103**, 11772 (2006).
- [11] D. Shoup and A. Szabo, Role of diffusion in ligand binding to macromolecules and cell-bound receptors, *Biophys. J.* **40**, 33-39(1982).
- [12] J.W. Evans, Random and cooperative sequential adsorption, *Rev. Mod. Phys.* **65**, 1281-1329 (1993).
- [13] J. Talbot, G. Tarjus, P.R. Van Tassel, and P. Viot, From car parking to protein adsorption: an overview of sequential adsorption processes, *Colloids Surf., A* **165**, 287-324 (2000).
- [14] Z. Adamczyk, *Particles at Interfaces: Interactions, Deposition, Structure*. (Academic Press, London, 2006).
- [15] S.E. Harding, On the hydrodynamic analysis of macromolecular conformation, *Biophys. Chem.* **55**, 69-93 (1995).
- [16] Y.G. Gu and D.Q. Li, Deposition of Spherical Particles onto Cylindrical Solid Surfaces: II. Experimental Studies *J. Colloid Interface Sci.* **248**, 329-339 (2002).
- [17] Z. Adamczyk and L. Szyk, Kinetics of Irreversible Adsorption of Latex Particles under Diffusion-Controlled Transport, *Langmuir* **16**, 5730- 5737 (2000).
- [18] Z. Adamczyk, Kinetics of Diffusion-Controlled Adsorption of Colloid Particles and Proteins, *J. Colloid Interface Sci.* **229**, 477-489 (2000).
- [19] K. Park, S.R. Simmons, and R.M. Albrecht, Surface characterization of biomaterials by immunogold staining-quantitative analysis, *Scanning Microsc.* **1**, 339 (1987).

[20] K.C. Grabar, *et al.* , Kinetic Control of Interparticle Spacing in Au Colloid-Based Surfaces: Rational Nanometer-Scale Architecture, *J. Am. Chem. Soc.* **118**, 1148-1153 (1996).

[21] Z. Adamczyk, K. Jaszczolt, B. Siwek, and P. Weronki, Irreversible adsorption of particles at random-site surfaces, *J. Chem. Phys.* **120**, 11155:1-8 (2004).

CHAPTER 6

Functionalization of Silica-based Microstructures

6.1 Nonlinear Fiber Tapers

Despite its prominence in optics, silica glass has some intrinsic limits. For example, silica can have third order nonlinearity but lacks second order nonlinearity [1, 2]. Consequently, it is difficult to investigate important processes such as second harmonic generation and second order parametric oscillation [3]. The key to overcome this deficiency is to develop versatile methods that can functionalize the surface of a silica fiber with various nonlinear nanomaterials. Yong Xu *et al.* have theoretically proposed a general approach that can produce thermally stable second order nonlinearity on the silica fiber surface [1]. However, to achieve high conversion efficiency, we must satisfy the phase matching condition between the pump beam and the nonlinear signals. For typical nonlinear crystals such as LiNbO₃, a common approach is to utilize crystal birefringence to achieve phase matching or quasi-phase-matching [4]. Unfortunately, this approach is not suitable for silica glass, since its refractive index is uniform and isotropic. For a uniform fiber taper (i.e., with constant taper radius) coated with a nonlinear film, the power of generated second harmonic signal can be expressed as, [5]

$$P_{2\omega} = 2\omega^2 \left(\frac{\mu_0}{\varepsilon_0 \varepsilon_r} \right)^2 \frac{P_\omega^2}{\pi a^2} \left| \frac{\delta}{a} \chi_{rrr}^{(2)} \right|^2 L^2 \times \frac{\sin^2(\Delta\beta L/2)}{(\Delta\beta L/2)^2}, \quad (6.1)$$

where P_ω is the power of fundamental beam, $P_{2\omega}$ is the power of generated SHS, ω is the angular frequency of pump beam, δ is the film thickness, a is the fiber radius, $\chi_{rrr}^{(2)}$ is the radial component of second order susceptibility, L is the taper length, and $\Delta\beta = 2\beta_\omega -$

$\beta_{2\omega}$, β_{ω} , $\beta_{2\omega}$ are the propagation constants of fundamental and second harmonic signals respectively. The mismatch in the propagation constant of the fundamental and the second harmonic light can be expressed by

$$\Delta\beta = \frac{4\pi}{\lambda} [n_{eff}(\omega) - n_{eff}(2\omega)] \quad (6.2)$$

where λ is the fundamental wavelength in vacuum, $n_{eff}(\omega)$ and $n_{eff}(2\omega)$ are the effective refractive index of silica at pump and SHS wavelengths, respectively. Due to material dispersion of silica, the phase matching condition ($\Delta\beta = 0$) is normally unsatisfied. Based on the selective rule [1], the angular mode number of SHS, $l_{2\omega}$ should equal to $l_{\omega} + l_{\omega}$, where l_{ω} is the angular mode number of the fundamental beam. In case that the fundamental beam propagate in the fundamental mode (HE_{11}), l_{ω} would be ± 1 . So, the possible SHS modes are TE01, TM01, or HE21 modes, which have $l_{2\omega} = 0$ or $l_{2\omega} = 2$ [8]. Propagation in different modes means facing different refractive indices, which can allow phase matching. Controlling the fiber diameter can achieve the proper condition for phase matching ($\Delta\beta = 0$). For example, at the taper diameter of $2a = 0.5320$, intermodal phase matching can be verified between $HE_{11}(\omega)$ and TE01 (2ω). At diameter of $2a = 0.5960$, phase matching can be verified between $HE_{11}(\omega)$ and HE21 (2ω) [8]. The conversion efficiency is around 4.3×10^{-5} at pump peak power $P_{\omega} = 5W$ (from Optical Parametric Oscillation (OPO) model OPOlette 355II from OPOtek Inc).

Unfortunately, fabricating a nonlinear fiber with submicron diameter is difficult. First, after coating the submicron fiber taper with nonlinear polymer, the taper transmission loss tends to be very high, , which is mainly due to the absorption from nonlinear film

and particles adsorbed to the fiber taper during the deposition process. Furthermore, submicron tapers are very fragile and can be easily broken.

Another technique that can produce strong SHG is quasi-phase-matching (QPM), which requires a spatially periodic modulation of the nonlinear coefficient [6]. QPM was first demonstrated in 1962 [7] and 1963 [8]. Since then, QPM has been demonstrated in a large number of different material systems, including cadmium telluride (CdTe) [9], GaAs [10, 11], quartz, LiNbO₃ [12], LiTaO₃ [13], and KTP [14]. Alternative to the crystal based second order nonlinearity, several research groups have attempted to implement QPM using fiber devices such as poled fibers. First, internal field was applied to produce periodic $\chi^{(2)}$ grating [15, 16]. D-shape fiber was used to enhance the SHG by applying external poling electric field at room temperature [17, 18]. Twin-hole fiber was poled via inserting the electrode wires into the side holes while the voltage was 2.5kV at 300°C for 40 minutes [19]. However, changing the shape of the fiber can induce excess power loss, in addition to the instability of the periodic structure of generated $\chi^{(2)}$ [20].

We have applied a new approach for implementing QPM in nonlinear fiber tapers. In this chapter, we discuss the theory and preliminary experiments on SHG in a nonlinear fiber taper with spatially periodic nonlinearity.

6.1.1 Theory for QPM in a Nonlinear Fiber Taper

Equation (6.2) describes the power of second harmonic signals generated by the nonlinear fiber taper. Without phase matching, power of SHS should oscillate with distance. The distance at which the power goes to its maximum before decreasing is defined as the coherence length (L_{coh}). From Eq. (6.1), it can be written as

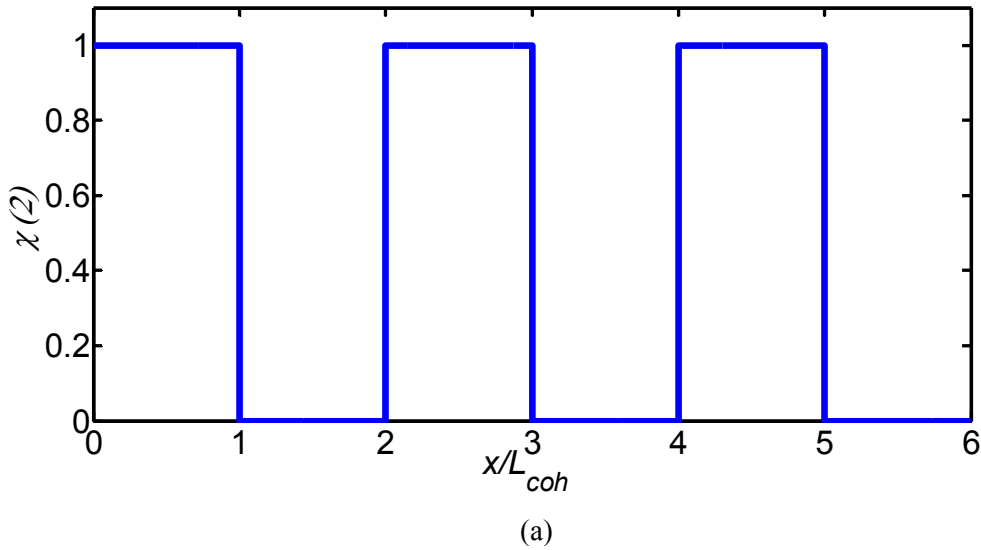
$$L_{coh} = \frac{L}{\Delta\beta} \quad (6.3)$$

Periodic structure of $\chi^{(2)}$ can be written to have a monotonic build-up of power which shown in Fig. (6.1-a) and power of SHS is shown in Fig. (6.1-b). Both units in the two figures are normalized.

In order to satisfy the quasi-phase-matching condition, the grating period Λ of $\chi^{(2)}$ variation should satisfy the condition:

$$\Lambda = 2L_{coh} = \frac{2\pi}{\Delta\beta} \quad (6.4)$$

Based on Eq. (4), the grating period Λ depends on the pump wavelength and the taper radius. In the range of wavelength of 1100-1300 nm, the grating period is 45-55 μm [21]. Starting from the coupled mode equations and taking in consideration the periodic change of $\chi_{eff}^{(2)}$, equation for the power of SHS with QPM on fiber taper can be derived.



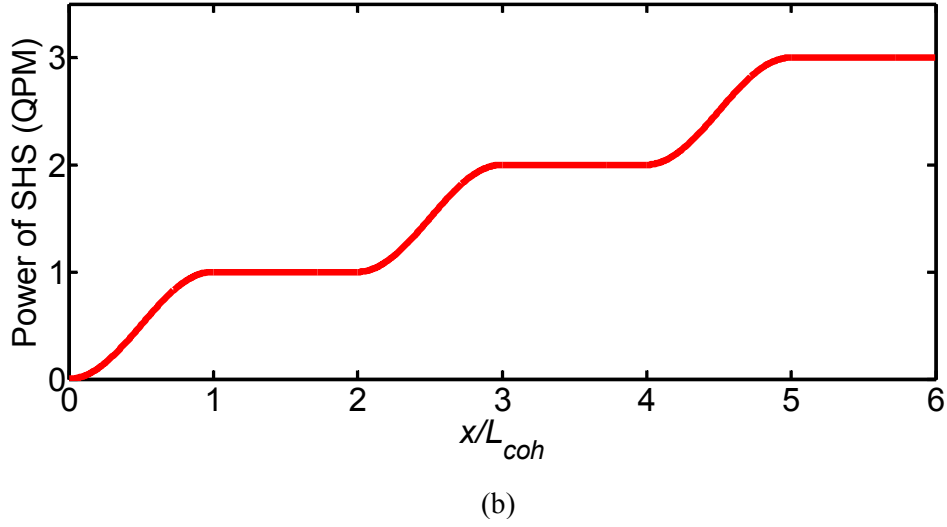


Fig. (6.1): (a) periodic structure of $\chi^{(2)}$, and (b) corresponding power of SHS.

By assuming uniform taper waist with length L , the SHS power was derived [8] to be

$$P_{2\omega} = \frac{1}{2} \varepsilon v_g(2\omega) |A_{2\omega}|^2 \quad (6.5)$$

where ε is the permittivity, $v_g(2\omega)$ is the group velocity, and $A_{2\omega}$ is the SHS field amplitude and is given by

$$A_{2\omega} = \frac{-\omega}{2v_g(2\omega)} A_\omega^2 L \chi_{eff}^{(2)} \left[\sum_m G_m e^{-\Delta\beta_m L/2} \frac{\sin^2(\Delta\beta_m L/2)}{(\Delta\beta_m L/2)^2} \right] \quad (6.6)$$

where A_ω is the pump field amplitude, G_m is the Fourier coefficient of $\chi_{eff}^{(2)}(z)$, and $\beta_m = \Delta\beta - k_m = \Delta\beta - 2\pi m/\Lambda$. The result is shown in Fig. (6.2). Simulation was done by Chalongrat Daengngam [21], using grating period $\Lambda = 50 \mu\text{m}$, and interaction length $L = 100 \times \Lambda = 5 \text{ mm}$. It is clear that, optimum conversion efficiency can be obtained by tuning the pump wavelength.

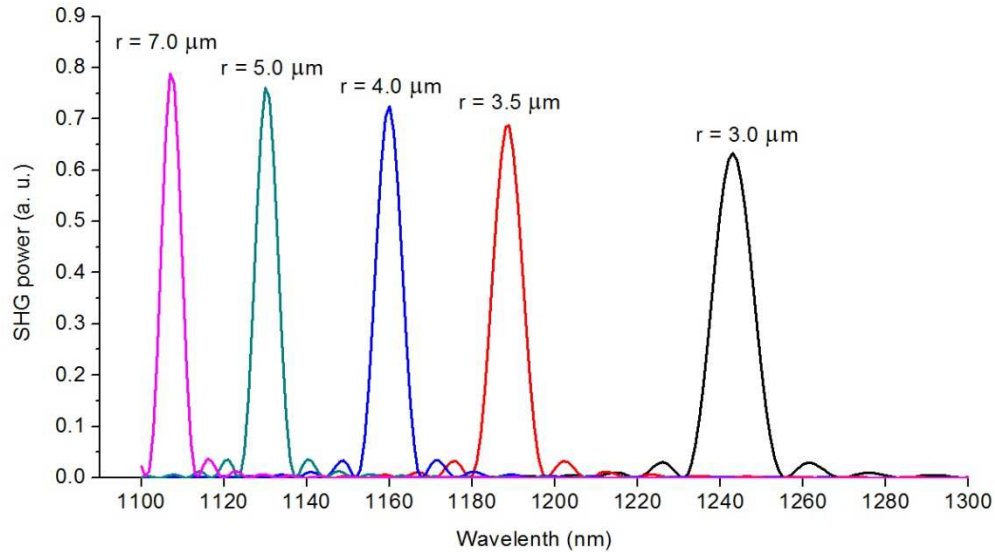


Fig. (6.2) Theoretical calculation for QPM SHS in fiber taper [21]. Used with permission of Chalongrat Daengngam, 2013.

6.1.2 Fabrication and Experimental Setup for QPM Measurement

The fiber taper is fabricated in the same way discussed in chapter 3. In addition, the loss before and after tapering is measured using optical power meter. Then, the fiber taper is glued on a glass slide. Deposition of nonlinear film of PAH/PB (10 bilayers) is carried out as explained before in Chapter 4. The only difference is the dipping machine used in film deposition. Here we use a dipping machine where the rinsing of the sample is done without the sample rotation. Taper fabrication and nonlinear film deposition should be carried out in the same day to make sure that the sample remains clean and dust free.

The SHG measurement system is shown on Fig. (6.3). OPO is used to generate linearly polarized pulsed wave light with wavelength between 1100-1300 nm. The generated pulse has a width of 10 ns and pulse repetition rate of 20Hz. Two long pass filters (F1 and F2) are used to block the visible light comes with the infrared light. The

polarizer (P) controls the amount of power passed through it. Light can be coupled to and from the fiber (50 μm core, 125 μm cladding, NA = 0.22) through 40 \times objective lens (OL2 and OL3). The two lenses (L1 and L4) are responsible for focusing light in small spots. The coupling efficiency can be optimized using 3D manual stage. Due to the relatively the spatial profile of the OPO pump, the coupling efficiency is typically between 3% -5%. Glass substrate (G) can reflect a small amount of light which goes to a photodetector (PD) sensitive to the long wavelength range. Short pass filter (F3) rejects the pump signal and pass the generated the SHS. A monochromator is synchronized with the OPO during the scanning process to detect the generated wavelength of SHS. The output power from the monochromator is collected by photomultiplier tube (PMT) (model 9130B from ET Enterprises Limited). PMT and PD outputs can be monitored using the oscilloscope, which is connected to computer (PC). PMT requires a high voltage for proper operation (about 1.8 KV).

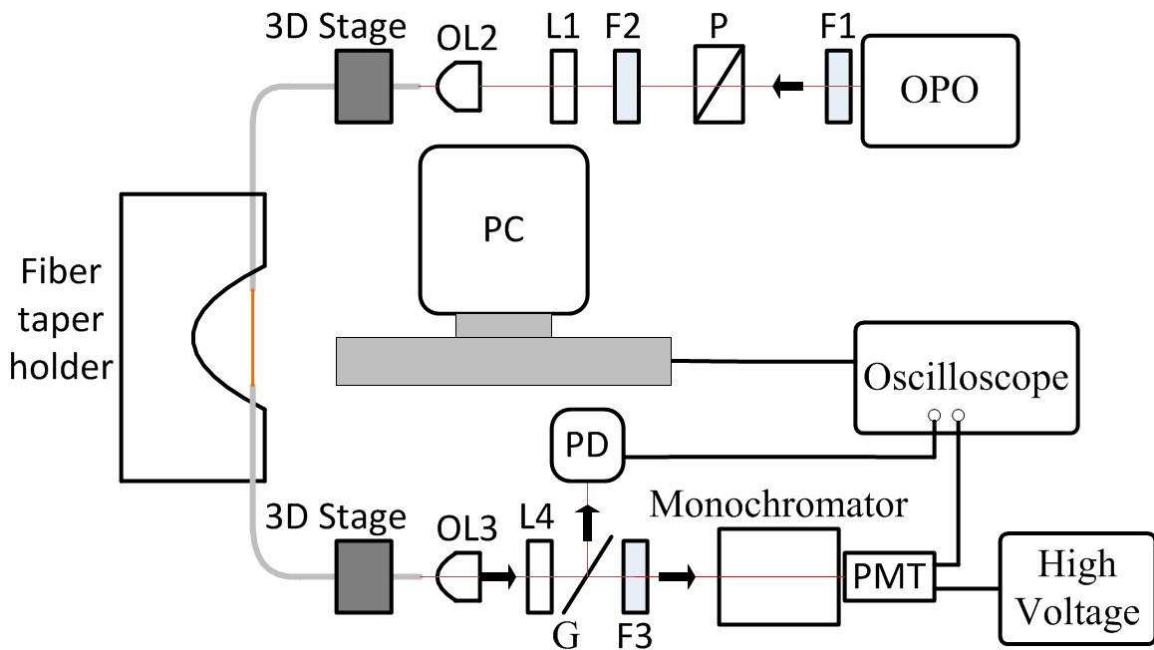


Fig. (6.3) Schematic of SHG measuring system.

To create spatially periodic nonlinear coefficient, we used the method of UV ablation. Specifically, the sample, which is uniformly coated with the nonlinear film, is exposed to the strong UV light generated by an excimer laser from MPB technology Inc. the UV wavelength from the laser is 248 nm, pulse width is 10 ns, beam size is $\sim 1\text{cm}^2$, and repetition rate of 5 Hz. A photomask with grating of period $\Lambda = 50\mu\text{m}$ made up of an 800-nm-thick Al layer deposited on a UV-grade fused silica substrate was purchased from Creative MicroSystems Corporation to write the gratings. The fiber taper is placed under the photomask. Photomask with fiber taper sample is subjected to the laser for about 5 minutes to ensure the removal of the film segments and remove all possible residual masses [21]. SHG measurements are performed after patterning using UV laser ablation.

6.1.3 SHG in a Periodically Patterned Fiber Taper

To ensure that the polymers assembled over the fiber taper can be removed through UV ablation, we first used a fiber taper covered with fluorescent dyes instead of nonlinear polymers. In particular, we first deposited 20 bilayers of PAH/ polystyrene sulfonate (PSS) on the fiber taper. Then we apply the same ablation technique to create spatially periodic patterns. Afterwards, a confocal microscope was used to get image of the fiber taper coated with 20 bilayer of PAH/PSS with pattern as shown in Fig. (6.4) **(Image was taken by Islam Ashry, Dr.Yong Xu's group, Department of Electrical and Computer Engineering, Virginia Tech.)**

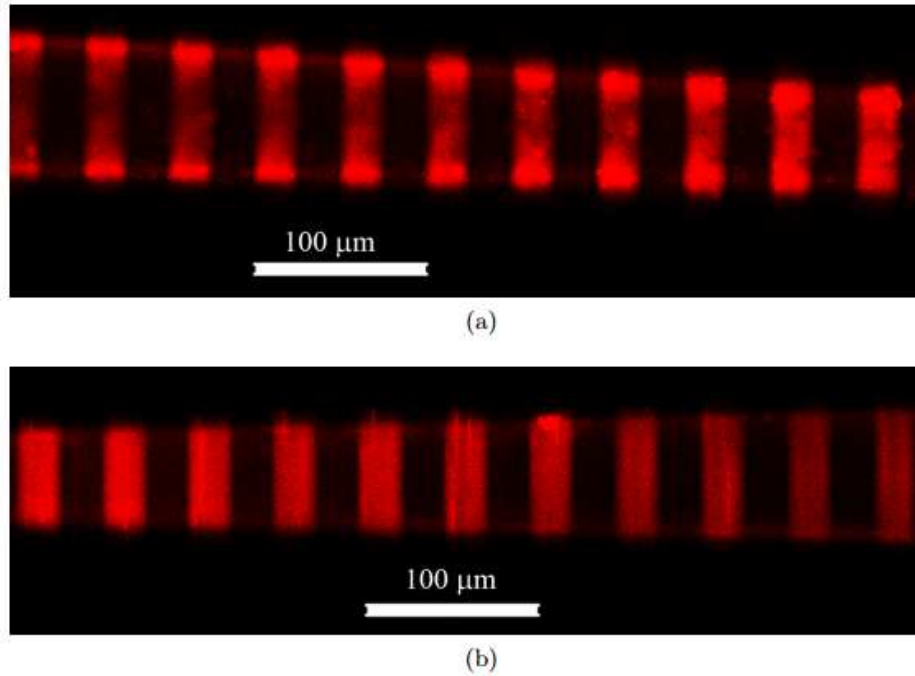


Fig. (6.4) Confocal fluorescence microscope images of a periodic pattern of 20-bilayer PAH/PSS-Dye film coated on a fiber taper: (a) near side and (b) far side.

Second harmonic signals were measured before and after patterning. (10 bilayers of PAH/PB were deposited on the fiber taper. The results are shown in Fig. (6.5-a). The taper waist radius is $\sim 3.75 \mu\text{m}$ (Fig. (6.5-b), which is determined by LEICA optical microscope (DMI300B). The fiber tapered length is $\sim 4.7 \text{ mm}$, which is determined by the distance at which the radius of fiber tapered is twice the waist radius. The output pump pulse energy from the taper is $4 \mu\text{J}$ (corresponding to peak power of 400 W). An enhancement is observable in the QPM case compared with the phase-mismatching case.

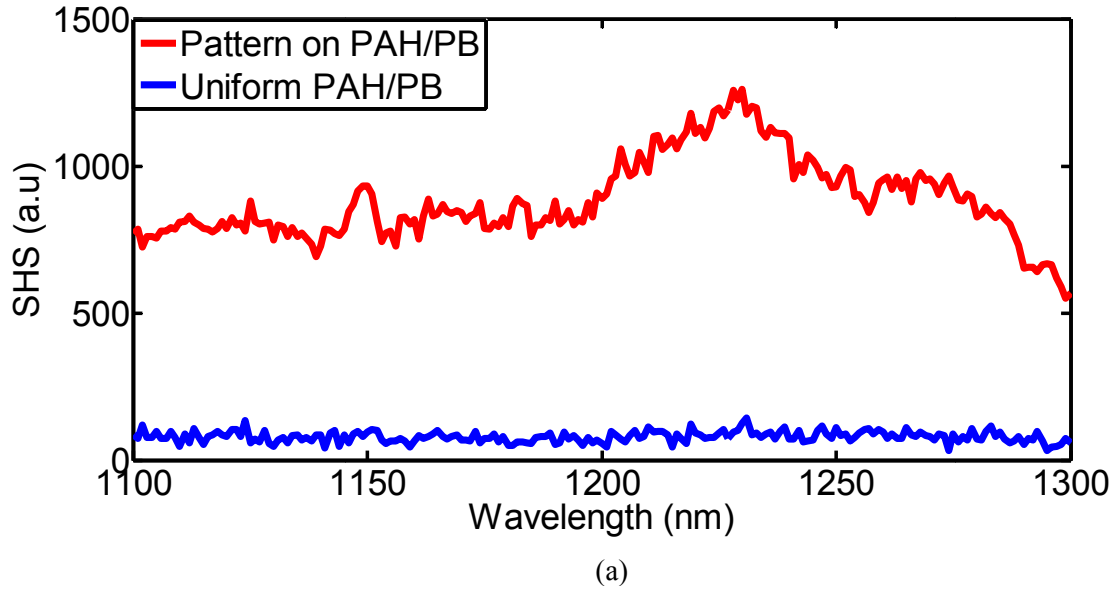
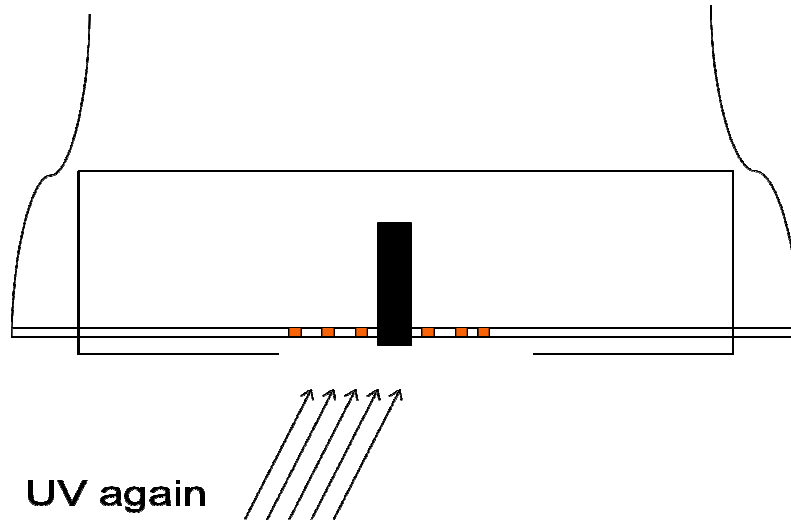


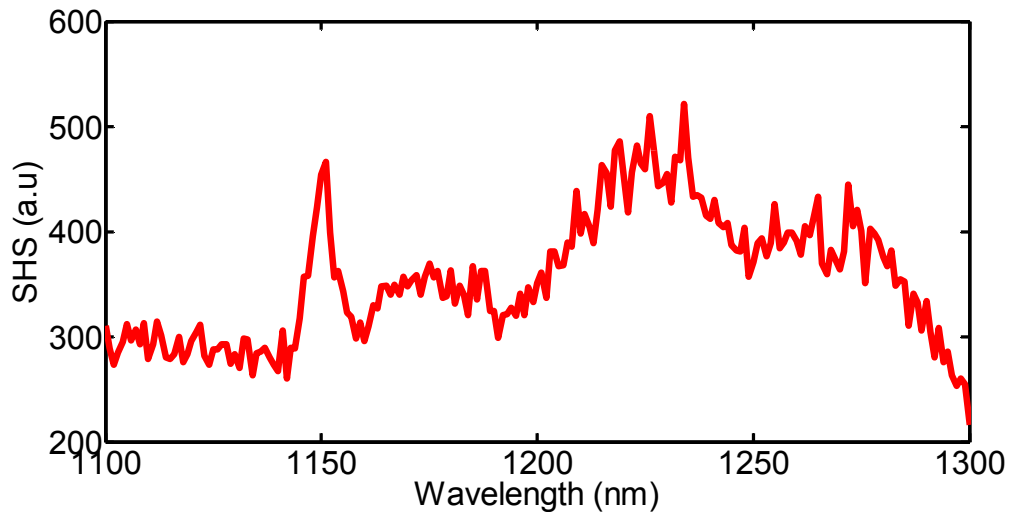
Fig. (6.5): (a) SHS measured for 10PAH/PB with phase-mismatching (blue line) and with QPM (red line), and (b) measured fiber taper diameter using optical microscope.

This result is consistent with the results done before [21]. The spectrum broadening can potentially be attributed to the non-uniformity of the fiber taper size. So, we used the UV laser ablation again to remove the coating (without using of phasemask) and length about 1mm at the center was left (by blocking) as shown in Fig. (6.6-a). First of all, the reduction of SHS is expected as we removed many of the coating stripes. Although the broadened spectrum did not change much, we have noticed an increase in the peak

around 1150 nm (Fig. (6.6-b)). This peak is around the predicted one for fiber tapered of radius 3.75 μm (see Fig. (6.2)).



(a)



(b)

Fig. (6.6): (a) removing the coating and maintaining a length about 1 mm at the center, and (b) SHS measured for 10PAH/PB after removing the coating and maintaining a length about 1 mm at the center.

6.2 Quantum Dots (QDs)

6.2.1 Introduction

QDs are semiconductor nanocrystals and their electronic properties are related to the size and the shape of individual crystal. As the size is reduced, the band gap energy is increased which means larger difference between valence band and conduction band. In this case, more energy (higher frequency) is needed to excite the dot. Colloidal nanocrystals of II-VI semiconductors (CdS, CdSe, CdTe) in the 1-10 nm size have attracted a great attention in the physics, chemistry, and engineering fields [22].

By combining the features of WGMs (High Q factor, large FSR) and QDs, microlasers with high efficiency and ultralow threshold can be achieved [23, 24]. In small size QDs (compared to electron-hole exciton Bohr radius), the electronic transitions are discrete. S. I. Shopova *et al.* demonstrated an ultralow-threshold continuous-wave lasing. The gain medium was HgTe QDs (colloidal NPs) coating fused-silica microsphere. Coupling into and out of microsphere was achieved with high efficiency using coupling system between microsphere and tapered fiber. Both the size and the composition of the QDs can impact the lasing wavelength. QDs of the form $\text{Hg}_{1-x}\text{Cd}_x$, can extend the lasing wavelength to the infrared region (1240 to 1780 nm depending on the size of the QDs). Ultralow-threshold laser (200 nW) was achieved. J. Schäfer *et al.* reported single mode and multimode laser using microdrop containing CdSe/ZnS QDs [25]. Single mode laser was achieved when the liquid microsphere diameter is less than 10 μm , and multimode laser was observed for bigger microdroplets (up to 41 μm).

Doped microsphere resonator with rare-earth-ions (such as neodymium-doped silica microspheres) can be used to have ultra-threshold microlaser [26]. Fluoride and

phosphate glass microspheres can absorb rare-earth ions with high concentration, so they are widely used. In particular, in Ref [27], a base microsphere of undoped silica was coated with an erbium-doped solgel film.

6.2.2 CdSe/ZnS core/shell QDs based Laser

A silica multimode fiber (50 μm core and 125 μm cladding, purchased from Corning Inc.) or microsphere made from the same fiber are coated with 5-nm CdSe/ZnS core/shell Quantum dots (QDs) (purchased from NN-LABS). Deposition of QDs on the fiber or microsphere surface is performed using the same layer-by-layer technique previously used for Au NPs. First, the fiber (microsphere) is dipped in an aqueous solution of PAH as before for 3 minutes to obtain positively charged layer on the surface. Then, rinsing with DI water was done for 2 minutes. Afterwards, the sample was dipped in a solution of negatively charged CdSe/ZnS QDs for time between 35-40 seconds to prevent aggregation of QDs. Finally, we rinsed the sample again. We repeated the procedure to have another layer which could give us a stronger emission than one layer.

Optical pumping was carried out using the system illustrated in Fig. (6.7). We used OPO (OPOlette 355II from OPOtek Inc) to generate linearly polarized pulsed pump light with wavelength between 435-500 nm. The generated pulse has a width of 10 ns and pulse repetition rate of 20Hz. Two band pass filters (F1 and F2) are used to remove any residual infrared light. The polarizer (P) controls the amount of power passed through it. Light can be coupled to and from the fiber (50 μm core, 125 μm cladding, NA = 0.22) through 40 \times objective lens (OL2 and OL3). The two lenses (L1 and L4) are responsible for focusing light in small spots. The coupling efficiency can be optimized using 3D manual stage. Long pass filter (F3) rejects the pump signal and pass the generated signal.

A monochromator (Cornerstone 74125) is used to filter out the fluorescent signal produced by the fiber or microsphere. The output power from the monochromator is collected by photomultiplier tube (PMT) (PMT R2228, by Hamamatsu). PMT and PD outputs can be monitored using the oscilloscope, which is connected to computer (PC). PMT requires a high voltage to work well (about 0.6 KV).

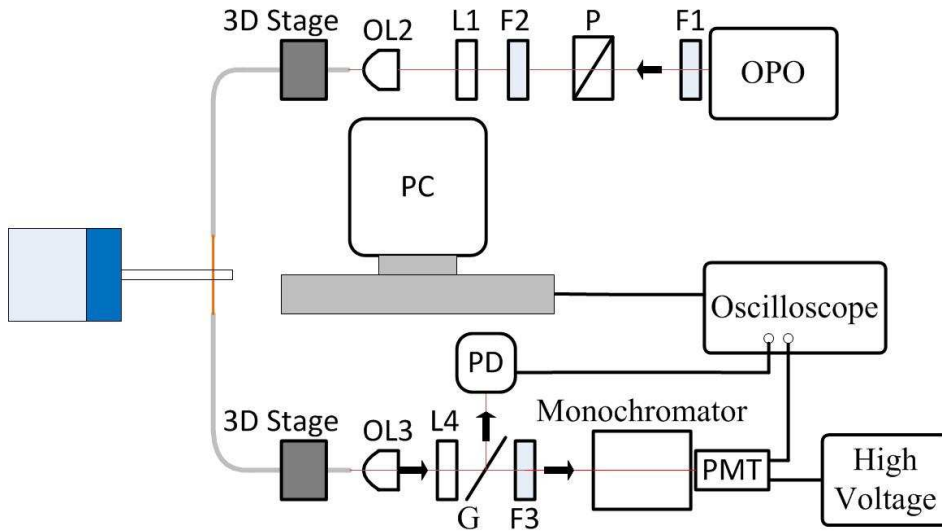


Fig. (6.7) Schematic of coupling system between fiber (microsphere) and fiber taper to study lasing effect.

Pump light is coupled into the fiber (microsphere) using a fiber taper with diameter in the range of 1-2 μm . the emission from the fiber (microsphere) is collected through the same fiber taper. The emission spectral from the multimode fiber was shown in Fig. (6.8) and results are obtained for pump wavelength of 496 nm. The measurements were done at input pulse energy, E of 20, 60, 100, 200, and 300 μJ , respectively. The peak power, P_{peak} can be calculated from

$$P_{peak} = \frac{E}{\tau} \quad (6.7)$$

where τ is the pulse width (10 ns in our case). Considering the coupling efficiency ($\sim 5\%$), the peak powers of the pump would be 100, 300, 500, 1000, 1500 W, respectively.

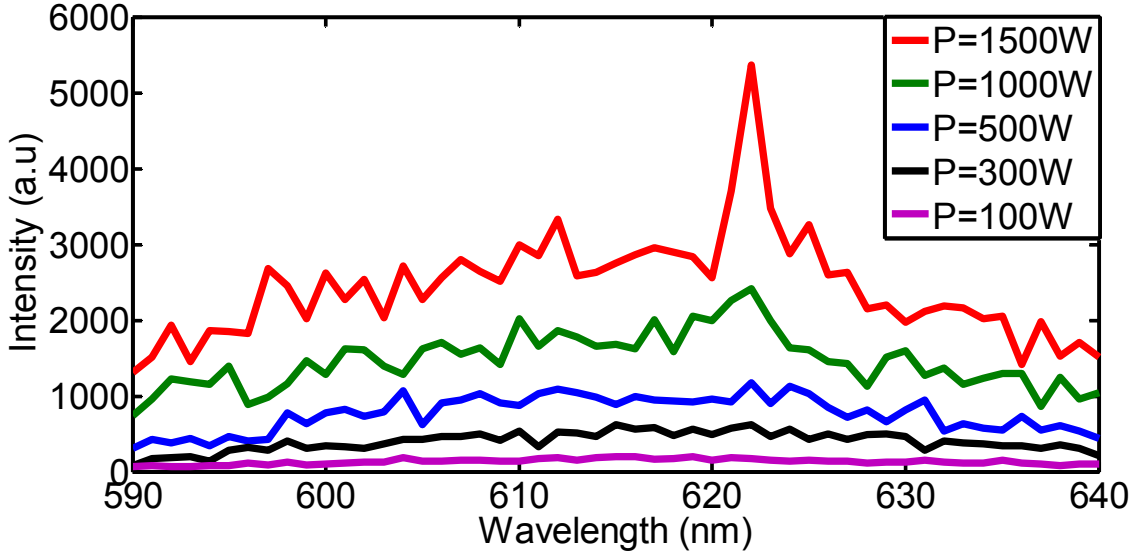


Fig. (6.8) Spectral emissions from cylindrical resonator at different pump power.

A comparison between the cylindrical and spherical resonators is displayed in Fig. (6.9). The input peak power is 1500 W and the resolution of monochromator is reduced to 0.1 nm instead of 1 nm. The microsphere radius is $\sim 125 \mu\text{m}$.

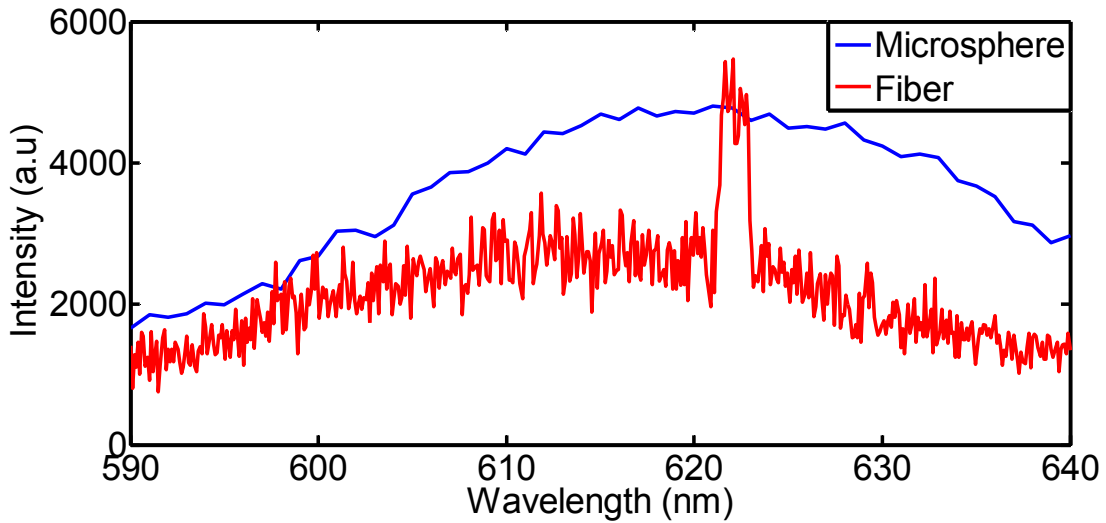


Fig. (6.9) Comparison between emission of fiber and microsphere coated with 2 bilayers of PAH/(CdSe/ZnS).

The result in Fig. (6.9) suggest that we can achieve lasing in cylindrical resonator but not the spherical resonator. One possible explanation is that the spherical resonator has a much higher Q factor. We measured the Q factor of cylindrical resonator using NEW FOCUS 6300 tunable laser diode. Q factor of bare cylindrical resonator was $\sim 4 \times 10^4$ and Q factor of coated cylindrical resonator with QDs was $\sim 3 \times 10^4$. Yet the OPO cannot be accurately tuned with <1 nm accuracy. Consequently, due to the frequency mismatch between the OPO pump and the WGM resonance, we cannot couple a significant portion of the OPO pump into the WGM circulating within the resonator. This frequency mismatch problem is potentially less severe with the silica cylinder, which tends to exhibit lower Q factors.

The maximum Q factor, Q_{max} . can be estimated from

$$Q_{max.} = \frac{\lambda_p}{OPO_{acc.}} \quad (6.8)$$

where λ_p is the pump wavelength, and $OPO_{acc.}$ is the OPO minimum tuning accuracy (which is 1 nm for our model). As, the pump wavelength is in the range 450-500 nm, the $Q_{max.}$ would be around 500 which is very low. So, the microsphere could not support a lasing action and the normal emission spectrum was obtained. In the fiber case, we could have a lasing action but unfortunately it was not repeatable and hard to achieve.

References

- [1] Yong Xu, Anbo Wang, James R. Heflin, and Zhiwen Liu, Proposal and analysis of a silica fiber with large and thermodynamically stable second order nonlinearity, *Appl. Phys. Lett.* **90**, 211110:1-3 (2007).
- [2] G. P. Agrawal, *Nonlinear fiber optics*, 4th edition. (Elsevier, Singapore, 2007).
- [3] Yong Xu, Ming Han, and Anbo Wang, Second Order Parametric Processes in Nonlinear Silica Microspheres, *Phys. Rev. Lett.* **100**, 163905:1-4 (2008).
- [4] D. Dimitropoulos, V. Raghunathan, R. Claps, and B. Jalali, Phase-matching and nonlinear optical processes in silicon waveguides, *Opt. Express* **12**, 149-160 (2003).
- [5] Chalongrat Daengngam, *et al.*, Demonstration of a cylindrically symmetric second-order nonlinear fiber with self-assembled organic surface layers, *Opt. Express* **19**, 10326-10335 (2011).
- [6] Martin M. Fejer, G. A. Magel, Dieter H. Jundt, and Robert L. Byer, Quasi-Phase-Matched Second Harmonic Generation: Tuning and Tolerances, *IEEE Quantum Electron.* **28**, 2631 - 2654 (1992).
- [7] J. A. Armstrong, N. Bloembergen, J. Ducuing, and P. S. Pershan, Interactions between Light Waves in a Nonlinear Dielectric, *Phys. Rev.* **127**, 1918-1939 (1962).
- [8] P. A. Franken, and J. F. Ward, Optical harmonics and nonlinear phenomena, *Rev. Mod. Phys.* **35**, 23-39 (1963).
- [9] M. S. Piltch, C. D. Cantrell, and R. C. Sze, Infrared second-harmonic generation in nonbirefringent cadmium telluride, *J. Appl. Phys.* **47**, 3514-3517 (1976).
- [10] A. Szilagy, A. Hordvik, and H. Schlossberg, A quasi-phase-matching technique for efficient optical mixing and frequency doubling, *J. Appl. Phys.*, **47**, 2025-2032 (1976).

- [11] D.E. Thompson, J. D. McMullen, and D. B. Anderson, Second-harmonic generation in GaAs 'stack of plates' using high-power CO₂ laser radiation, *Appl. Phys. Lett.* **29**, 113-115(1976).
- [12] M. Okada, K. Takizawa, and S. Ieiri, Second harmonic generation by periodic laminar structure of nonlinear optical crystal, *Opt. Commun.* **18**, 331-334 (1976).
- [13] W. S. Wang, Q. Zhou, Z. H. Geng, and D. Feng, Study of LiTaO₃ crystals grown with a modulated structure: I. Second harmonic generation in LiTaO₃ crystals with periodic laminar ferroelectric domains, *J. Cryst. Growth* **79**, 706-709 (1986).
- [14] C. J. van der Poel, J. D. Bierlein, J. B. Brown, and S. Colak, Efficient type I blue second-harmonic generation in periodically segmented KTiOPO₄ waveguides, *Appl. Phys. Lett.* **57**, 2074-2076(1990).
- [15] M.C Farries, P. St. J. Russell, M.E. Fermann, and D.N. Payne, Second-harmonic generation in an optical fibre by self-written $\chi(2)$ grating, *Electron. Lett.* **23**, 322-324 (1987).
- [16] D.Z. Anderson, V. Mizrahi, and J.E. Sipe, Model of second-harmonic generation in glass optical fibers based on asymmetric photoelectron emission from defect centers, *Opt. Lett.* **16**, 796-798 (1991).
- [17] M.-V. Bergot, *et al.*, Generation of permanent optically induced second-order nonlinearities in optical fiber by poling, *Opt. Lett.* **13**, 592-594 (1988).
- [18] M.E. Fermann, *et al.*, Second-harmonic generation using gratings optically written by mode interference in poled optical fibers, *Opt. Lett.* **14**, 748-750 (1989).

- [19] Toru Mizunami, Takahiro Tsukada, Yasuhiro Noi and Keiichi Horimoto, Second-order nonlinearity and phase matching in thermally poled twin-hole fiber, Proc. of SPIE **5350**, 115-122 (2004).
- [20] A. L. Moura, M. T. de Araujo, M. V. D. Vermelho, and J. S. Aitchison, Improved stability of the induced second-order nonlinearity in soft glass by thermal poling, J. Appl. Phys. **100**, 033509:1-5 (2006).
- [21] Chalongrat Daengngam, Second-Order Nonlinear Optical Responses in Tapered Optical Fibers with Self-Assembled Organic Multilayers, Virginia Polytechnic Institute and State University, 2012.
- [22] S. R. Cordero, Photo-Activated Luminescence of CdSe Quantum Dot Monolayers, J. Phys. Chem. B **104**, 12137-12142 (2000).
- [23] S. I. Shopova, G. Farca, and A. T. Rosenberger, Microsphere whispering-gallery-mode laser using HgTe quantum dots, Appl. Phys. Lett. **85**, 6101-6103 (2004).
- [24] Jonathan Ward and Oliver Benson, WGM microresonators: sensing, lasing and fundamental optics with microspheres, Laser Photonics Rev. **5**, 553–570 (2011).
- [25] J. Schäfer, *et al.*, Quantum Dot Microdrop Laser, Nano Lett. **8**, 1709-1712 (2008).
- [26] V. Sandoghdar, *et al.*, Very low threshold whispering-gallery-mode microsphere laser, Phys. Rev. A **54**, R1777-R1780 (1996).
- [27] Lan Yang and K. J. Vahala, Gain functionalization of silica microresonators, Opt. Lett. **28**, 592-594 (2003).

CHAPTER 7

Conclusion and Future Work

Here we summarize our results and propose some directions for future research work.

7.1 Conclusion

7.1.1 Functionalization of microsphere surface

We have investigated the Q factor of silica microsphere coated with thin film of nonlinear materials such as PB and PCBS. Nonlinear films (PAH/PB and PAH/PCBS) were fabricated using ISAM technique. The concentrations and the pH values are respectively 0.93 mg/mL and PH ~7 for PAH solution, 3.7 mg/mL and pH ~7 for PCBS solution, and 1 mg/mL and pH ~10.5 for PB solution. UV laser ablation and Dektak Profilometer were used to determine the bilayer thickness. The thickness of one bilayer was measured to be ~ 1.3 nm for PAH/PB and ~ 0.9 nm for PAH/PCBS. As a conclusion, we have investigated the Q factor of silica microspheres after coating with a thin film of nonlinear materials such as PB and PCBS. Scattering loss due to surface roughness was found to be very small compared with absorption loss of the film. The Q factor due to direct contact between the bare microsphere and fiber taper was $\sim 2 \times 10^7$. The Q factor due to absorption and scattering loss from the added film of PAH/PB and PAH/PCBS decreases nearly linearly with the film thickness in Log scale. The Q factor for PAH/PB coating is slightly larger than that of PAH/PCBS for the same film thickness. Coating a microsphere with 20 bilayers of PAH/PB or PAH/PCBS drops the Q factor to value greater than 10^6 which is still suitable for SHG. As future work, a coated microsphere with thin film of PAH/PB or PAH/PCBS will be used to generate a second harmonic signal (SHS). In

addition, adsorption of gold nanoparticles on the microsphere surface was investigated. A relation between the particle density and Q factor was derived and verified experimentally.

7.1.2 Irreversible Adsorption of Au NPs on Microspheres

We have derived simple expressions describing adsorption of spherical particles onto adhesive spherical and flat surfaces in the absence of flow, and shown that realistic deposition conditions are well described by the theory. The scaling behavior of the model is correct for all cases we examined. Our main finding is that highly curved surfaces accumulate particles significantly faster than their flat counterparts at long deposition times, even though their behavior is identical at short deposition times. For the cases we have studied here, with deposition times on the order of minutes to hours, and radii of curvatures around 125 μm .

7.1.3 Nonlinear Fiber Tapers

Quasi-phase-matching (QPM) can be used to enhance the second harmonic generation (SHG) efficiency for nonlinear fiber taper. Periodic modulation of $\chi^{(2)}$ (0 and 1) allowing the monotonic increase in the SHS power. A photomask with period 50 μm and UV laser ablation were used to write a pattern on fiber taper coated with 10PAH/PB bilayers. The pump wavelength used of range 1100-1300 nm. Writing a pattern on the film produced a QPM and improved the generated SHS by factor about 10 for fiber taper of radius ~ 3.75 μm . A big part from the transition part was removed and a noticeable peak was noticed at 1150 nm which is consistent with the theoretical prediction. The broadening of the spectrum can be explained by the non-uniformity of the fiber taper.

7.1.4 CdSe/ZnS QDs based Laser

A preliminary investigation of lasing in a silica fiber (microsphere) coated with CdSe/ZnS core/shell quantum dots (QDs) was carried. The microsphere could not support a lasing action and the normal emission spectrum was obtained. In the fiber case, we could have a lasing action but unfortunately it was not repeatable and hard to achieve.

7.2 Future Work

- Building up a suitable system to measure the SHS generated from coated microsphere with nonlinear film. Find the optimum number of bilayers for SHG as there is a tradeoff between this number and the Q factor of the spherical resonator.
- Applying QMP to the surface of coated microsphere with nonlinear film to enhance the generated SHS and comparing it with phase mismatching case.
- Improving the SHG generated from patterned fiber taper by finding a way to increase its length and make the fiber taper more uniform.
- Building up a suitable system to measure the lasing effect generated from microsphere coated with QDs.